PREPARATION OF LEAD-FREE BZT-BCT THIN FILMS BY CHEMICAL SOLUTION DEPOSITION AND THEIR CHARACTERIZATION

A THESIS SUBMITTED TO
THE GRADUATE SCHOOL OF NATURAL AND APPLIED SCIENCES
OF
MIDDLE EAST TECHNICAL UNIVERSITY

BY

BARIŞ ÇELTİKÇİ

IN PARTIAL FULFILLMENT OF THE REQUIREMENTS
FOR
THE DEGREE OF MASTER OF SCIENCE
IN
METALLURGICAL AND MATERIALS ENGINEERING

SEPTEMBER 2012

Approval of the thesis:

PREPARATION OF BZT-BCT THIN FILMS BY CHEMICAL SOLUTION DEPOSITION AND THEIR CHARACTERIZATION

submitted by **BARIŞ ÇELTİKÇİ** in partial fulfillment of the requirements for the degree of **Master of Science in Metallurgical and Materials Engineering Department, Middle East Technical University** by,

Prof. Dr. Canan Özgen
Dean, Graduate School of **Natural and Applied Sciences** _____

Prof. Dr. Cemil Hakan Gür
Head of Department, **Metallurgical and Materials Engineering** _____

Prof. Dr. Ahmet Macit Özenbaş,
Supervisor, **Metallurgical and Materials Engineering Dept.,METU** _____

Examining Committee Members:

Prof. Dr. Raşit Turan
Department of Physics, METU _____

Prof. Dr. Cevdet Kaynak
Metallurgical and Materials Engineering Dept., METU _____

Prof. Dr. A. Macit Özenbaş,
Metallurgical and Materials Engineering Dept., METU _____

Assoc. Prof. Dr. Burcu Akata Kurç,
Micro and Nanotechnology Dept., METU _____

Asst. Prof. Dr. Y. Eren Kalay,
Metallurgical and Materials Engineering Dept., METU _____

Date: 10.09.2012

I hereby declare that all information in this document has been obtained and presented in accordance with academic rules and ethical conduct. I also declare that, as required by these rules and conduct, I have fully cited and referenced all material and results that are not original to this work.

Name, Last Name: Barış ÇELTİKÇİ

Signature:

ABSTRACT

PREPARATION OF BZT-BCT LEAD-FREE THIN FILMS BY CHEMICAL SOLUTION DEPOSITION AND THEIR CHARACTERIZATION

Çeltikçi, Barış

M.S., Department of Metallurgical and Materials Engineering

Supervisor: Prof. Dr. Ahmet Macit Özenbaş

September 2012, 98 pages

In the presented thesis, lead-free $Ba(Ti_{0.8}Zr_{0.2})O_3$-$(Ba_{0.7}Ca_{0.3})TiO_3$ (BZT-BCT) thin films were deposited on $Pt/TiO_2/SiO_2/Si$ substrates using chemical solution deposition method and then the effect of process parameters were investigated to obtain optimum parameters of these lead-free thin films. The phase was selected near to the morphotropic phase boundary (MPH) to increase the number of polarization directions where rhombohedral and tetragonal phases exist together.

In this study, the effect of sintering temperatures on microstructure, dielectric and ferroelectric properties were studied systematically. Among the various high-quality BZT-BCT thin films with uniform thickness, the optimum dielectric and ferroelectric responses were observed for films annealed at 800 ^oC for 1 h sintering time. The thickness was kept constant for all measurements as 500 nm (triple layered films). Therefore, the average grain sizes were found around 60 nm for samples sintered at 700,750 and 800 ^oC.

BZT-BCT thin films sintered at 800 ^oC showed effective remnant polarization and coercive field values of 2.9 $\mu C/cm^2$ and 49.4 kV/cm, together with a high dielectric

constant and low loss tangent of 365.6 and 3.52 %, respectively, at a frequency of 600 kHz due to pure perovskite phase showing full crystallization and minimum surface porosity obtained at this temperature.

Keywords: Chemical Solution Deposition, Lead-Free Thin Films, BZT-BCT, Ferroelectric Properties, Dielectric Properties.

ÖZ

KURŞUN İÇERMEYEN BZT-BCT İNCE FİLMLERİN KİMYASAL ÇÖZELTİDEN BİRİKTİRME YÖNTEMİYLE HAZIRLANIŞI VE KARAKTERİZASYONU

Çeltikçi, Barış
Yüksek Lisans, Metalurji ve Malzeme Mühendisliği Bölümü
Tez Yöneticisi: Prof. Dr. Ahmet Macit Özenbaş

Eylül 2012, 98 sayfa

Yapılan tez çalışması kurşunsuz baryum titanat esaslı $Ba(Ti_{0.8}Zr_{0.2})O_3$-$(Ba_{0.7}Ca_{0.3})TiO_3$ (BZT-BCT) ince filmlerin $Pt/TiO_2/SiO_2/Si$ altlıkları üzerine kimyasal çözelti biriktirme yöntemiyle büyütülmeleri ve denenen süreç parametrelerinin en uygun film üretimi üzerine etkisinin araştırılmasıdır. İdeal film üretiminin gerçekleştirilmesi amacıyla kompozisyon rombohedral-tetragonal fazların bir arada gözlemlendiği morfotropik faz sınırına yakın seçilmiştir.

Bu çalışmada, üretilen filmlerin ferroelektrik ve dielektrik özelliklerinin birbirleri ile olan ilişkisi ve sinterleme sıcaklıklarının ince filmlerin mikroyapı ve morfolojisi üzerine olan etkisi sistematik bir şekilde çalışılmıştır. Uygulanan değişik sinterleme sıcaklıkları içerisinde, en uygun ferroelektrik ve dielektrik özellikler 800 °C'de 1 saat süreyle sinterlenen, homojen yüzeylere sahip filmlerde gözlemlenmiştir. Bütün çalışma boyunca, film kalınlığı 500 nm (üç katmanlı film) olarak sabitlenmiştir. Buna bağlı olarak ortalama tane boyutu yaklaşık 60 nm olarak 700, 750 ve 800 °C'de sinterlenen filmlerden elde edilmiştir

En iyi özellikler 800 °C'de sinterlenen filmlerde elde edilmiş olup, kalıcı polarizasyon 2.9 $\mu C/cm^2$ ve koersiv alan 49.4 kV/cm olarak hesaplanmıştır. Bu

filmlerde dielektrik sabiti ve dielektrik kaybının 600 kHz frekansta elde edilen değerleri de sırasıyla 365.6 ve % 3.52 olarak bulunmuştur. Bunun nedeninin 800 °C'de sinterlenen filmlerde tam kristalizasyon neticesinde oluşan saf perovskit fazı ve düşük yüzey porozitesinden kaynaklandığı düşünülmektedir.

Anahtar Sözcükler: Kimyasal Çözelti Biriktirme, Kurşunsuz İnce Filmler, BZT-BCT, Ferroelectrik Özellikler, Dielektrik Özellikler.

To my family

ACKNOWLEDGEMENTS

First of all, I would like to express my sincere gratitude to my supervisor Prof. Dr. Macit Özenbaş for his support, guidance, impatience, supervision and encouragement during the study.

I would like to thank to Dr. İbrahin Çam for his help during the dielectric measurements and for his comments. I am also very grateful to all the staff of the Department of Metallurgical and Materials Engineering and Central Laboratory staff for all measurements.

I must thank to Surface Science Research Laboratory staff Burak Coşar, Murat Güneş, Halil İbrahim Yavuz, Kerem Çağatay İçli and Berk Akbay for their endless support and friendship.

Finally, I would like to express my deepest gratitude to my family for sharing my hard times with me and their love, support and patience during my life.

TABLE OF CONTENTS

LIST OF TABLES

TABLES

LIST OF FIGURES

FIGURES

CHAPTER 1

INTRODUCTION

For the second half of the last century, the lead based compositions attracted great interest for ferroelectric, piezoelectric and dielectric applications, from microphones to high quality scanning electron microscopes, actuators, sonar sensors, cell phones, micro electromechanical systems (MEMs) and etc… [1], in the electronic industry. Among the applications as thin films and ceramics, piezoelectric thin films have attracted a great deal of attention because of many advantages. These are low operating voltages, high economical market as MEMs, and greater design flexibility with lithographic processes to fabricate [2].

In particular, the PZT phase (lead zirconate titanate) as a thin film shows superior properties in consequence of the existing of morphotropic phase boundary (MPB) on its phase diagram which allows the coexistence of two ferroelectric phases together. This coexistence of the phases cause higher polarization with zero energy barrier on polarization rotation from tetragonal to rhombohedral or rhombohedral to tetragonal directions [3].

There are many production techniques for PZT thin films as pulsed laser deposition (PLD), molecular beam epitaxy (MBE), chemical vapor deposition (CVD), magnetron sputtering (PVD) and chemical solution deposition (CSD). Among them, two methods have given prominence which are chemical solution deposition and pulsed laser depositon techniques to observe columnar and dense structures for perovskite oxides. However, physical vapor deposition techniques (such as pulsed laser deposition) fail to display chemical homogeneity during the formation of complex phases in the whole structure. Therefore, chemical solution deposition

remains as a suitable, low cost and highly flexible technique for the fabrication of perovskite oxides in the form of thin films. Consequently, the chemical solution deposition technique was selected for the entire study to determine ferroelectric and dielectric properties of the lead-free compositions [4].

Although there are large number of advantages of PZT materials, the lead based compositions are problematic for health because of their toxicity due to lead content and it is prohibited to use in European Union and Japan in civil applications [5-6]. Thereupon, alternative phases have been studied during the last decade instead of PZT material. There have been offered three main lead free families which are barium titanates, alkaline niobates and bismuth sodium titanates and their combinations for this purpose.

After the discovery of the ferroelectric property in potassium niobate, $KNbO_3$ (KN) by Matthias in the 1950s [7], some modifications on KN structure were performed. Therefore, KN-based compositions such as potassium sodium niobate (KNN) were the most attractive ones by the work of Saito et al. [5], that show remarkable piezoelectric properties.

Bismuth sodium titanate (BNT) perovskite ferroelectrics have also been considered as lead free systems for applications since the work by Smolenski in 1961 [6]. However the main problem in those pure types of systems is large coercive field and dielectric losses due to porosity which lead to the insufficient poling thus yielding moderate piezoelectric properties [2].

Third group of lead-free materials is barium titanate based compositions. This phase has been generally used as an addition to have dense microstructures of KNN and BNT systems. However, currently, the enormous piezoelectric coefficients have been published with some modifications of the barium titanate phases through the addition of calcium, zirconium and tin [8-11]. This is because of the lead-based compositions and barium titanate based compositions have tricritical point on their phase diagrams. If the film is produced exactly at this point, this situation causes zero energy barrier

for the change of polarization rotation from tetragonal to rhombohedral, or vice versa. However, there is polymorphic point in the phase diagrams of KNN and BNT based materials and this situation results with serious energy barrier for polarization rotation and decreases polarization and piezoelectricity [12].

Although the bulk forms of barium titanate based $Ba(Ti_{0.8}Zr_{0.2})O_3$-$(Ba_{0.7}Ca_{0.3})TiO_3$ compositions were studied effectively, the film production of this phase was not examined, yet. Therefore, the aim of the study is the growth of this new phase as a thin film. The ferroelectric, dielectric and piezoelectric coefficients were determined with a systematical study. The precursor was prepared carefully to form homogeneous and crack free films. The thermal properties were determined using thermal analysis of the powder form of the phase and correlated with phase analysis, ferroelectric properties and dielectric properties. Thus, optimum conditions for the production of these films were determined with correlations to the electrical properties and phase analysis in the study.

This thesis is consisting of five chapters. In the beginning, a wide literature search was mentioned. The lead-free families in the literature for the film form of piezoelectric materials were explained in detail with comparisons of ferroelectric, dielectric and piezoelectric properties. Theoretical approaches for ferroelectric, dielectric and piezoelectric properties were done. The importance of perovskite structure was touched, briefly. In the third chapter, all experimental details were given for the production of the films that consist of spin coating, heat treatment and characterization of the films. The results were discussed in chapter 4 with all optimizations, approaches, phase analysis, thermal analysis, ferroelectric and dielectric responses. Conclusions and further suggestions were given in chapter 5.

CHAPTER 2

LITERATURE SURVEY

2.1 Dielectric Properties of Materials

2.1.1 Dielectric Properties

A dielectric material is an electrical insulator that has a polarization effect with applied voltage on the material. There is a dipole structure in these materials which means electric charges do not flow inside the material but they are separated from each other on opposite directions causing dielectric polarization [13].

A capacitor is a device used for charge storage on its' parallel plates, one plate becomes positively charged, the other plate negatively charged, with an applied voltage. Each capacitor has a capacitance C. The capacitance (Farad) C is defined by the quantity of charge stored on either plate, Q (Coulomb),

$$C = \frac{Q}{V} \qquad \text{Eq. [2.1]}$$

with voltage V (Volt) applied across the capacitor. An empty capacitor, which is a condition of vacuum between the plates, can also be used in applications. In this situation,

$$c_o = \frac{\epsilon_0 \times A}{d} \qquad \text{Eq. [2.2]}$$

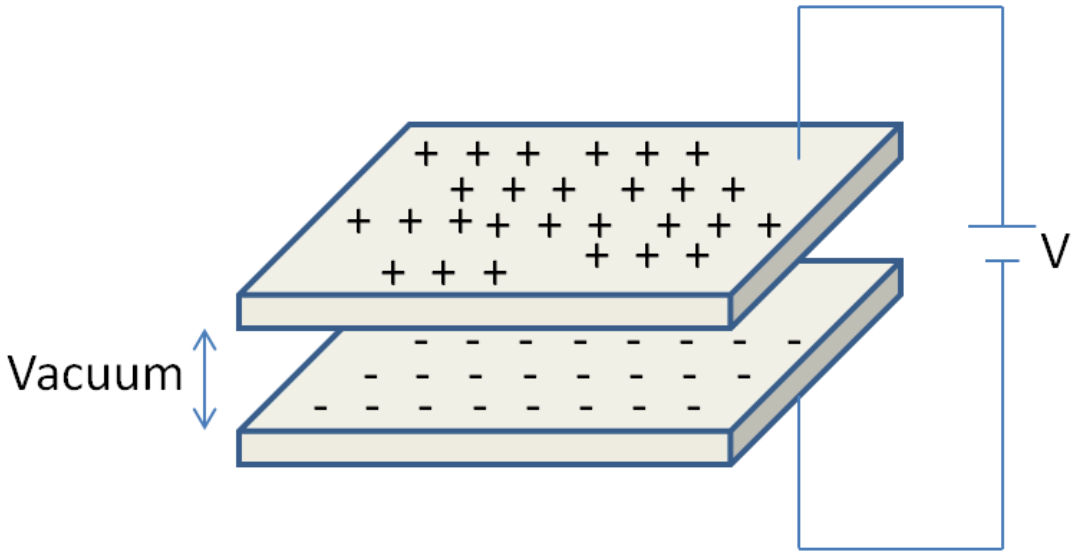

Figure 2.1 A parallel plate capacitor when vacuum is present between the plates.

where ϵ_o is permittivity of vacuum, 8.85×10^{-12} F/m, A is area of plates and d is the distance between the plates. If a dielectric material exists between the plates, the equation becomes,

$$C = \frac{\epsilon \times A}{d} \qquad \text{Eq. [2.3]}$$

where ϵ is the permittivity of this dielectric medium, d is the thickness for the dielectric medium and A is the contact area for the measurement [14]. The relative permittivity ϵ_r, mostly called as dielectric constant (K), is the ratio between the charge stored on an electrode slab of material brought to a given voltage and the charge stored on a set of identical electrodes separated by vacuum.

$$\epsilon_r = \frac{\epsilon}{\epsilon_o} \qquad \text{Eq. [2.4]}$$

Therefore, the dielectric constant can be written in terms of measured capacitance,

$$C = \frac{\epsilon_r \times \epsilon_o \times A}{d} \qquad \text{Eq. [2.5]}$$

where ϵ_r is dielectric constant of thin film (form of material which we are searching), ϵ_o is the permittivity of vacuum, 8.85×10^{-12} F/m, A is the contact area (mercury probe area which we are using), d is the thickness of the film.

With alternating voltages, the charge stored on a dielectric has both real (in phase) and imaginary (out of phase) components, caused by either resistive leakage or dielectric absorption. The loss is expressed by the ratio of the out-of-phase component to the in-phase component. This is D, the dissipation factor or the dielectric loss, also frequently called as the loss tangent, tan δ in the literature. Figure 2.2 illustrates the situation with circuit diagrams.

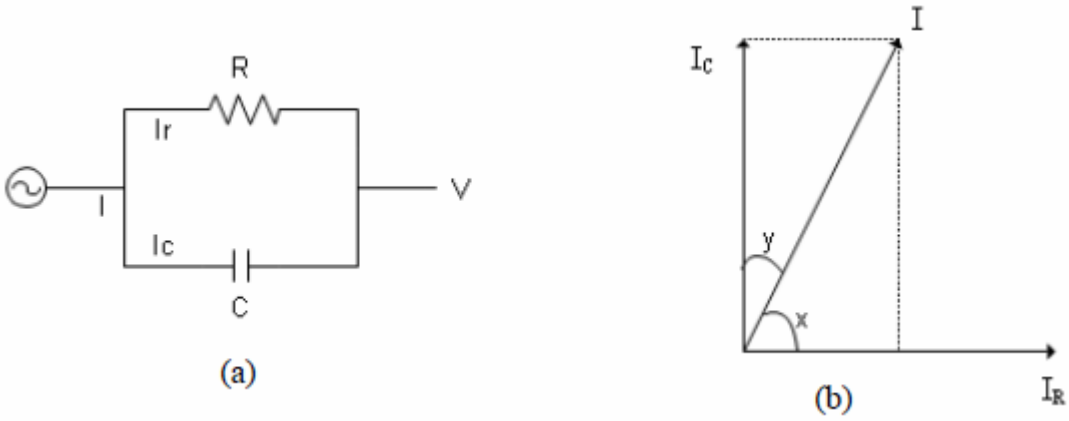

Figure 2.2 Circuit diagrams (a) charging and loss current (b) vector drawing of loss tangent for a typical dielectric [15].

In vector notation, the total current is the sum of the charging current and the loss current. The angle y (known as δ) is between the vector for amplitude of the total current and that for amplitude of the charging current is the loss angle, and the tangent of this angle is the loss tangent.

$$\tan \delta = (\text{loss current})/(\text{charging current}) = \frac{\epsilon''}{\epsilon'} \qquad \text{Eq. [2.6]}$$

where ϵ'' is the imaginary component and ϵ' is the real component of the permittivity [16].

2.1.2 Polarization

In the theoretical explanation of capacitance, the best way is the description of polarization mechanisms for the dielectric materials. There are electric dipoles which are possible opposite (positive and negative) charges separated by a certain distance that is illustrated in Figure 2.3

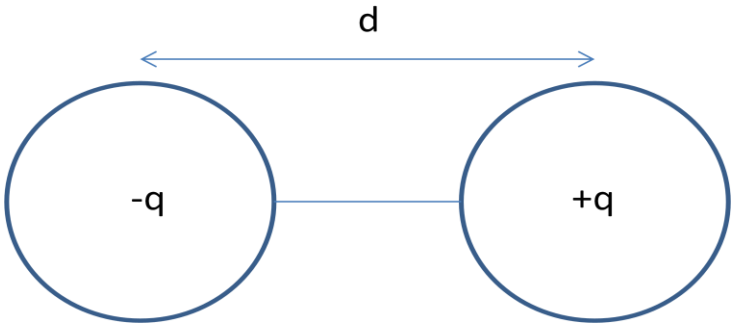

Figure 2.3 An electric dipole which consists of two electric charges.

An electric dipole moment $\boldsymbol{p}$ is associated with each dipole as follows:

$$\boldsymbol{p} = q \times d \qquad \text{Eq. [2.7]}$$

where q is the magnitude of each dipole charge and d is the distance between them. The polarization is alignment of dipole moments with an external electric field in the applied field direction. There are three types of polarization in materials as electronic, ionic and orientation polarization and dielectric materials exhibit at least one of these polarization types depending on material [13].

Upon the application of an external field, the electrons are displaced slightly with respect to the nuclei; induced dipole moments result and cause the so-called electronic polarization of the materials. When atoms of different types from molecules, they will normally not share their electrons symmetrically, as the electron clouds will be displaced toward the stronger binding atoms. Thus atoms acquire charges of opposite polarity, and an external field acting on these net charges will tend to change the equilibrium positions of atoms themselves. By these displacements of charged atoms or group of atoms with respect to each other, a second type of induced dipole moment is created; it represents the atomic polarization of the dielectric material. The asymmetric charge distribution between the unlike partners of a molecule gives rise, in addition to, to permanent dipole moments which exist also in the absence of an external field. Such moments experience a torque in an applied electric field that tends to orient them in the field direction. Consequently, an orientation (dipole) polarization will arise [17].

The total polarization $\boldsymbol{P}$ of a substance is equal to the sum of the electronic, ionic and orientation polarizations ($\boldsymbol{P_e}$,$\boldsymbol{P_i}$, and $\boldsymbol{P_o}$, respectively), or

$$\boldsymbol{P} = \boldsymbol{P_e} + \boldsymbol{P_i} + \boldsymbol{P_o} \qquad \text{Eq. [2.8]}$$

2.2 Ferroelectric Properties of Materials

2.2.1 Ferroelectric Phenomena

Ferroelectricity is described generally with the presence of spontaneous polarization in a crystal which has some polarization directions depending on the crystal type. This spontaneous polarization can be increased or decreased with applied voltage in polarization directions for ferroelectric materials. The spontaneous polarization is the non-equilibrium position of centre atom in the crystal [13].

Figure 2.4 shows the perovskite structure for both (a) cubic and (b) tetragonal phases. Perovskite crystals has a general formula ABO_3, where A atoms (Ba^{+2} and Ca^{+2} for our system) represent cations which are in the corners of the unit cell, and B atom (Zr^{+4} or Ti^{+4} for us) represents a cation which is in the center of crystal and O^{-2} is oxygen anions which surround the B type of atoms in an octahedra.

Above the Curie temperature, which is a phase transition temperature that the spontaneous polarization disappears, the crystal has cubic structure and centro-symmetric position of centre atom resulted with no dipole moment. Figure 2.4 illustrates both of the centrosymmetric and non-centrosymmetric situations. Below the Curie temperature cubic perovskite phase changes to tetragonal phase and B type atoms move in the O_6 octahedra because of the internal stresses which are the reason for non-centrosymmetric position and spontaneous polarization, thus material becomes ferroelectric.

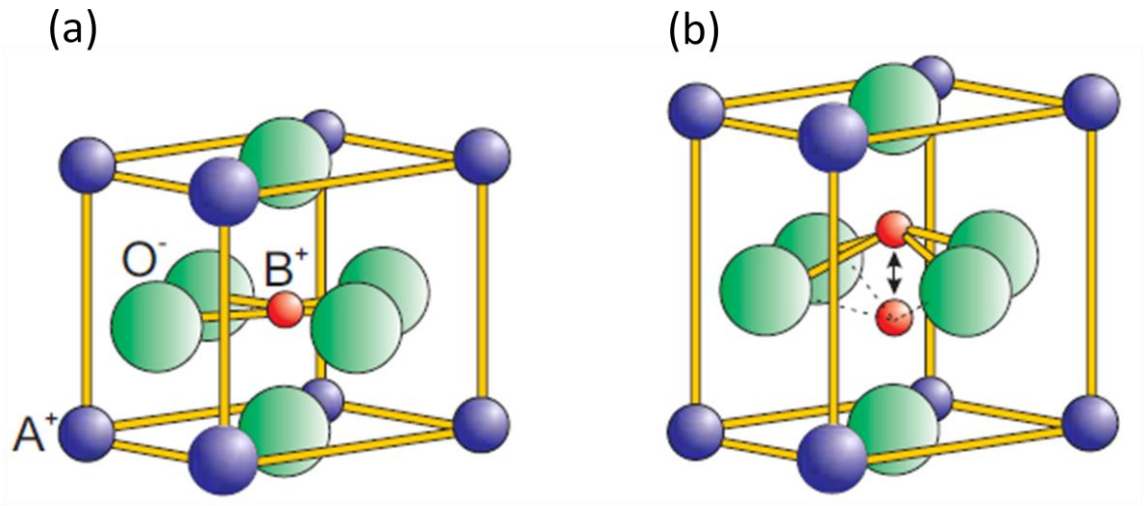

Figure 2.4 (a) Cubic and (b) tetragonal phases for perovskite oxides [14].

The definition of ferroelectricity is not well described with just the presence of spontaneous polarization; rather change of its orientation or decreasing/increasing of its polarization with an external field is essential. In this point the hysteresis loop has to be mentioned in detail which is seen in Figure 2.5. If an electric field is applied to the material, Ti atom moves in the direction of applied electric field and polarization reaches to maximum (from A point to D point). D point is the saturation point, P_s. If the field strength starts to decrease, some domains will back-switch, but at zero field the polarization is nonzero (point E). The value of polarization at zero field (point E) is called the remnant polarization, P_r. To reach a zero polarization state the field must be reversed (point F). The field necessary to bring the polarization to zero is called the coercive field, E_C. It should be mentioned that the coercive field E_C that is determined from the intercept of the hysteresis loop with the field axis is not an absolute threshold field. Further increase of the field in the negative direction will cause a new alignment of dipoles and saturation (point G). A completed cycle is resulted with hysteresis loop [15].

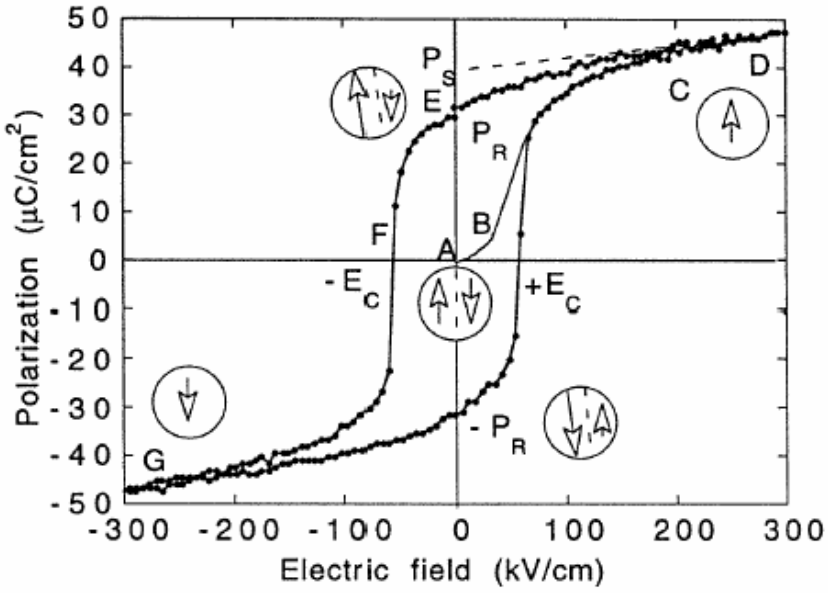

Figure 2.5 Ferroelectric (P-E) hysteresis loop. Circles with arrows represent the polarization state of the material at the indicated fields [15].

The domains are the regions that each grain has common orientation of spontaneous dipole moments below the Curie temperature. When there is no electric field, there is just spontaneous polarization since the dipole moments in the domains are aligned randomly, which is seen in Figure 2.6. When an electric field is applied to the material, the domains are oriented in the same direction by the movement of domains. If the applied electric field is removed some of the dipole moments remain in their aligned position. The remaining polarization is called the remnant polarization, P_r [18].

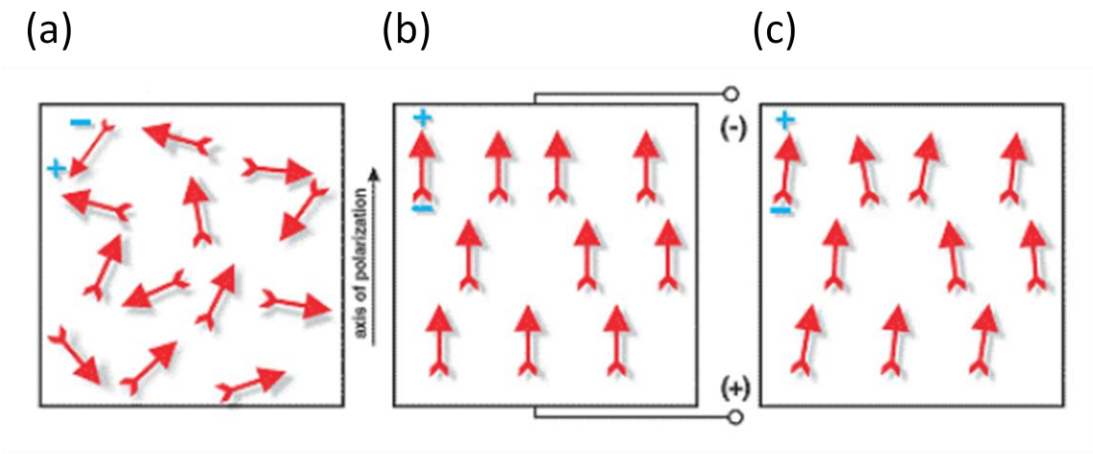

Figure 2.6 (a) Random polarization situation of domains in the material, (b) orientation of domains with applied voltage, (c) remnant polarization after the removal of applied voltage [19].

2.2.2 Ferroelectric Thin Film Applications

The ferroelectric effect was discovered by Valasek in 1921, in Rochelle salt. The molecular formula of this material was $KNaC_4H_4O_6 \cdot 4H_2O$. The effect was then not considered in applications for some time, and after a few decades later the effect came into great use. Today, the ferroelectric materials are used widely, mostly in memory applications. During the last four decades, these memory applications have been used frequently as Random Access Memories (RAM) and Read Only Memories (ROM). Some examples of these applications are Dynamic RAM (DRAM), Static RAM (SRAM), Electrically Programmable ROM (EPROM), Electrically Erasable ROM (EEPROM), etc. [20]. However these memories have lower write and read speed on working. In the late 1980s, the capacity and speed of these memories were increased dramatically with the help of ferroelectric random access memories (FeRAM) which depend on silicon based memory cells. Figure 2.7 shows structure of a 1 transistor of FeRAM.

Ferroelectric RAM (FeRAM, F-RAM or FRAM) has similar in construction to DRAM, however, uses a ferroelectric layer instead of a dielectric layer to achieve

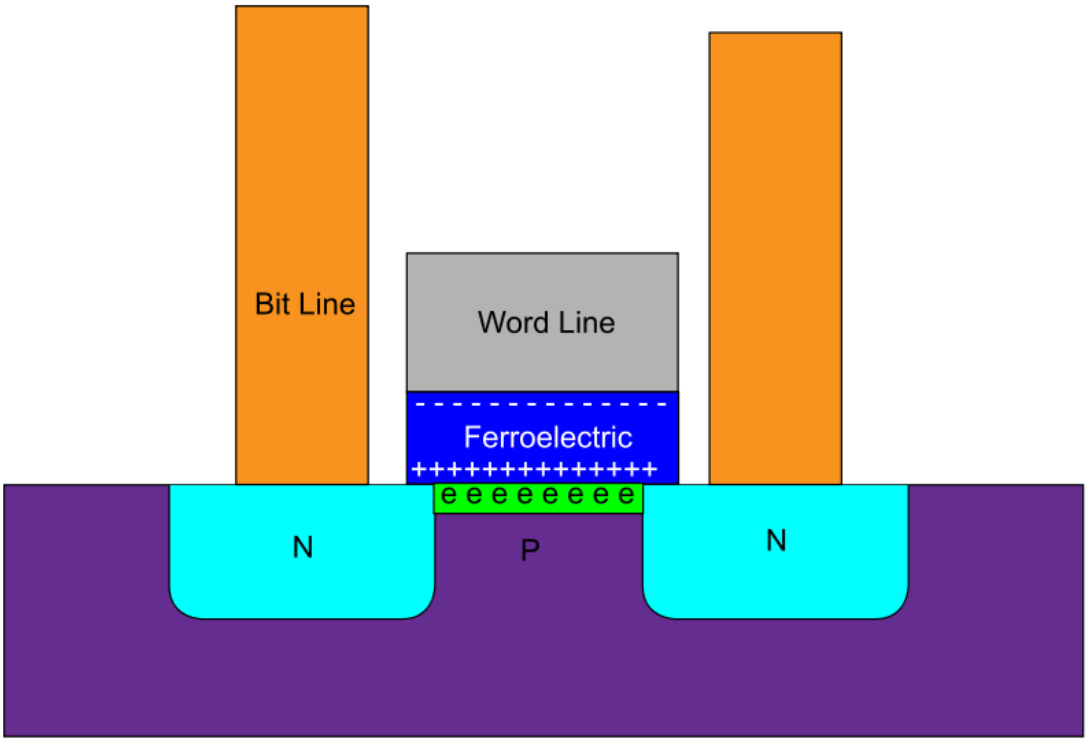

Figure 2.7 A transistor of a FeRAM [21].

non-volatility. FeRAM is one of attractive research area of non-volatile random-access memory technologies that offer the same functionality as flash memory. FeRAM advantages over flash memory such as lower power usage, faster writing performance and a much greater write-erase cycles (exceeding 10^{16} for 3.3 V devices) [23].

The important factor here for the usage of a ferroelectric layer is the thickness dependence for the minimum voltage necessities [22]. To be able to use a ferroelectric film on a transistor, the polarization voltage must be lower than 5 volts and effective switching can be achieved with lower than 1 micron thickness of ferroelectric material using 5 volts. Figure 2.8 illustrates the applied voltage dependence of thickness of the ferroelectric films. Of course the ferroelectric

material used is also important for this figure. Here, lead zirconate titanate is used for most of the applications.

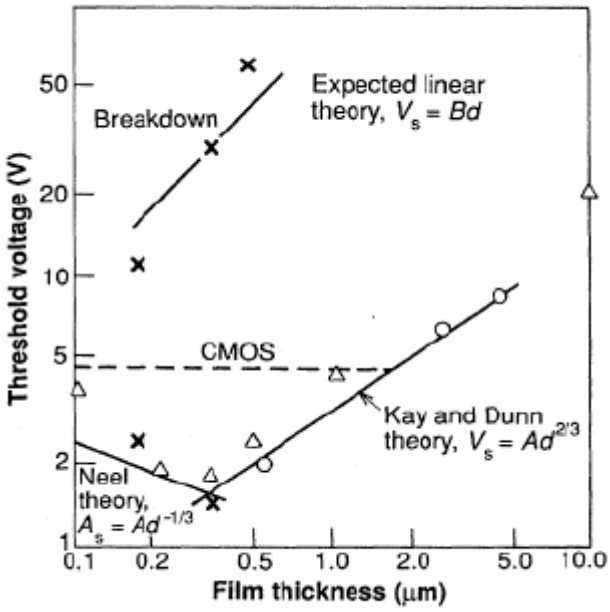

Figure 2.8 Switching voltage versus film thickness demonstrating the necessity of thin films [22].

2.3 Piezoelectric Properties of Materials

Piezoelectricity is a reversible effect that the mechanical stresses applied to the material will cause the generation of the electrical charge, which is named with direct piezoelectric effect, or reverse piezoelectric effect which is the change of dimensions of the material with applied electric field.

Lead zirconate titanate (PZT) is well known piezoelectric material that will be mentioned in detail in the next sections. In this type of material, applied voltage can result in 0.1% change in the dimensions. This percentage is enough to produce ultrasonic sensors. Also, the pressure applied to the PZT material can result to energy

generation which is one of the main energy harvesting research area in the world. Figure 2.9 shows the direct piezoelectric effect on the material with the applied voltage.

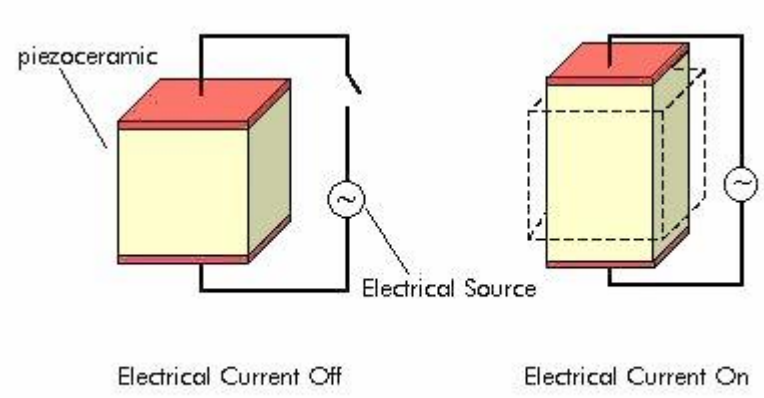

Figure 2.9 Change of the dimensions of the material with applied voltage [23].

2.3.1 Piezoelectric Charge Constant (d)

The piezoelectric charge constant, d, is the polarization produced per applied mechanical stress applied to a piezoelectric material or mechanical strain which is generated per applied electric field. The direct piezoelectric effect is,

$$D = dT + e^{T}E \qquad \text{Eq. [2.9]}$$

$$d = D/T \qquad \text{Eq. [2.10]}$$

where D is the dielectric displacement, T is the stress, and d is the piezoelectric charge constant (by using direct effect) [24-25].

Dielectric displacement D can be also described as the total surface charge density which is induced in the material by the applied field and can be expressed as,

$$D = \ Coulombs\ /Area(m^2)$$

T is the applied stress on the material and can be expressed as,

$$T = Force(Newton)/Area(m^2)$$

Thus, by applying these two definitions to the Equation [2.10] gives us,

$$d = Coulombs/Newton$$

the well known unit of piezoelectric charge constant, pC/N. This is mainly used as direct piezoelectric coefficient in most of the bulk applications of piezoelectric materials. As an example, the piezoelectric coefficient for BCT-BZT bulk material was reported as 620 pC/N [3].

The reverse effect of piezoelectricity can be created by applying an electric field which causes a dipole moment on the system. This dipole moment is a result of the movement of atoms which causes contraction or expansion on the bulk of the piezoelectric material due to applied electric field [26]. Then, the change in the dimensions of the material can be given as,

$$S = dE + s^E T \qquad \text{Eq. [2.11]}$$

$$d = S/E \qquad \text{Eq. [2.12]}$$

where S is the strain on the material, d is the piezoelectric coefficient and E is the applied electric field strength, d is the piezoelectric charge constant (by using reverse effect) [24-25].

Strain is the deformation by applied electric field on piezoelectric material that can be expressed as,

$$S = \Delta L/L \qquad \text{Eq. [2.13]}$$

Applied electric field can be expressed as,

$$E = V/m \qquad \text{Eq. [2.14]}$$

Thus, the application of Equation [2.13] and [2.14] to the Equation [2.12] gives us,

$$d = \text{Meter/Volt} \qquad \text{Eq. [2.15]}$$

This term is mostly used in piezoelectric thin film measurements because of the fact that applying a force to thin film is an insufficient way for piezoelectric measurements. As an example, the piezoelectric constant of PZT [58] is d~100 pm/V.

2.3.2 Piezoelectric Voltage Constant (g)

Another frequently used piezoelectric coefficient is the g constant which is named with piezoelectric voltage constant. The piezoelectric voltage constant, g, can be defined as electric field generated with applied mechanical stress to the material. Its usual units are meter volts/Newton, simplified from,

$$\frac{\text{volts/meter}}{\text{Newton/square meter}}$$

As an example, the piezoelectric voltage constant of $0.985(K_{0.5}Na_{0.5})NbO_3$-$0.015LiNbO_3$ system [65] was given as 36.2 mmV/N.

2.3.3 Electromechanical Coupling Factor (k)

The electromechanical coupling factor, sometimes named with piezoelectric coupling factor, k, is a dimensionless indicator that measures the ability of the piezoelectric material to convert electrical energy to the mechanical energy or mechanical energy to electrical energy [27]. Its explicit definition can be represented as shown below,

$$k^2 = \frac{\text{electrical energy converted to mechanical energy}}{\text{input electrical energy}} \qquad \text{Eq. [2.16]}$$

or,

$$k^2 = \frac{\text{mechanical energy converted to electrical energy}}{\text{input mechanical energy}} \qquad \text{Eq. [2.17]}$$

This dimensionless factor is always lower than 1, which means the energy conversation is never fully completed without loss. So, for most of the strong piezoelectric materials, the k factor can be about 0.7. The electromechanical coupling factor of BCT-BZT ceramic phase, the main phase mentioned in this thesis, was reported as 0.65 [10].

2.4 State of Art

Currently, the lead free research is a new surge with piezoelectric properties instead of lead based compositions for ceramics and thin film applications [30]. Over the last decade, the lead free thin film researches have been studied increasingly because of the highly input applications such as MEMs. However, there are lots of limitations on microstructure on the production of thin films. The aim of this thesis is the production of the most attractive lead free phase with a thin film production method, concisely.

The lead-free compositions were categorized as three main families, potassium niobates (KN), bismuth sodium titanates (BNT) and barium titanates (BT). In the

presented section the state of art techniques for lead free piezoelectric families are briefly described.

2.4.1 Potassium Sodium Niobates and Derivatives

Potassium sodium niobates (KNN) have been investigated as strongest candidate for the lead free piezoelectric phases because of the high Curie temperature, moderate ferroelectric responses, and large electromechanical coupling factor. However, the piezoelectric performance for pure KNN structures was just 100 pC N^{-1} [29]. Therefore, there was a need for some modifications on compositions, the most attractive one was Li modified compositions. A significant improvement was achieved by Saito et. al. [5], who is the pioneer for compositional modifications using Li, Ta, and Sb elements, with a piezoelectric coefficient of 416 pC N^{-1} in the composition of $(K,Na,Li)(Nb,Ta,Sb)O_3$. Hollenstain et. al. [30], investigated the electrical responses of $(K,Na,Li)(Nb,Ta)O_3$ composition and observed a piezoelectric coefficient of 290 pC N^{-1} with an effective electromechanical coupling factor of k_p=0.46 at x=0.03 and y= 0.20. Lin et. al. [31], also had a study of $(K,Na)_{1-x}Li_x(Nb_{1-y}Ta_y)O_3$ ceramics and observed that piezoelectric coefficient is 208 pC N^{-1} and electromechanical coupling factor is k_p=0.48 at x=0.04 y=0.225. Mn addition to the composition was another work for the modifications on the composition, $(K,Na,Li)(Nb,Mn,Ta)O_3$ [32].

Thus, all the modifications were for the decrease of the Curie temperature to be closer to the polymorphic point in their phase diagram which causes a significant decrease in the energy barrier for easy polarization rotation that results with higher piezoelectricity. Although there are investigations on potassium sodium titanate phase and their derivatives, the electrical properties, especially electrical responses, of these materials are not enough to be a good candidate instead of commercial lead based phases.

2.4.2 Bismuth Sodium Titanates and Derivatives

Bismuth sodium titanates (BNT) and their solid solutions have been considered as another main lead-free family for piezoelectric materials. First study was done by Smolenski in 1961, that BNT phase shows moderate piezoelectric performance and remnant polarization as 73 pC N^{-1} and 38 μC/cm^2, respectively, with a Curie temperature of 320 °C [6]. Advantages of this phase is easy production due to the use of non-volatile elements and lower process temperatures during the sintering stage compared to the KNN based compositions. However, one of the main disadvantages of BNT composition is its lower electromechanical coupling factor due to higher conductivity which can be understood from their high dielectric losses.

So, these factors lead the researchers for essential modifications on the BNT composition with some additive phases such as BNT-$BaTiO_3$ [33-37], BNT-$SrTiO_3$ [38], BNT-$PbTiO_3$ [39], BNT-$BiFeO_3$ [40-42], BNT-$BiKTiO_3$ [43], BNT-$BiScO_3$ [44], BNT-$NaNbO_3$ [45], BNT-$BiKTiO_3$-$BaTiO_3$ [46-47], BNT-$KNbO_3$-(Bi_2O_3.Sc_2O_3) [48], BNT-Ba(CuW)O_3 [49], $(NaBi)_{1-1.5x}La_xTiO_3$ [50], and $(Bi_{1-y}(Na_{1-x-y}Li_x))_{0.5}Ba_yTiO_3$ [51]. The well known additive phase is $BaTiO_3$ for decreasing the conductivity and porosity for better dielectric constants. Abazari et. al. [52] published a composition of (BiNa)TiO_3-(BiK)TiO_3-$BaTiO_3$ ternary system as a thin film produced by pulsed laser deposition technique with piezoelectric, ferroelectric and dielectric constants as $e_{31,f}$ = -2.25 C/cm^2, P_r^+ = 30μC/cm^2 and K ~ 575, respectively. Although the investigations on BNT-based phases continue, there are some thermodynamic restrictions of ternary systems which will be mentioned in the next section, BNT-based compositions still are not good candidates for lead-free alternatives.

2.4.3 Barium Titanate Based Compositions and BZT-BCT System

Another family of the lead-free alternatives is $BaTiO_3$ and compositional derivatives. Prior to about 1940, only a few types of salts were known as the ferroelectrics. Subsequently, the piezoelectric effect was discovered on $BaTiO_3$ phase. There were

three steps in the discovery of piezoelectricity. First one was the determination of a high dielectric constant in the $BaTiO_3$ composition by Thurnauer [53]. The second step was the assumption that this high dielectric constant was caused by the ferroelectricity of these materials. The third significant step was the discovery of the poling process. The poling process is the application of high voltage to the material to control electric moments of spontaneously polarized regions in desired direction. Thus, the first commercial piezoelectric device was discovered in the $BaTiO_3$-based compositions and used at World War II in the radars. In time, the lead zirconate titanate with various additives has become the dominant piezoelectric material as a result of very strong and stable piezoelectric properties.

During the last five decade, $BaTiO_3$ and derivatives have been mentioned as good dielectric materials instead of piezoelectric materials that is because of relatively high Curie temperature (~130 °C) [54]. This Curie temperature is far away from the room temperature which is the working temperature for most of the applications. Moving away from this tricritical (C-R-T) phase transformation temperature creates higher energy barrier for changing of polarization rotation between rhombohedral and tetragonal phases, that results with decreasing of the polarization [3]. This tricritical phase transition temperature can be decreased by doping of either A or/and B site substitutions, e.g., the addition of calcium into barium site or zirconium into titanium site in the $BaTiO_3$ structure [55-56]. While the Ca^{+2} addition decreases the Curie temperature to around room temperature, the doping of Zr^{+4} increases the electrical properties being chemically more stable than Ti^{+4} ions.

Recently, high piezoelectric responses have been reported due to compositional modifications on $BaTiO_3$ composition as $(1\text{-}x)Ba(Zr_{0.2}Ti_{0.8})O_3\text{-}x(Ba_{0.7}Ca_{0.3})TiO_3$ where x is 0.5. This composition will be referred as BZT-BCT from thereafter. The piezoelectric coefficient of this system was 620 pC/N, which is almost higher than the Pb-based system and much higher than other families (such as KNN-based d_{33}~416 pC/N [5], and BNT-based d_{33}~200 pC/N [48]). This comparison was illustrated in Figure 2.10. As it is seen, the piezoelectric performance of BZT-BCT system is twice than KNN-LT-LS phase and undoped PZT phase and also almost

higher than that of commercial PZT-based piezoelectric systems.

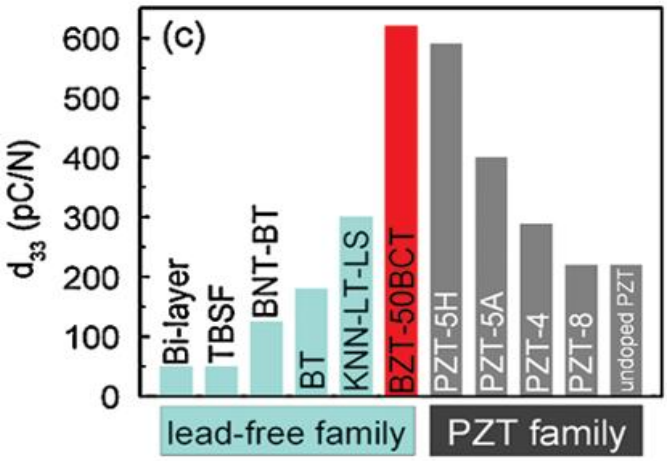

Figure 2.10 Comparison of some lead-free families and lead based-commercial products with BZT-BCT composition [3].

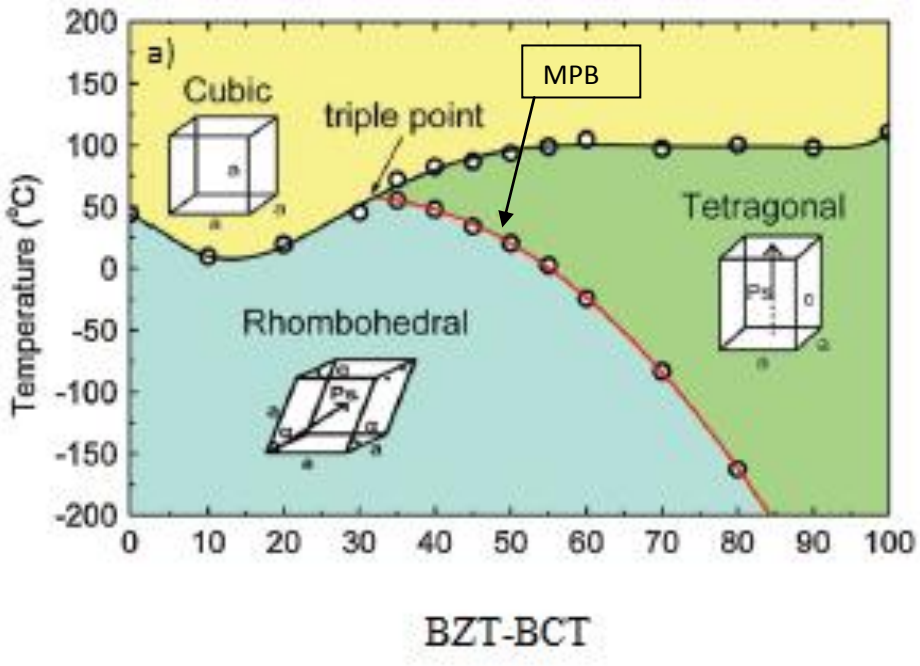

Figure 2.11 Phase diagram for BZT-BCT system which was determined by dielectric constant versus temperature curves in the Liu's work [3].

To explain these enormous piezoelectric values on BZT-BCT phase (Figure 2.11), a composition-based phase transition phenomenon has to be discussed in detail for perovskite oxides. This transition line in the phase diagram of perovskite oxides is known as "morphotropic phase boundary (MPB)". Basically, perovskite oxide's phase diagram has a line (MPB) that contains both of polarization directions as rhombohedral <111> and tetragonal<001>. This coexistence causes the instability of polarization state, so that the polarization direction can easily be rotated by any electric field [58-59].

Although most of the lead-free systems (KNN, BNT) have morphotropic phase boundary in their phase diagrams, it was unclear why these lead-free systems have lower piezoelectric coefficients (d_{33}~100-300 pC/N) than Pb-based systems (300-600 pC/N) and BZT-BCT system (d_{33}~620 pC/N) with existing theories. There is an explanation for this situation. The Pb-based and BZT-BCT systems have tricritical point (TCR) which is an intersection for the cubic, tetragonal (T) and rhombohedral (R) phases in their phase diagrams. In the explanations of Rossetti *et* al. [60] and Haun *et* al. [61], the free energy (F) for polarization rotation between R and T phases is a function of composition (x), temperature (T), magnitude of polarization (P), and its direction (**n**) that can be written as Landau polynomial (Equation 2.18).

$$F(x,T,\mathbf{n},P) = A(x,T)P^2 + B(x,\mathbf{n})P^4 + C(x,\mathbf{n})P^6 \qquad \text{Eq. [2.18]}$$

where A(x,T), B(x,**n**), and C(x,**n**) are the coefficients of second, fourth, and sixth order terms, respectively. When the composition is produced exactly on tricritical point in the phase diagram, this situation requires $B(x_{MPB},\mathbf{n}) = B(x_{TCP},\mathbf{n}) = 0$ and $C(x_{TCP},\mathbf{n}) = C(x_{TCP})$ [62]. So, the equation becomes,

$$F(x_{TCP},T,\mathbf{n},P) = A(x_{TCP},T)P^2 + C(x_{TCP})P^6 \qquad \text{Eq. [2.19]}$$

Therefore, the free energy for polarization rotation (F) becomes independent of polarization direction (**n)** when the composition is produced exactly on this tricritical point that can be seen in Equation 2.19. The disappearance of the anisotropy results

with zero energy barrier for polarization rotation from tetragonal state to rhombohedral state [60]. This is the main reason for enormous piezoelectric properties of the tricritical point type morphotropic phase boundary. In fact, the phase should not be produced on the tricritical point because of the fact that cubic phase does not show any piezoelectric effect. Any temperature instability, even 1 °C above the Curie temperature, is enough for the shift away from this C-R-T point, which can easily make the material non-piezoelectric by entering into the cubic region. So, the phase has to be produced on MPB near to the C-R-T point. In this situation the free energy of polarization rotation will not be zero as the above case, however it gives us very weak polarization anisotropy. This is resulted with very low energy barrier between <001>T and <111>R polarization states and the polarization rotation is still easy.

While $BaTiO_3$-based and PZT-based compositions have tricritical point type (C-R-T) MPB as shown in Figure 2.12(a1), present lead-free piezoelectric families (KNN-based and BNT-based) do not have a tricritical point type morphotropic phase boundary in their phase diagrams as shown in Figure 2.12(b1).

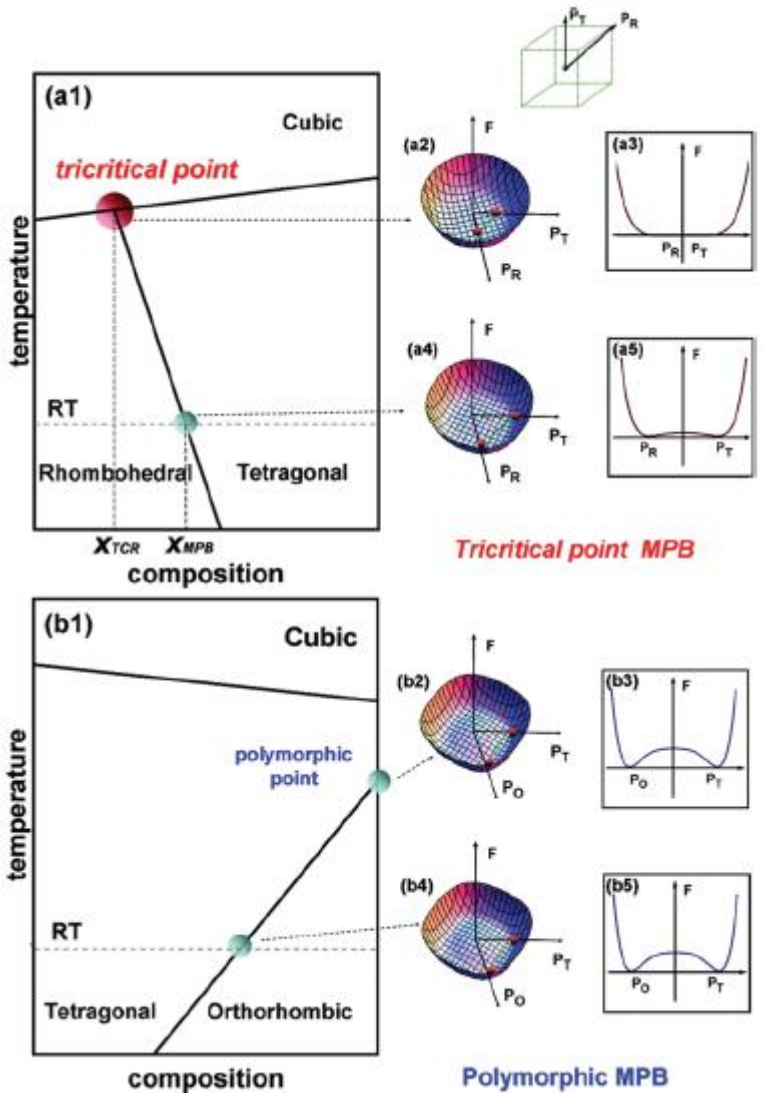

Figure 2.12 (a1) A part of phase diagram of BZT-BCT phase that includes tricritical point MPB. (a2) and (a3) Free energy diagram, which is isotropic, for polarization rotation between tetragonal and rhombohedral phases at C-R-T point. (a4) and (a5) Free energy diagram, which is anisotropic, for polarization rotation between <001>T and <111>R states on MPB. (b1) A typical phase diagram of polymorphic type MPB between tetragonal and orthorhombic phases. (b2) and (b3) Free energy diagram, which is anistropic, for polarization rotation between two ferroelectric crystal structures on intersection point. (b4) and (b5) Schematic anisotropic free energy diagram on polymorphic type MPB [3].

Polymorphic phase transition also exhibits an enhancement on piezoelectric properties because of the instability through coexistence of two ferroelectric crystal structures. However, there is much more anisotropy along the polymorphic MPB which results in larger energy barrier during the polarization rotation. Thus, lower polarization is obtained in the case of polymorphic MPB in comparison to tricritical type MPB.

Thus, the approach given above explains why higher piezoelectric coefficients can be obtained in the BZT-BCT (d_{33}~620 pC/N) and PZT-based compositions (d_{33}~300-600 pC/N) with respect to other lead-free familes (d_{33}~100-300 pC/N).

2.4.4 Lead-Free Thin Film Progress

Over the last decade, the researches on lead-free piezoelectric thin films have been constantly increasing. The families which are mentioned above were mainly used for thin film processing. However, thin film processing needs different approaches and experimental behaviors than ceramic (bulk) processing. The main problem of thin film production is volatilization of species (such as K^+, Na^+, Bi^{3+}, Ti^{4+}) during heat treatment or the precursor preparing stage. This problem was seen mostly in the chemical solution deposition or metal-organic deposition methods.

KNN-based compositions were fabricated using different techniques, such as magnetron sputtering [63], chemical solution deposition (CSD) [64-79] and pulsed laser deposition (PLD) [70]. As it is seen, the most attractive method of production of KNN-based compositions is chemical solution deposition method. While pure KNN composition $(K_{0.5}Na_{0.5})NbO_3$ [67] shows a moderate piezoelectric strain coefficient d_{33}~74.0 pm/V, the Li addition to this phase (Li,K, Na)NbO_3 [65] causes serious stoichiometric deviation and lattice defects in the Li-KNN films and results with higher piezoelectric strain coefficient d_{33}~83.1 pm/V which is much more close the PZT film d_{33}~100 pm/V [71]. Ta and Mn modified KNN thin films (KNL-x NMT, x = 0 to 0.2) were also studied systematically to improve ferroelectric and dielectric performance of KNN-based lead-free thin films [66]. In this phase 5 mole

% Mn addition plays an important role to decrease leakage current density. This study showed that 10 mol. % Ta doping results with d_{33}~61 pm/V piezoelectric strain coefficient which is lower than that of Goh's works [65,67]. However, the point of the study is to obtain improved ferroelectric and dielectric properties in the mentioned work as P_r~16.1 μC/cm^2 and ϵ_r~2649, respectively. The second method for the production of KNN-based compositions is pulsed laser deposition [70]. In this study, Mn-doped $(K_{0.44}Na_{0.52}Li_{0.04})(Nb_{0.84}Ta_{0.1}Sb_{0.06})O_3$ (KNN-LT-LS) thin films on $SrTiO_3$ substrates were examined. Piezoelectric strain coefficient of KNN-LT-LS phase was determined as ~45 pm/V for 500 nm Mn doped films.

The well studied second phase as an alternate to lead-free piezoelectric thin film is (Bi,Na)TiO_3-based compositions which were fabricated using chemical solution deposition [72-76] and pulsed laser deposition method [77,75]. Pure $Bi_{0.5}Na_{0.5}TiO_3$ films were deposited on Pt/Ti/SiO_2/Si substrates using CSD together with rapid thermal annealing [74]. In this study, moderate dielectric and ferroelectric properties were obtained as ϵ_r~277 and P_r~8.3 μC/cm^2, respectively. The doping of Ba^{2+} ions to the phase, $(Na_{0.5}Bi_{0.5})_xBa_{1-x}TiO_3$ (NBT-BT) 96/4, causes good insulating characteristics because of decreasing the porosity which was mentioned in the other study [75]. Dielectric permittivity and dielectric loss of the NBT-BT 96/4 phase was found as ϵ_r~740 and tan δ~5%. Zhang et. al. [73] studied the same composition (NBT-BT 96/4) with a different substrate and found additionally the piezoelectric constant of this phase as d_{33}~94 pm/V. Also, dielectric permittivity, dielectric loss and remnant polarization values were given as ϵ_r~504, tan δ~5% and 12 μC/cm^2, respectively in that study. Another BNT derivative is (1-x)BNT-xBKT composition [76]. At x=0.15, dielectric constant was found as ϵ_r~360 with a dielectric loss of tan δ~5.9%. The importance of this study is the improvement in ferroelectric properties (as remnant polarization) of P_r~13.9 μC/cm^2. $BaTiO_3$ addition to BNT-BKT $(0.88)(Bi_{0.5}Na_{0.5})TiO_3$-$(0.08)(Bi_{0.5}K_{0.5})TiO_3$-$(0.04)BaTiO_3$ was studied also by Abazari et. al. [52] on $SrRuO_3$ coated $SrTiO_3$ substrates. Dielectric permittivity and dielectric loss was given as ϵ_r~750 and tan δ~15% while piezoelectric voltage coefficient and remnant polarization was found to be -2.2 C/m^2 and 30 μC/cm^2 which

is the highest obtained remnant polarization value in BNT based compositions. All properties of lead-free thin film families can be seen in Table 2.1.

Many recent studies have been reported for the preparation of $(Ba,Ca)(Zr,Ti)O_3$ derivatives for mostly bulk applications. Furthermore, there are a few studies about the production of thin films with this composition using mainly pulsed laser deposition and chemical solution deposition methods [78-81]. In these studies, dielectric properties of the $(Ba,Ca)(Zr,Ti)O_3$ thin films were studied in detail. While $(Ba,Ca)(Zr,Ti)O_3$ thin films show high dielectric constant around ϵ^r~1000 produced by pulsed laser deposition method [78,81], films of same composition show a moderate dielectric constant around ϵ^r~250 prepared using chemical solution deposition method [80]. This situation is explained by the presence of porosity in chemical solution deposited $BaTiO_3$-based thin films where the porosity is the source of moisture which causes a decrease in dielectric permittivity. In contrast, the pulsed laser deposition method results with dense and oriented films. Recently, only one study was exhibited all ferroelectric, dielectric and piezoelectric properties of this phase as P_r^+=14.1 $\mu C/cm^2$, ϵ^r~1010 and d_{33}=80 pm/V, respectively [78], using pulsed laser deposition method. Among the variety of process types, the chemical solution deposition method offers better control of the chemical composition and easy control of the process with a disadvantage of grain sizes and orientation control compared with physical vapor deposition methods. However, the control of the chemical composition is quite important to produce a material on morphotropic phase boundary for lower energy barrier to obtain optimum polarization. Moreover, the preparation of $Ba(Ti_{0.8}Zr_{0.2})O_3$-$(Ba_{0.7}Ca_{0.3})TiO_3$ composition using chemical solution deposition method and its ferroelectric and dielectric correlation have not been reported yet.

In this thesis, we determine the ferroelectric and dielectric properties of $Ba(Ti_{0.8}Zr_{0.2})O_3$-$(Ba_{0.7}Ca_{0.3})TiO_3$ composition prepared using chemical solution deposition method for different process parameters. Thus, optimum electrical properties were observed for BZT-BCT lead-free thin films using a systematic study.

Table 2.1 Ferroelectric, dielectric and piezoelectric properties of lead-free thin films in the literature.

Ref.	Composition		Piezoelectric displacement coefficient	Dielectric constant	Current density	Dielectric loss	Coercive field	Remnant polarization
			d33 (pm/V)	K (ϵ_r)	J (A/cm^2)	D (tan δ) (%)	E_c (kV/cm)	P_r (μC/cm^2)
[63]	$(K_{0.5}Na_{0.5})NbO_3$	[KNN]		450		1.7		12
[64]	$(K_{0.5}Na_{0.5})NbO_3$	[KNN]			10^{-7}		90 (at -190 °C)	20 (at -190 °C)
[65]	$0.985(K_{0.5}Na_{0.5})NbO_3$-$0.015LiNbO_3$	[KNN]	83.1	250		5		
[66]	$(K_{0.48}Na_{0.48}Li_{0.04})(Nb_{0.895}Ta_{0.1}Mn_{0.005})O_3$	[KNN]	61	2650			22.2	16.1
[67]	$(K_{0.5}Na_{0.5})NbO_3$	[KNN]	74	337	10^{-8}	3.2	50	4
[68]	$(0.06)LiNbO_3$-$0.94(K_{0.52}Na_{0.58})NbO_3$	[KNN]	192	625	10^{-5}		36.5	9.7
[69]	$(K_{0.4425}Na_{0.52}Li_{0.0375})(Nb_{0.8825}Ta_{0.0375}Sb_{0.08})O_3$	[KNN]		341		5	31.8	9.5
[71]	Mn-doped $(K_{0.44}Na_{0.52}Li_{0.04})(Nb_{0.84}Ta_{0.1}Sb_{0.06})O_3$	[KNN]	45				30	15
[72]	Pr^{3+} doped $Na0_{.5}Bi_{0.5}TiO_3$	[BNT]		772		4.6	94	18.3
[73]	$0.94(Na_{0.5}Bi_{0.5})TiO_3$-$0.06BaTiO_3$	[BNT]	94	504		5	103	12
[74]	$Na_{0.5}Bi_{0.5}TiO_3$	[BNT]		277	10^{-5}	2	200	8.3
[75]	$(Na_{0.5}Bi_{0.5})_{0.94}Ba_{0.06}TiO_3$	[BNT]		740	10^{-4}	5		9
[76]	$Bi_{0.5}$ $Na_{0.5}TiO_3$- $Bi_{0.5}K_{0.5}TiO_3$	[BNT]		360		5.9		13.8
[77]	$0.92(Na_{0.5}Bi_{0.5})TiO_3$-$0.08BaTiO_3$	[BNT]		820	10^{-9}	13	120	11
[52]	$0.88(Bi_{0.5}$ $Na_{0.5})TiO_3$-$0.08(Bi_{0.5}K_{0.5})TiO_3$-$0.04BaTiO_3$	[BNT]		600		20	95	30
[78]	$0.5[Ba(Ti_{0.8}Zr_{0.2})O_3]$-$0.5[(Ba_{0.7}Ca_{0.3})TiO_3]$	[BZT-BCT]	80	1010			17.7	2.5
[79]	$(Ba_{0.95}Ca_{0.05})(Zr_{0.2}Ti_{0.8})O_3$	[BZT-BCT]		900		5		
[80]	$(Ba_{0.95}Ca_{0.05})(Zr_{0.05}Ti_{0.95})O_3$	[BZT-BCT]		250	10^{-6}			
[81]	$(Ba_{0.90}Ca_{0.10})(Zr_{0.25}Ti_{0.75})O_3$	[BZT-BCT]		725		3		

2.5 Chemical Solution Deposition Technique

The sol-gel technique has been considered for more than 100 years. A sol is suspension of colloidal particles in a solution while the gel is a colloidal solid that has an internal network structure with mixed solid and fluid components. Sol-gel processing offers advantages over standard ceramic or glass processing for some electronic applications. The process is a series of wet chemical reactions occurring at relatively low temperatures. The chemical reactants are available in solution form which allows for distillation of the materials. Thus, high purity "raw materials" for electronic ceramics can be prepared in sol-gel process.

Multicomponent oxides can be formed via sol-gel processing. The individual constituents are combined as liquids resulting in atomic level mixing. The final material can be more homogeneous with respect to chemical species than could be expected from processing in which solid-state or melt-phase diffusion is necessary to get compound formation.

It should be noted that purity and homogeneity could also result from other types of solution preparation of electronic ceramics. These advantages result from the liquid nature of the reactants regardless of whether a powder or a monolithic gel is formed. These advantages, therefore, are not limited to sol-gel processing. The three dimensional network (rather than particulate) structure does allow for some additional advantages [82].

Before the gelation is complete, the material is still fluid. Films or coatings of desired compositions can be easily formed on a substrate. Another advantage is that after drying, the gel is porous. The pores in dried gels are often extremely small (approximately 10 nm). This allows lower firing temperatures to be used for sol-gel derived pieces than for standardly processed pieces. The low firing temperature of sol-gel derived material can also be important in compositions which undergo undesired phase transitions or have volatile components. It is possible in certain cases to process at sufficiently low temperatures, e.g. below the phase transition, thus

avoiding any deleterious effects. Categories of sol-gel processing technique were shown in Figure 2.13.

The properties of an electronic ceramic device result from composition of materials used as well as the micro and macrostructure of the piece. Because of the options available in each of the steps during sol-gel processing there can be somewhat independent control over porosity, crystal structure, and grain size. Sol-gel processing thus allows for a variety of compositions and structures to be formed. The resultant piece can, therefore, possess a unique combination of properties [82].

In review, due to the liquid nature of the constituents and the diversity of the processing variables possible, sol-gel processing can offer many advantages for use in electronic ceramics. They are: (1) purity, (2) homogeneity, (3) ease of forming a variety of structures, (4) low temperature processing, and (5) unique combination of properties.

The first usage of this technique for perovskite thin film production to produce electronic oxides dates from the mid-1980s. Publications by Fukushima et. al. [84] on the production of PZT (lead zirconate titanate) by sol-gel processing was the first study to obtain desired properties as thin films in comparison with bulk of PZT phase. With the help of this starter study, a wide range of metal oxides for electronic industry [$PbTiO_3$, $BaTiO_3$, $SrTiO_3$, $(Ba,Sr)TiO_3$, $Pb(Zr,Ti)O_3$, $Ba(Zr,Ti)O_3$, $Pb(Sc,Ta)O_3$, $Pb(Mg_{1/3}Nb_{2/3})O_3$, $SrBi_2Ta_2O_9$, $SrBi_2Nb_2O_9$, $(Bi_{1-x}La_x)_4Ti_3O_{12}$, $(La,Sr)CoO_3$, $(La,Sr)MnO_3$, $YBa_2Cu_3O_{7-\delta}$, $BaZr_xY_{1-x}O_3$ and etc.] were tried to be produced using this technique.

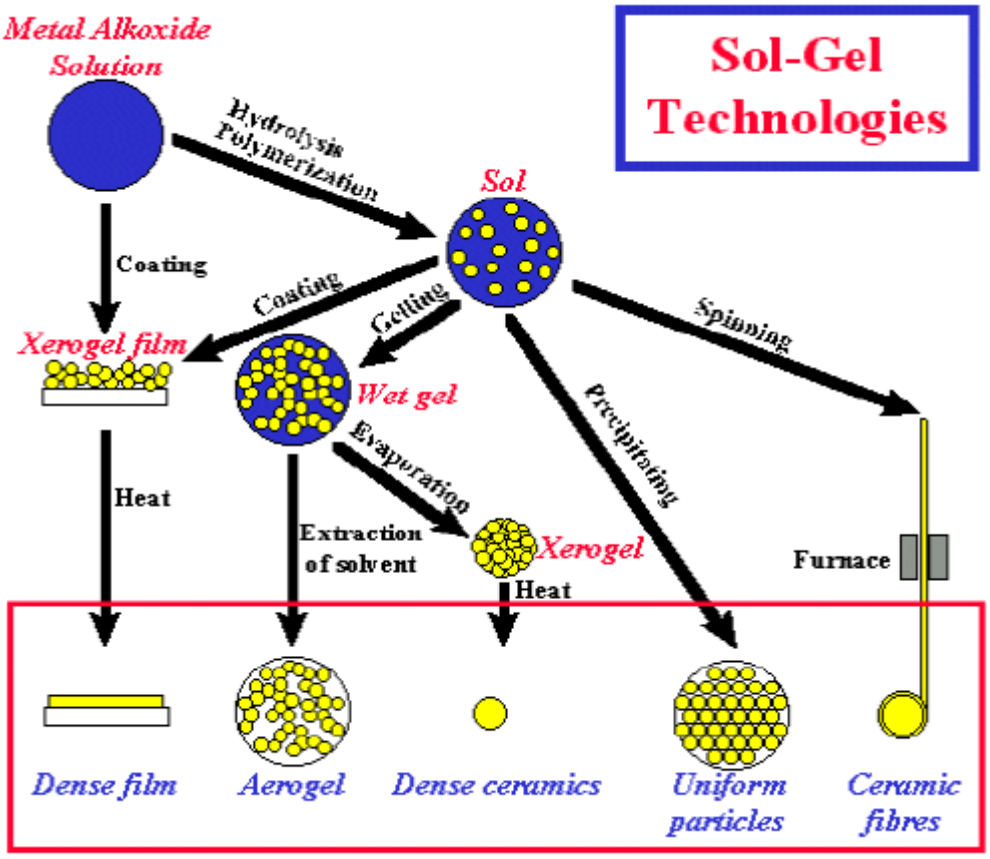

Figure 2.13 Categories of sol-gel processing technique. The route at the left in the figure, called chemical solution deposition, was used in current study [83].

2.5.1 Preparation of the Solution and Process Chemistry

Figure 2.14 illustrates the route of chemical solution deposition technique for thin film production. At first the precursor has to be prepared by mixing of appropriate amounts of metal-carboxylates and metal alkoxides and solvents. This stage is the most critical step for thin film production. Compositional stoichiometry is obtained in this stage and also the homogeneity of the solution is an important factor to obtain optimum film quality.

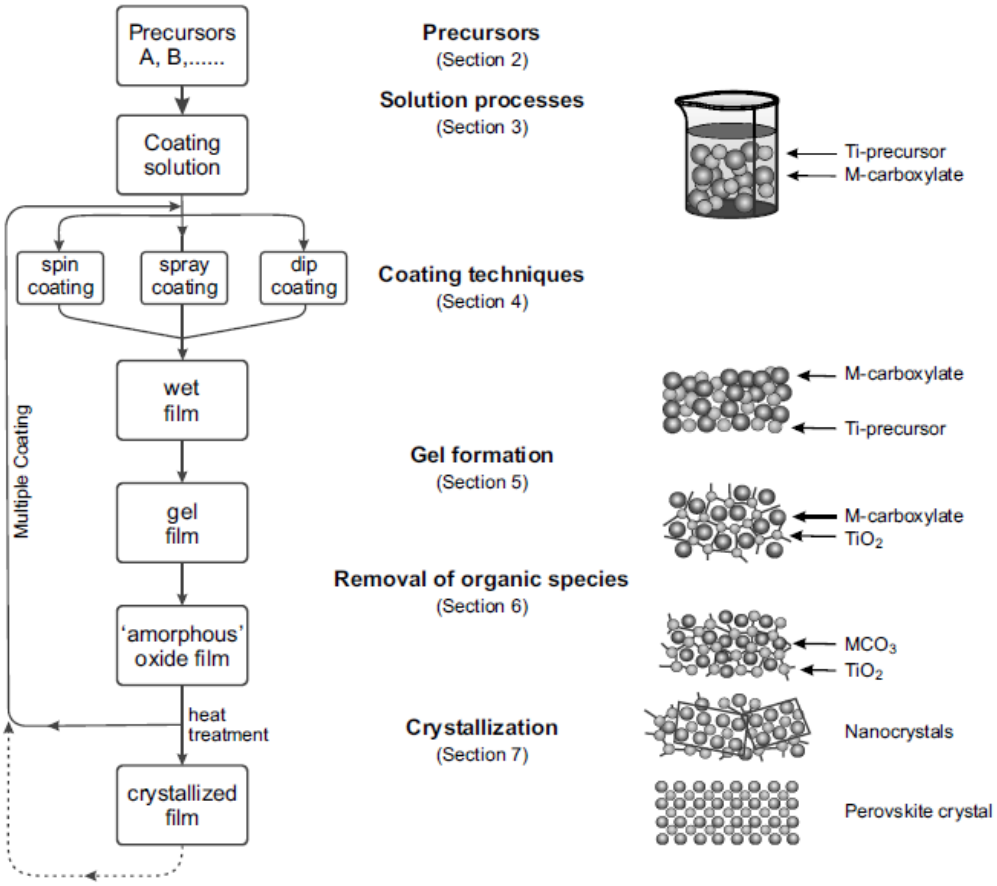

Figure 2.14 Flow chart of typical chemical solution deposition technique for thin film production [85].

Losses during the preparation of solution have to be considered carefully because of the volatile raw materials such as Pb-acetate, Na-acetate or Ti-isopropoxide. To obtain crack free films some chemical stabilizers, such as ethylene glycol, can be added to the solution.

Metal carbocylates are common salts of carboxylic acids, R-COOH, where R is alkyl group such as methyl, CH_3 (acetic acid) ethyl, C_2H_5, etc. Carboxylates can normally be dissolving in their own (parent) carboxylic acids [85]. This is important that Ba-acetate and Ca-acetate were dissolved in acetic acid in current study. Alcohols (R-OH) can be considered as weak acids, and metal salts of alcohols were called

alkoxides, M-$(OR)_x$, where M is the metal part. The key reactions which are leading to the formation of precursor species are hydrolysis and condensation.

Hydrolysis:

$$M(OR)_x + H_2O \longrightarrow M(OH)_x + {}_xROH \qquad \text{Eq. [2.20]}$$

Condensation (alcohol elimination):

$$2M(OR)_x(OH) \longrightarrow M_2O(OR)_{2x-3}(OH) + ROH \qquad \text{Eq. [2.21]}$$

Condensation (water elimination):

$$2M(OR)_x(OH) \longrightarrow M_2O(OR)_{2x-2}(OH) + H_2O \qquad \text{Eq. [2.22]}$$

These reactions cause the formation of a metal-oxygen-metal bridge, which can be considered as the backbone of any oxide ceramic structure. Continued condensation process increases the density of metal-oxygen-metal crosslinks until gelation or precipitation occurs.

2.5.2 Spin Coating Process

Once the precursor has been prepared, there are three techniques for coating of the films which are spin coating, spray coating and dip coating, as illustrated in Figure 2.15. In most of the researches, the spin coating process has been used generally. The electroded (Pt is used for this purpose) Si substrates are the best ones for piezoelectric applications. This substrate is held on the spin coater with the help of vacuum or double sided sticker from back side of the wafer. The spin rate (in rpm) and time are controlled to achieve desired thickness. The controlling of thickness is

quite important for a systematical study. The collaboration of precursor molarity, spin rate and spin time affect directly the thickness of the film. For example, while 0.1 molar solution with 3000 rpm spin rate and 30 s spin time gives around ~10 nm thickness, 0.85 molar solution with 1500 rpm and 30 s spin time results with ~150 nm film thickness.

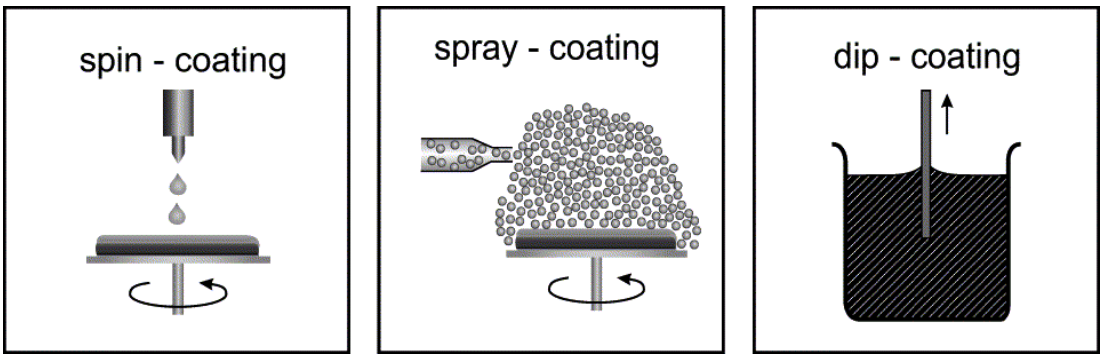

Figure 2.15 Commonly used coating processes for the electronic oxides using chemical solution deposition method [85].

A variety of defects can be seen when spin coating process is used. Any dirt (particles mostly) from precursor or atmosphere will stick to the surface during spin coating step. So, before the spin coating process, 0.2 µm nozzled filters has to be used to obtain clean precursors. The control of the particles in the atmosphere can be provided by the use of clean rooms.

According to Bornside et. al. [86], there are four stages during the spin coating process which are illustrated in Figure 2.15. First one is the depositon of precursor onto the substrate using a pipe. Usually the excess amount of solution is dropped to the wafer for wetting to the surface as well. The second stage is spin-up which has the aggressive fluid expulsion from the substrate by rotational speed. The next stage is the smoothing of the precursor with a constant speed rotation. The final step is the evaporation of solvents and gel formation. This is an important stage because of the thickness and smoothing of the films are determined on this gel formation stage.

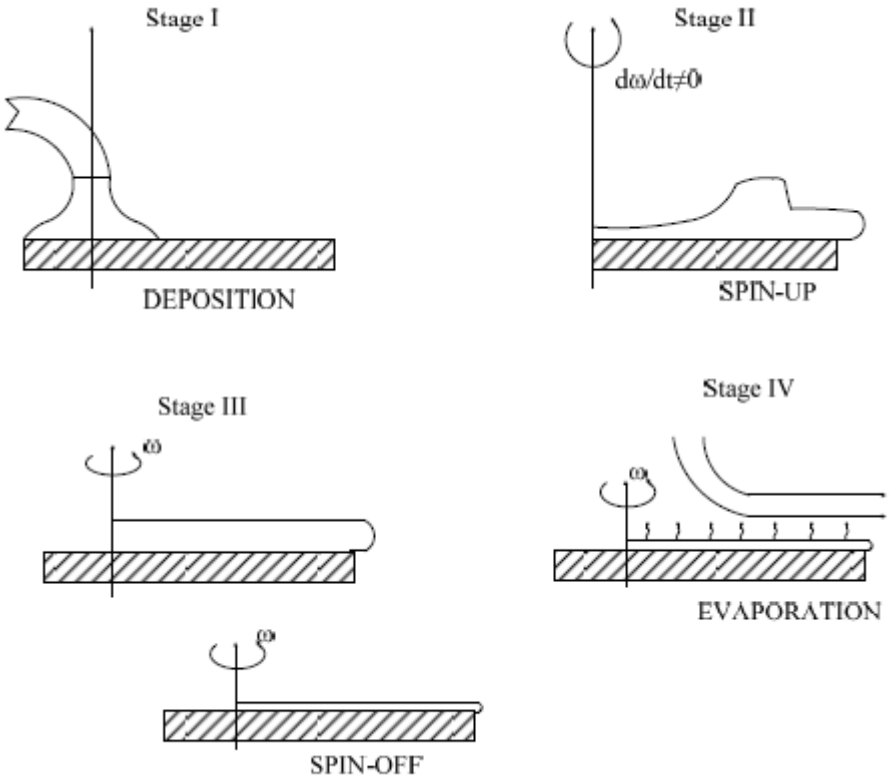

Figure 2.16 Stages during spin coating process [86].

The prediction of Mayerhofer about factors affecting the film thickness includes the spin rate (f), the initial viscosity (η_i), and the evaporation rate (e):

$$h \ \alpha \ f^{2/3} \ _i^{1/3} \ e^{1/3} \qquad \text{Eq. [2.23]}$$

2.5.3 Drying, Firing and Sintering of Perovskite Thin Films

After the spin coating step, the crystallization of the films were required to obtain perovskite oxides. To obtain desired perovskite phase, all solvents and organics (in the form of gel) have to be removed from the system. There are some stages during the heat treatment process of the film. The first one is the removal of solvents or water (if it exists) at relatively low temperatures (~150-200 °C). This step is named

as drying of the films. In this point it is necessary to say that all heat treatment process has to be determined with a well studied TG/DTA measurement. The timing during the steps was critical because of the fact that all reactions have to be completed before the next step.

There are two main approaches that are commonly used to complete crystallization of the films: the two step and the one step processes. Mainly the two step process is described as first the pyrolysis which is the removal of all organics at relatively low temperatures (~500 °C in our work) and then reaching to a high crystallization temperature (~800 °C in our work). This two step process is much more preferred option in the literature that allows crack-free films because of the fact that rapid thermal treatment processes tends to create cracked films. When the heat treatment occurs, the film has a shrinkage value along the thickness by 50 to 70%. So, it is an essential to fabricate multilayered films in each pyrolysis step (3 pyrolsis steps were used in our work to obtain desired thickness before the crystallization).

In the one step process, the material is heated directly to the crystallization temperature, which consists of both organic removal and perovskite formation. This one step process is named as rapid thermal annealing. This process is preferred mostly for the formation of highly crystalline and oriented films with a much lower film thicknesses because of the crystallization kinetics, and there are a few reports about this process for $BaTiO_3$ based phases [87-89]. The rapid thermal annealing also tends to enhance film densification by delaying the onset of crystallization to higher temperatures.

In the processing of $BaTiO_3$ based compositions, the formation of the carbonate phases complicates the annealing scheme. The reactions for phase transitions during the heat treatment include:

- The tiranium isopropoxide tends to create titanium oxide at temperatures 300-350 °C. This situation results with a mixture of titanium oxide secondary

phases and weak crystalline alkaline (Ba,Ca for our study) carboxylate netwoks.

- The exact barium carboxylates occur at relatively high temperatures (450-500 °C). This is pyrolysis step and has to be waited enough to complete.
- During the heat tratment, the secondary phases occur at the bulk of the film. These are mostly complex carbonates, $Ba_2Ti_2O_5CO_3$ which is an intermediate phase [90]. Mostly, this phase causes the increase in annealing temperatures to higher temperatures.

2.6 Viscosity of the Solutions

Viscosity is the resistance of a fluid to flowing which is deformed by either shear stress or tensile stress. For a viscous flow, the viscosity **η** is coming from applied shear stress **τ** and the change in the velocity **du** with the distance **dy** imposed by two parallel plates, or

$$\eta\eta = \frac{\tau}{du/dy} \qquad \text{Eq. [2.24]}$$

Viscosity unit is described as poises (P) and pascal-seconds (Pa-s); and 1 P equals to 1 dyne-s/sm^2 , 1 Pa-s equals to 1 N-s/m^2. The correlation between poises (P) and pascal-seconds can be given as 10 P = 1 Pa-s.

The straight, parallel and uniform flow is expected from the solutions, so the shear stress, **τ**, between layers is directly proportional to the velocity gradient, du/dy**,** thus the relative motion of the layer is,

$$\tau = \mu\frac{\partial u}{\partial y} \qquad \text{Eq. [2.25]}$$

where μ is named as the coefficient of viscosity, the viscosity, or the dynamic viscosity. This equation was derived from Newton. A flow with a constant and non-constant gradient is seen in Figure 2.17.

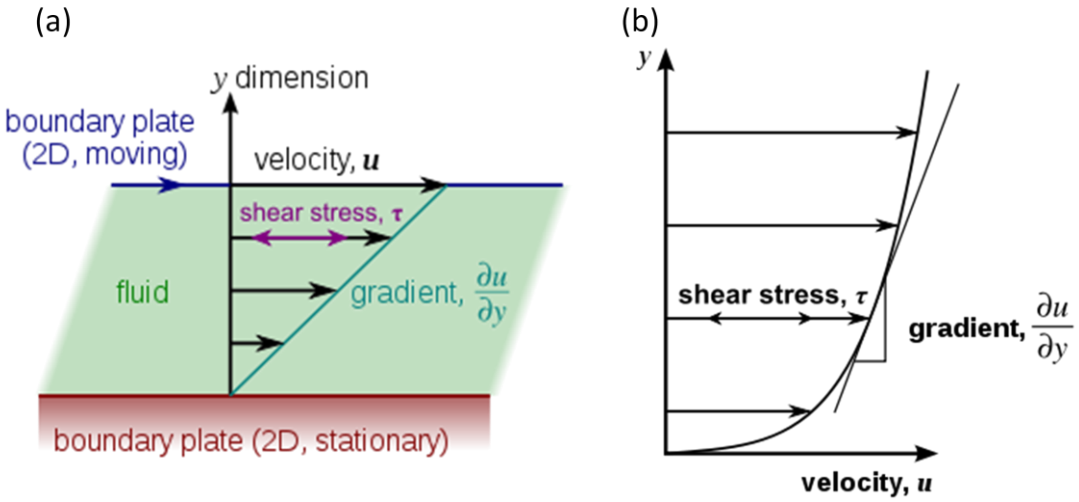

Figure 2.17 Laminar flow, (a) with a constant gradient, and (b) with a non-constant gradient [91].

There are several viscosity types and mostly seen ones are Newtonian, shear thickening and shear thinning. Types of viscosities are illustrated in Figure 2.18 [98]. The Newtonian fluids exhibit a linear behavior with the increase of shear rate. When the viscosity decreases with increasing shear rate, it is called the fluid shear-thinning. In opposite case where the viscosity increases as fluid is subjected to a higher shear rate, fluid is called as shear-thickening [92].

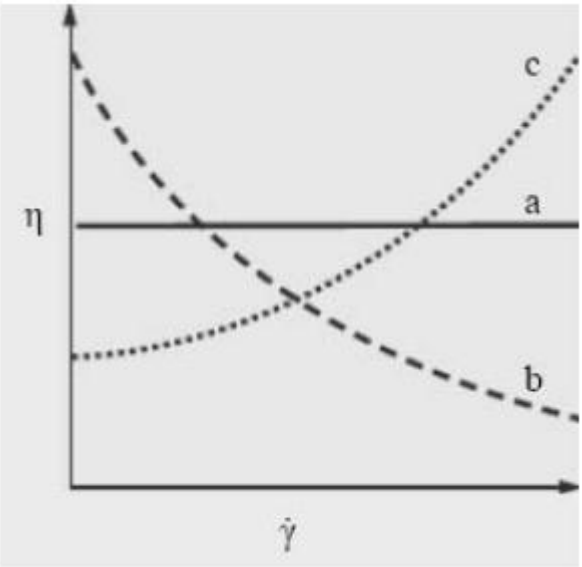

Figure 2.18 (a) Newtonian (b) shear thinning and (c) shear thickening situations for a fluid [92].

A power-law fluid is a type of generalized Newtonian fluid for which the shear stress, τ, is given by,

$$\tau = K(\frac{\partial u}{\partial y})^n \qquad \text{Eq. [2.26]}$$

where K is the flow consistency, ∂u/∂y is the shear rate, and n is the flow behavior index. n is equal to 1 corresponding to Newtonian solution.

$$\mu_{eff} = K(\frac{\partial u}{\partial y})^{n-1} \qquad \text{Eq. [2.27]}$$

The effective viscosity as a function of shear rate can be found using Eq. 2.26 as given in Eq. 2.27.

CHAPTER 3

EXPERIMENTAL PROCEDURE

In the current study, the lead-free BZT-BCT thin films were produced towards a nominal composition of $Ba(Ti_{0.8}Zr_{0.2})O_3$-$(Ba_{0.7}Ca_{0.3})TiO_3$ to obtain coexistence of rhombohedral and tetragonal phases at room temperature through morphotropic phase boundary (MPB). Solution preparation, coating and annealing stages were performed, respectively, to obtain optimum electrical properties.

3.1 Solution Preparation

3.1.1 Starting Materials

To achieve true composition of the BZT-BCT film, the precursor solution was prepared using predetermined amounts of barium acetate $Ba(CH_3COO)_2$ (Aldrich Co., purity 99+%), calcium acetate hydrate $Ca(CH_3COO_2).H_2O$ (Merck Co., purity 97+%), zirconium (IV) isopropoxide $Zr(OC_3H_7)_4$ (Aldrich Co., 70wt.% solution in 1-propanol) and titanium *n*-propoxide $Ti(OC_4H_9)_4$ (Aldrich Co., 97+%) as starting materials. 2-methoxyethanol $C_3H_8O_2$ (Aldrich Co., purity 99%) and glacial acetic acid $C_2H_4O_2$ (Merck Co., purity 99.8+%) were used as solvents for metal alkoxides (zirconium (IV) isopropoxide, titanium *n*-propoxide) and metal carboxylates (barium acetate, calcium acetate hydrate), respectively.

3.1.2 Solution Preparation

To produce homogeneous films in desired composition, preparation of the precursor is extremely important. Starting materials are divided in two groups as metal alkoxides (zirconium (IV) isopropoxide, titanium *n*-propoxide) and metal

carboxylates (barium acetate, calcium acetate hydrate). Therefore the solvents for these materials are different. 2-methoxyethanol and acetic acid were used as solvents for metal alkoxides and metal carboxylates, respectively. In the first solution, to prepare metal carboxylate complex, barium acetate, calcium acetate hydrate and acetic acid were mixed in predetermined ratios at high temperature. The mixing of materials with solvent at high temperature is crucially important to prevent from precipitation. The temperature used for this stage was 125 ˚C for 1 h using an oil bath for homogeneous heating. A reflux system was needed for high temperature heating to avoid evaporation which results in the change of the molarity of solution. Simultaneously, the second solution was prepared using zirconium (IV) isopropoxide, titanium *n*-propoxide and 2-methoxyethanol through mixing with each other at room temperature for 1 h. Subsequently, two solutions were combined together and mixed at 75 ˚C for 2 h. To obtain a stable stock solution, the next step was aging of the solution. Then, the solution was stirred at room temperature for 24 h to obtain final stock solution. The final solution can be kept as stock at least 1 week and has to be kept in an ultrasonic bath for 20 min for homogenization before each usage.

The flow chart of the production of BZT-BCT film is shown in Figure 3.1. To fabricate BZT-BCT film in desired composition and thickness, amounts of the starting materials used and solvents have to be calculated carefully. The molarity and volume of the solution was 0.845 M and 0.04 lt., respectively. So, the total mole number of the starting materials in the solution was 0.0338 moles. At first, 3.6043 gr barium acetate and 0.4410 gr calcium acetate hydrate were mixed with 10 ml acetic acid at high temperature. The solution was mixed in the reflux system for 1 h using a magnetic stirrer. At the same time, the second solution was prepared using 4.8075 gr titanium *n*-propoxide, that includes 10% excessive amount to compensate evaporation during sintering, and 0.6476 gr zirconium (IV) isopropoxide. The amount of zirconium (IV) isopropoxide was calculated 30% excess because of the fact that zirconium (IV) isopropoxide is 70 wt% in 1-propanol solution. 2-methoxyethanol used was 30 ml to obtain 40 ml (+10 ml acetic acid) precursor. This second solution was stirred at room temperature to avoid evaporation of titanium *n*-

propoxide for 1 h. The transparent solution has to be obtained to assure the

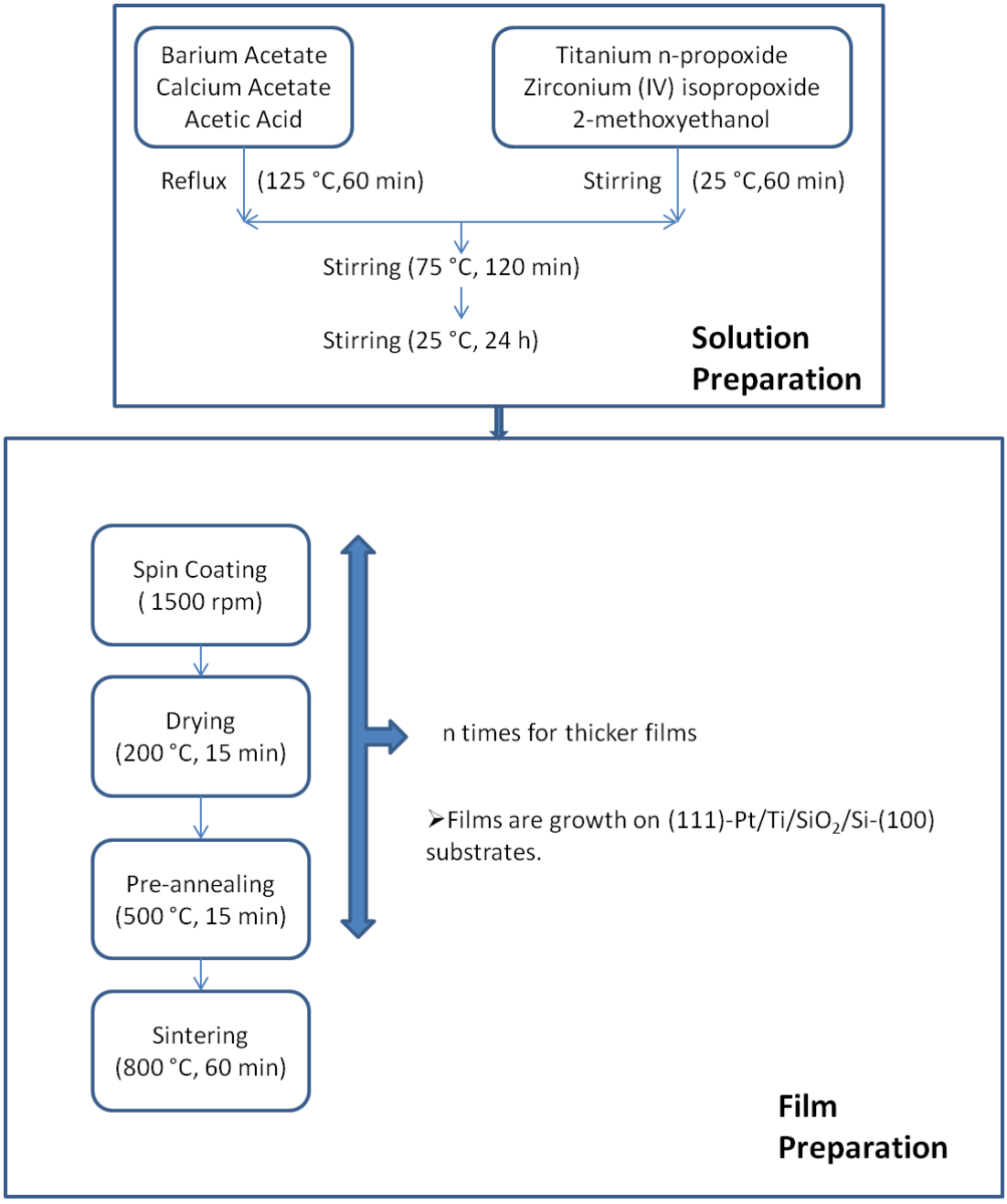

Figure 3.1 Flow chart of two different steps for the production of BZT-BCT thin films.

dissolution of all materials used. Then, both of the solutions were mixed together and stirred at 75 ˚C for 2 h. The role of this stage is to combine the two solutions to

obtain metal-oxygen-metal complex. At the end of this stage, a few milliliters acetic acid could be added to ensure molarity of the solution. The final solution was stirred 24 h at room temperature for aging stage.

3.2 Film Preparation

3.2.1 Preparation of Substrates

The selection of the substrate is a definitive factor to determine desired microstructure during a systematic study. Therefore, there are some parameters to obtain consistency between substrate and film; as thermal expansion coefficient and lattice misfit. The calculated lattice misfit between substrate and BZT-BCT film is 1.54%. The conductivity of the substrate as bottom electrode is another selection criteria for piezoelectric applications. Thus, lead-free BZT-BCT thin films were grown on (111)-Pt/Ti/SiO_2/Si-(100) (INOSTEK Korea) substrates by CSD technique in this thesis. Specifications of the substrate are shown in Table 3.1. The effective usage of the substrate is only possible by divided wafers. Consequently, the substrates were cut in square shape in dimensions of 1.5 cm to 1.5 cm. The dimensions were selected such that wafers cover completely mercury probe measurement area. The cutting procedure was done using a diamond glass cutter or green light laser (GÜNAM - Center for Solar Energy Research and Applications at METU). Usage of the laser beam has been preferred mostly to obtain minimum dirtiness on wafer surfaces. Contaminations on the surface of wafers have to be cleaned by ultrasonic alcohol procedure. Wafers were rinsed in acetone to remove organics and contaminations using the ultrasonic bath for 15 min. Then, they were rinsed in ethanol to clean the wafer surface from acetone with a second ultrasonic bath procedure. Finally the surfaces were dried using high pressure nitrogen gas.

3.2.2 Spin Coating

Before each spin coating step, it is recommended to keep the precursor in the ultrasonic bath for 20 min for homogenization. The prepared precursors were applied

to the substrates using Chemat Technology spin coating system by sticking on double sided tapes. The precursor was dropped in excess amount onto the substrates using Eppendorf pipettes. The thickness of the films depends on the viscosity of the solution and speed of the coater. Different speeds were tried using spin coater and optimum speed was determined as 1500 rpm for 30 s. To obtain desired thickness, multiple (three layers) spin coating-pyrolysis steps were performed.

Table 3.1. Specifications of multilayered substrate.

Pt Layer (Top Electrode)	
Production Method	DC Magnetron Sputtering
Thickness (nm)	150
Orientation	111
Ti Layer (Exchange Layer)	
Production Method	DC Magnetron Sputtering
Thickness (nm)	10
SiO_2 Layer	
Production Method	Thermal Oxidation
Thickness (nm)	3000
Substrate (Silicon Wafer)	
Production Method	CZ (Prime)
Thickness (μm)	525
Orientation	100

To obtain electrical properties, there is a minimum thickness where dielectric breakdown is not observed. Dielectric breakdown is the existence of a high-voltage (above 15 V for our measurements) that can find a conduction path on the film. On the other hand, increasing film thickness causes cracks due to the increse of stresses on the film surfaces and affects the microstructure by changing the orientation. Therefore, optimum films thickness was determined as 500 nm using three spin coating-pyrolysis steps.

3.2.3 Heat Treatment of BZT-BCT Thin Films

The first step on heat treatment of BZT-BCT thin films is drying process at 200 °C for 15 min. In spin coating step, most of the acetic acid and water were removed from the surface at high rpm values. Remaining chemicals, except 2-methoxyethanol, were removed in this stage. The formation of inorganic film takes place with the removal of all organics. Therefore, the second stage is pre-annealing of the films at 500 °C for 15 min. This process was repeated until desired thickness was reached.

The final step is sintering of inorganic amorphous films to form crystalline perovskite structure. Various sintering temperatures were studied to observe pure perovskite phase for 1 h sintering time. Additionally, annealing temperature is an important factor in the formation of microstructure. In this process, the heating rate of the furnace was 10 °C/min. After the process, the furnace was shut down and waited until to reach the room temperature before the specimens were taken out.

In order to understand the effect of sintering temperature, five different temperatures were selected as 700 °C, 750 °C, 800 °C, 850 °C and 900 °C. Sintering time was not changed because it does not affect the microstructure for barium titanate based phases. The selected thickness was 500 nm for three layered films that kept constant during the current study.

3.3 Characterization of BZT-BCT Thin Films

3.3.1 Structural and Morphological Analysis

Cross-sectional and morphological analyses of the films were done using FEI Nova Nano SEM 430 Field Emission Scanning Electron Microscope to find out information about the morphology and thickness of the films. Additionally, grain size of the films was studied to explain the change of the electrical properties with different sintering temperatures. To correlate the microstructural results, phase

analysis were done by X-ray diffraction using Rigaku (Japan) D/MAX 2200/PC Diffractometer between 20°-60° (2θ) with Cu (Kα) radiation. To investigate cracks on the film surfaces, Nikon Type 104 Stereo Microscope was used.

3.3.2 Dielectric and Ferroelectric Measurements

Capacitance-frequency measurements of BZT-BCT films were conducted using Agilent 4294A Impedance Analyzer for dielectric constant and tangent loss measurements. These measurements were carried out in the frequency range of 1 kHz-1000 kHz with the oscillation voltage of 0.05 V at room temperature to determine dielectric constant (ϵ_r) and tangent loss (tanδ) values. To obtain healthy electrical contacts, Mercury Probe Model 802B-200 was used for both dielectric and ferroelectric measurements. Contact area is a critical factor to define electrical field. Therefore, the contact area for this mercury probe was 0.00454 cm^2. Ferroelectric measurements were done using Radiant Ferroelectric Tester LC (Radiant Technologies, Inc.) for Polarization ($\mu C/cm^2$)-Electric field (kV/cm) curves at the voltages as 5 V, 10 V and 15 V.

3.3.3 Thermal Analysis

Differential Thermal Analysis (DTA) and Thermogravimetry analysis were done in the Central Laboratory at Middle East Technical University by Simultaneous Thermogravimetric Analyzer and Differential Thermal Analyzer to determine critical reaction temperatures and weight losses of the BZT-BCT thin films during the heat treatment stage. For this purpose, powder form of the material was prepared using the precursor that was kept at the furnace for 5 h at 100 °C. This thermal analysis gave information about drying, pyrolysis (organic removing) and annealing temperatures and reactions.

3.3.4 Viscosity Measurements

Viscosity of the solutions was found by TA Instruments ARES Rheometer unit in Central Laboratory at METU. Viscosity (Pa.s) of the solutions with increasing shear rate (s^{-1}) curves was obtained for BZT-BCT solutions in order to find the uniformity of the solutions.

CHAPTER 4

RESULTS AND DISCUSSION

The aim of the study was to produce lead-free alternative ferroelectric, piezoelectric and dielectric $Ba(Ti_{0.8}Zr_{0.2})O_3$-$(Ba_{0.7}Ca_{0.3})TiO_3$ composition using chemical solution deposition method. This composition was selected because of the fact that it is near the morphotropic phase boundary. With the help of this method, homogenous Newtonian stock solution was used to produce compositionally homogeneous, crack free and smooth thin films. To be able to find optimum film production parameters, the different sintering temperatures (700 °C, 750 °C, 800 °C, 850 °C, and 900 °C) were studied at constant sintering time (1 h) while the film thickness was kept constant. At first, the optimum film thickness was determined basically through predetermined process parameters. There was a simple conclusion about the thickness such that 2 coating layers (around 300 nm) were not enough to obtain ferroelectric and dielectric measurements because of the dielectric breakdown. Dielectric breakdown refers to the formation of electrically conducting regions in an insulating material exposed to a strong electric field [93]. This situation yields a conductive material where dielectric, ferroelectric and piezoelectric properties disappear. 4 coating layers (around 650 nm) result into cracked films because of the high stress on the films. So, 3 coating layers (around 500 nm) are the only choice at this solution molarity (0.845 M) to produce $Ba(Ti_{0.8}Zr_{0.2})O_3$-$(Ba_{0.7}Ca_{0.3})TiO_3$ composition as a measurable thin film. All the film thicknesses were determined by SEM study. By comparing thermal analysis, x-ray diffraction, ferroelectric and dielectric results for different sintering temperatures, the optimum sintering temperature was determined as 800 °C. The experimental details of the thin films that were produced during the study are seen in Table 4.1.

Table 4.1 Experimental details for the determination of the optimum lead-free thin films.

Composition	Sintering Temperature 1 h	Number of layers coated
$Ba(Ti_{0.8}Zr_{0.2})O_3$-$(Ba_{0.7}Ca_{0.3})TiO_3$	800 °C	2
$Ba(Ti_{0.8}Zr_{0.2})O_3$-$(Ba_{0.7}Ca_{0.3})TiO_3$	800 °C	3
$Ba(Ti_{0.8}Zr_{0.2})O_3$-$(Ba_{0.7}Ca_{0.3})TiO_3$	800 °C	4
$Ba(Ti_{0.8}Zr_{0.2})O_3$-$(Ba_{0.7}Ca_{0.3})TiO_3$	700 °C	3
$Ba(Ti_{0.8}Zr_{0.2})O_3$-$(Ba_{0.7}Ca_{0.3})TiO_3$	750 °C	3
$Ba(Ti_{0.8}Zr_{0.2})O_3$-$(Ba_{0.7}Ca_{0.3})TiO_3$	800 °C	3
$Ba(Ti_{0.8}Zr_{0.2})O_3$-$(Ba_{0.7}Ca_{0.3})TiO_3$	850 °C	3
$Ba(Ti_{0.8}Zr_{0.2})O_3$-$(Ba_{0.7}Ca_{0.3})TiO_3$	900 °C	3

4.1 Thermal Analysis

To find out exact process temperatures, Thermogravimetric and Differential Thermal Analysis were done on powders. The powders were prepared using homogeneous precursors that were kept at 100 °C for 5 h. Then, the analyses were examined between 25 °C to 900 °C with a heating rate of 10 °C/min. Drying, pyrolysis and sintering temperatures were determined through this thermal analysis to produce crack-free smooth films.

Exothermic and endothermic reactions in the differential thermal analysis (DTA) graph were determined to find out important stages while the BZT-BCT powders were heated up to 1000 °C. Additionally, the weight loss points during the heating were obtained with respect to thermogravimetry (TG) curves. TG and DTA curves of $Ba(Ti_{0.8}Zr_{0.2})O_3$-$(Ba_{0.7}Ca_{0.3})TiO_3$ composition are shown in Figure 4.1 and Figure 4.2, respectively. Also, both of the curves were plotted together in Figure 4.3.

Thermogravimetry (TG) curve shows us the main three weight loss regions. The first one is resulted with 11% loss and stable around 200 °C. In the spin coating process, the evaporation of solvents is not fully completed even the gel form is observed. In this region most of the solvents (acetic acid and 2-methoxyethanol) were evaporated in the gel and evaporation is completed. Second weight loss region, resulted into 25 % weight loss between 200 to 500 °C, which is due to the decomposition of acetates and organic compounds. The final weight loss region has 8% loss and occurs between 500 to 800 °C. In this region the inorganic phase was formed. Exothermic peak at 784 °C is the crystallization of perovskite phase.

Thus, the determined values for drying and pyrolysis temperatures were selected as 200 °C and 500 °C, respectively. The crystallization of perovskite phase begins with 784 °C that is seen as an exothermic peak in the DTA curve. So, the sintering temperature is probably higher than 784 °C. However, this result is not enough to determine exact sintering temperature. Therefore, a detailed crystallization study with ferroelectric and dielectric correlations will be mentioned in the next sections.

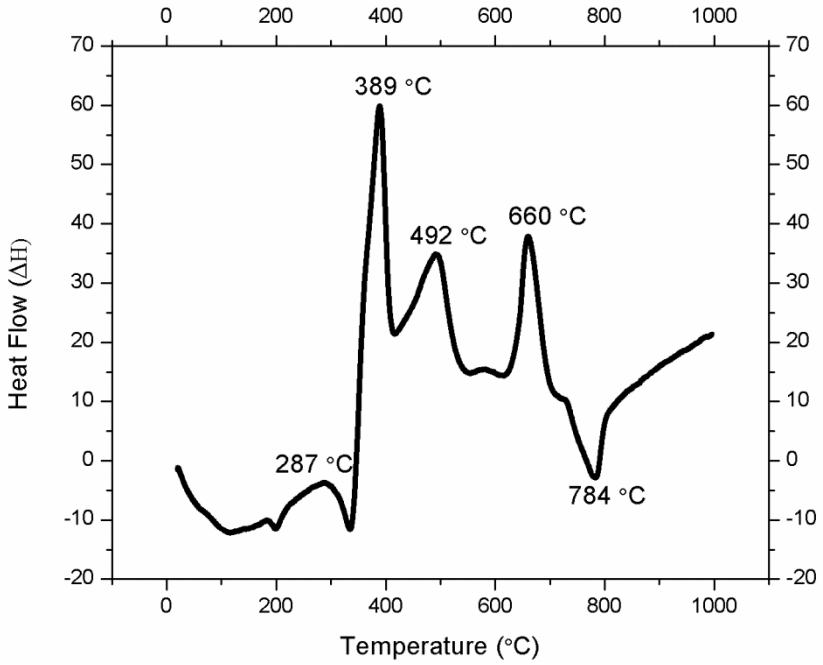

Figure 4.1 Differential Thermal Analysis (DTA) curves of $Ba(Ti_{0.8}Zr_{0.2})O_3$-$(Ba_{0.7}Ca_{0.3})TiO_3$ powders.

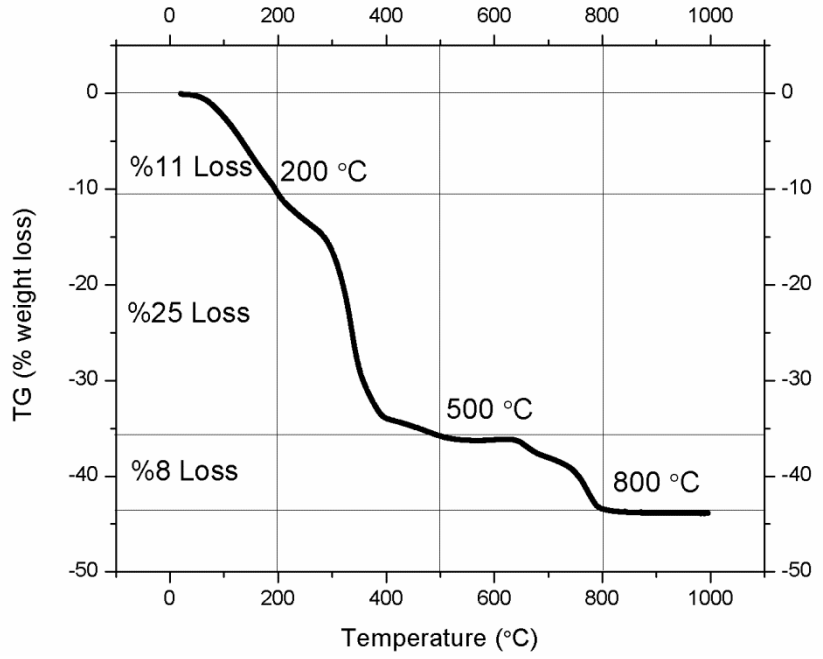

Figure 4.2 Thermogravimetry (TG) curves of $Ba(Ti_{0.8}Zr_{0.2})O_3$-$(Ba_{0.7}Ca_{0.3})TiO_3$ powders.

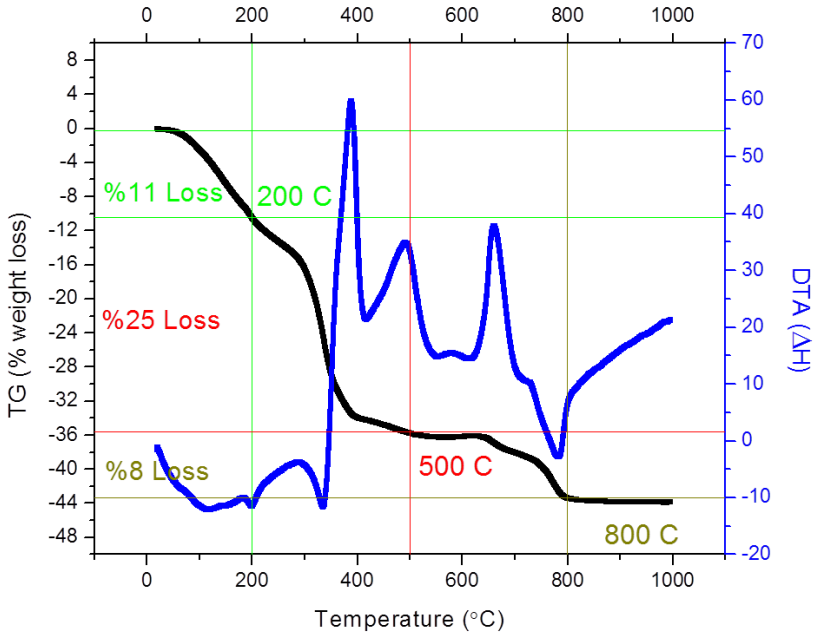

Figure 4.3 Illustration of TG and DTA curves together.

4.2 Viscosity Measurements of BZT-BCT Solutions

To understand the homogeneity of the solution, the viscosity measurements were performed. It is necessary to have a uniform solution to obtain crack-free and smooth films.

The viscosity measurement of $Ba(Ti_{0.8}Zr_{0.2})O_3$-$(Ba_{0.7}Ca_{0.3})TiO_3$ solution is given in Figure 4.4. There is a stable behavior of the solution with increasing shear rate (s^{-1}) which is a sign of uniform solution. The average viscosity is measured as 0.002154 Pa.s.

The character of the solution was estimated by calculating the power law index. It was found to be around 1 by applying Equation [2.27]. The value is close to 1 which means that the solution is Newtonian. Newtonian solutions are uniform and homogeneous solutions.

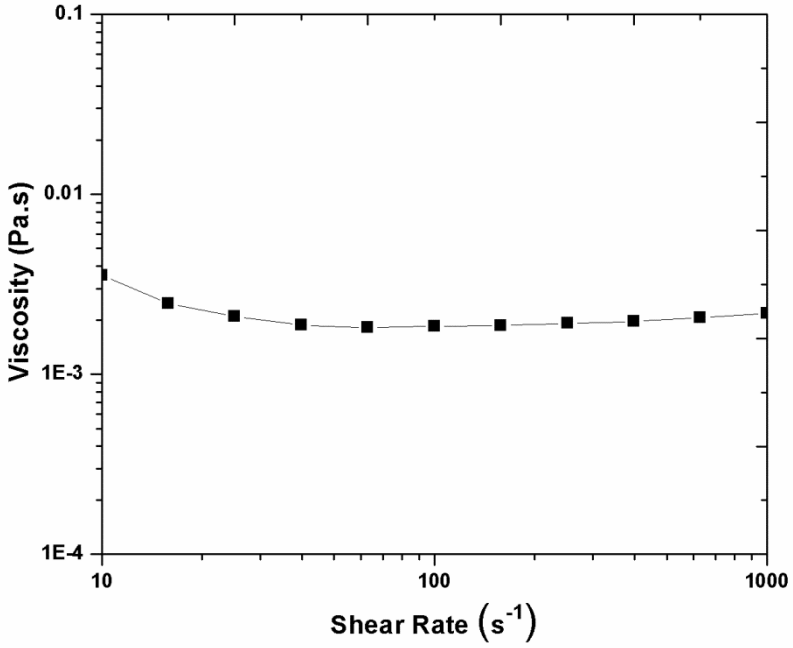

Figure 4.4 Viscosity versus shear rate of BZT-BCT solution.

4.3 Crystalline Film Formation

The phase analysis were done to determine perovskite phase using XRD studies for thin films grown on (111)-Pt/Ti/SiO_2/Si-(100) substrates. Optimum sintering temperatures were analyzed by comparing XRD spectra and the presence of pyrochlore phases was identified. Pyrolysis temperature of 500 °C and sintering temperatures of 600 °C, 700 °C, 750 °C, 800 °C, 850 °C, and 900 °C were compared. Sintering time was 1 h for all samples. The thickness of the films is kept constant as 500 nm for all of the XRD measurements.

The perovskite structure of $BaTiO_3$ has peaks approximately at 2θ = 22° (100), 33° (110), 38° (111), 46° (200), 52° (210) and 57° (211) between 20 to 60 degrees. However (111) peak could not be observed in the XRD spectra because of the overlapping of Pt (111) peak which is coming from the substrate.

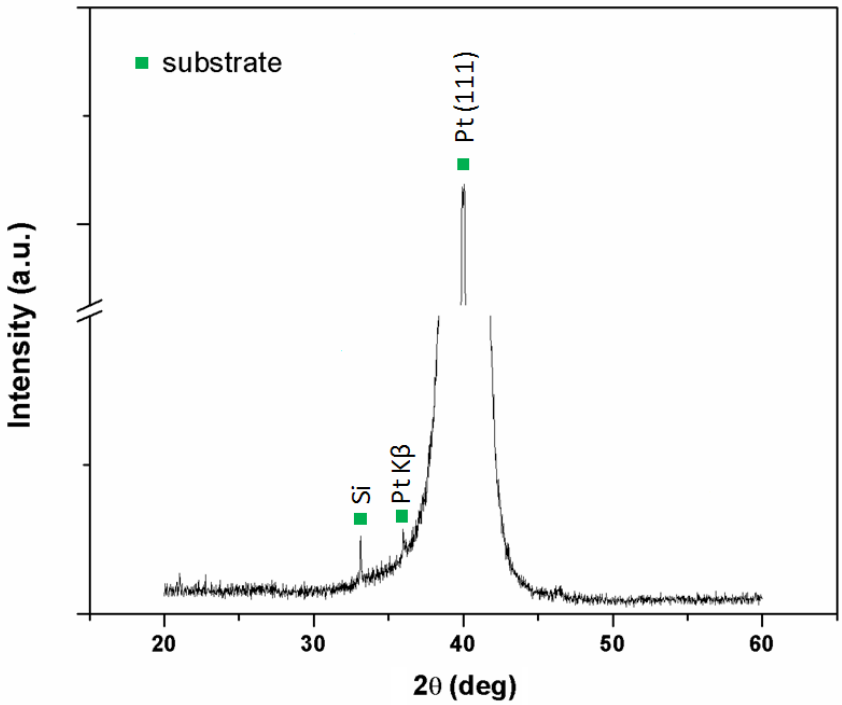

Figure 4.5 X-ray diffractogram of (111)-Pt/Ti/SiO_2/Si-(100) substrate.

Figure 4.5 shows the XRD pattern of (111)-Pt/Ti/SiO_2/Si-(100) substrate without any coating on the surface. This spectrum is important to determine the peaks which are coming from the substrate. Si peak is observed at 2θ=33.12° and determined also at the JCPDS file number of 17-0901. The main platinum peak is also appeared at 2θ=40.25° with the help of JCPDS file number of 88-2343. There is an interesting consequence here. Pt (111) peak for CuK_β diffraction was observed at 2θ=36.16°. In addition to XRD peaks of Pt (111) from CuK_α radiation, additional peaks of Pt (111) due to CuK_β radiation were observed. Normally the usage of monochromatic filter eliminates all other types of Cu radiations which are coming from the source except for CuK_α radiation. However, this situation was observed in some studies [94-96] for Pt substrates.

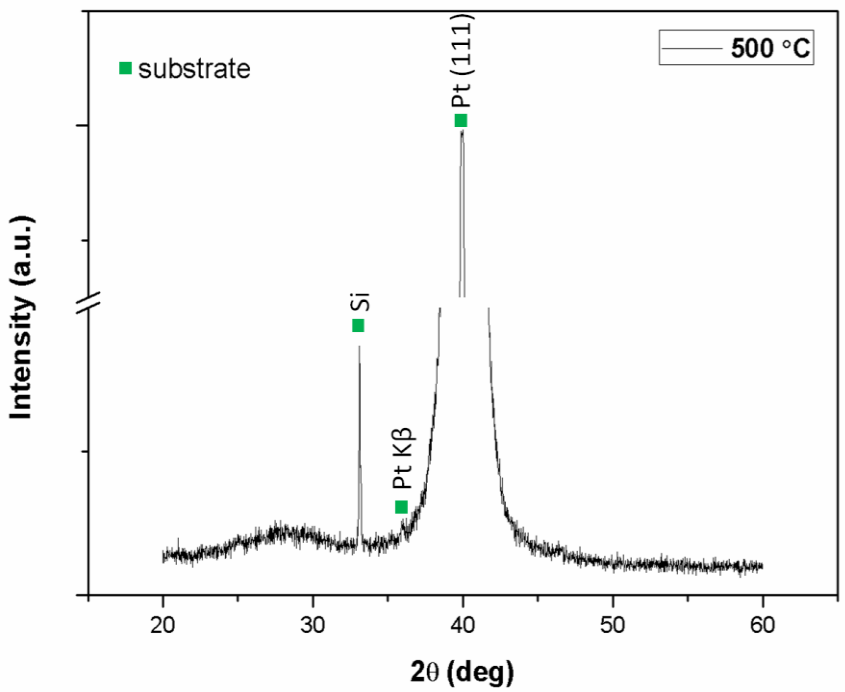

Figure 4.6 X-ray diffractogram of $Ba(Ti_{0.8}Zr_{0.2})O_3$-$(Ba_{0.7}Ca_{0.3})TiO_3$ thin film of 500 nm thickness sintered at 500 °C for 1 h.

Figure 4.6 is the x-ray diffractogram of $Ba(Ti_{0.8}Zr_{0.2})O_3$-$(Ba_{0.7}Ca_{0.3})TiO_3$ phase in the pyrolysis stage of heat treatment. There is not any crystallization at this temperature. The amorphous $Ba(Ti_{0.8}Zr_{0.2})O_3$-$(Ba_{0.7}Ca_{0.3})TiO_3$ phase exists as a coating on the substrate. So, this result gives us that 500 °C is an appropriate temperature for pyrolysis step of heat treatment because of the fact that there is no crystallization at this temperature.

Figure 4.7 illustrates the x-ray diffraction results of sintered $Ba(Ti_{0.8}Zr_{0.2})O_3$-$(Ba_{0.7}Ca_{0.3})TiO_3$ phase at 600 °C. The first perovskite peak is observed at this temperature with the existence of the first pyrochlore phase peak at $2\theta=26.9°$. This pyrochlore phase is the intermediate secondary oxycarbonate $Ba_2Ti_2O_5.CO_3$ phase prior to the formation of $BaTiO_3$. The formation of this pyrochlore phase was studied in detail by Duran et. al. [90]. The first study of metastable $Ba_2Ti_2O_5.CO_3$ phase was done by Gopalakrishnamurthy et.al. [97] that is the key for the formation of $BaTiO_3$ during the heat treatment of perovskite phase in air atmosphere. The formation of $BaTiO_3$ from the organic precursor involves three main steps during the heat

treatment: (i) drying of the solution, (ii) removal of organics and formation of intermediate phases such as $BaCO_3$, TiO_2, $BaCO_3.TiO_2$, and $Ba_2Ti_2O_5.CO_3$, (iii) decomposition of last intermediate phase that leads to the formation of $BaTiO_3$ as the final perovskite phase. According to Duran et. al. [90], the highest peak intensity of $Ba_2Ti_2O_5.CO_3$ was obtained at $2\theta=26.9°$ (100 a.u.) and only this peak is appeared at 600 °C sintering temperature that is the same with our results illustrated in Figure 4.7.

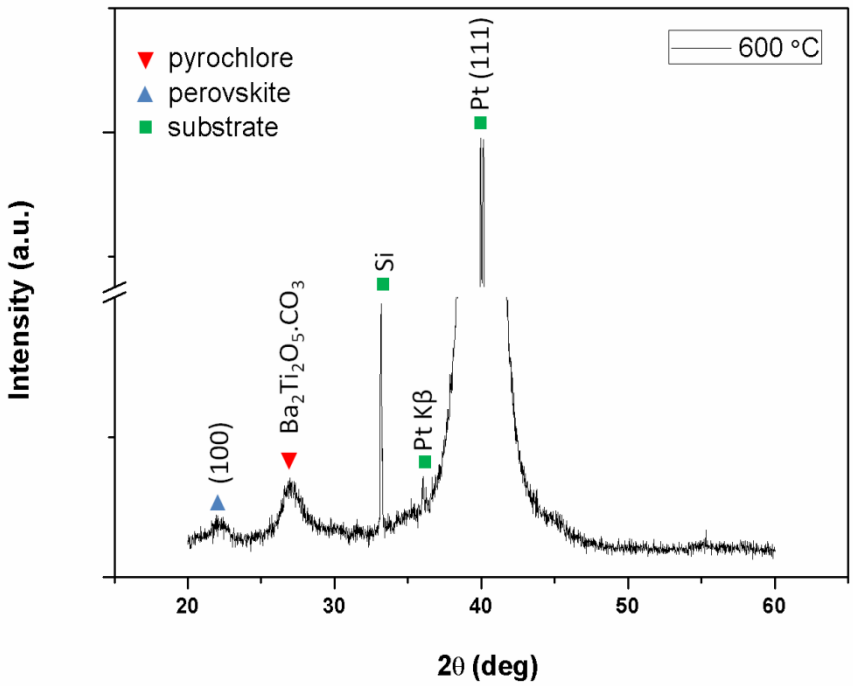

Figure 4.7 X-ray diffractogram of $Ba(Ti_{0.8}Zr_{0.2})O_3$-$(Ba_{0.7}Ca_{0.3})TiO_3$ thin film of 500 nm thickness sintered at 600 °C for 1 h.

In Duran's work [90], the pyrochlore phase disappears simultaneously and the perovskite $BaTiO_3$ phase was formed fully at 700°C. In our results, the pyrochlore phase ($Ba_2Ti_2O_5.CO_3$) did not disappear, but perovskite phase of $Ba(Ti_{0.8}Zr_{0.2})O_3$-$(Ba_{0.7}Ca_{0.3})TiO_3$ begins to form which can be followed in Figure 4.8. In Duran's work, the formation of pyrochlore and perovskite phases were investigated between 500 °C to 700 °C. However, x-ray diffraction results for $BaTiO_3$ based $Ba(Ti_{0.8}Zr_{0.2})O_3$-$(Ba_{0.7}Ca_{0.3})TiO_3$ composition in our study were investigated between 500 °C to 900 °C.

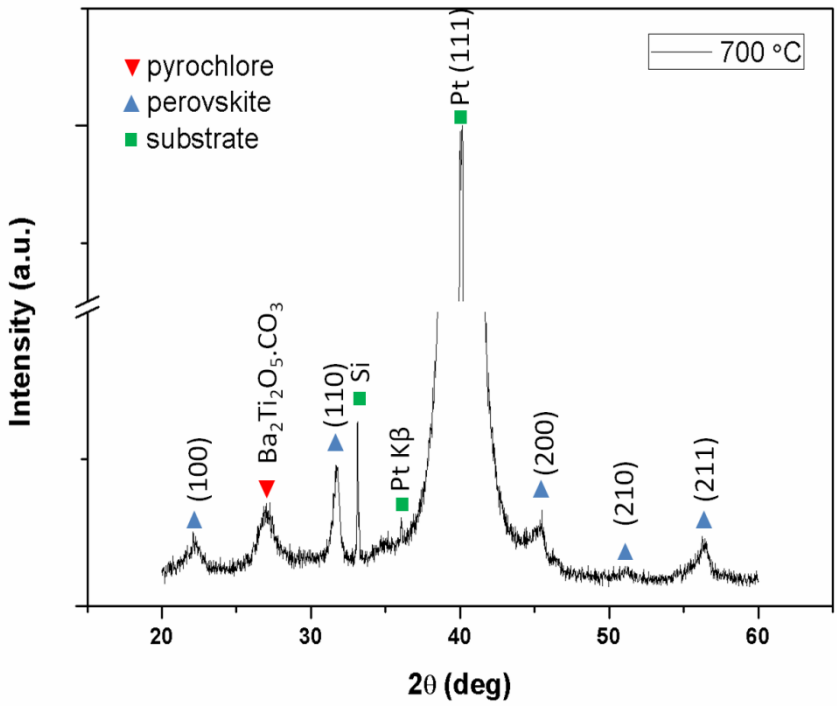

Figure 4.8 X-ray diffractogram of $Ba(Ti_{0.8}Zr_{0.2})O_3$-$(Ba_{0.7}Ca_{0.3})TiO_3$ thin film of 500 nm thickness sintered at 700 °C for 1 h.

The pure perovskite phase was only observed without secondary phases sintered at 750 ˚C, 800 ˚C, and 850 ˚C which are seen in Figures 4.9-4.11. The peak intensities of perovskite phase for these temperatures are almost the same. So, the selection of optimum sintering temperature cannot be done by just using these X-ray results. The perovskite peaks were emerged at approximately 2θ=22° (100), 31° (110), 45° (200), 51° (210) and 56° (211). Also there is (111) peak around 39°. However this peak could not be observed in X-ray results because of the overlapping with main Pt (111) peak.

The chemical solution deposition method for $BaTiO_3$ based compositions fail to display oriented growth and larger grain size for better polarization because of the homogeneous nucleation of the films during sintering stage in comparison to PZT films which have heterogeneous nucleation resulted with columnar growth of the films in desired orientation [4]. In our study this situation was totally observed. The perovskite phase has polycrystalline nature because of the homogeneous nucleation of the films.

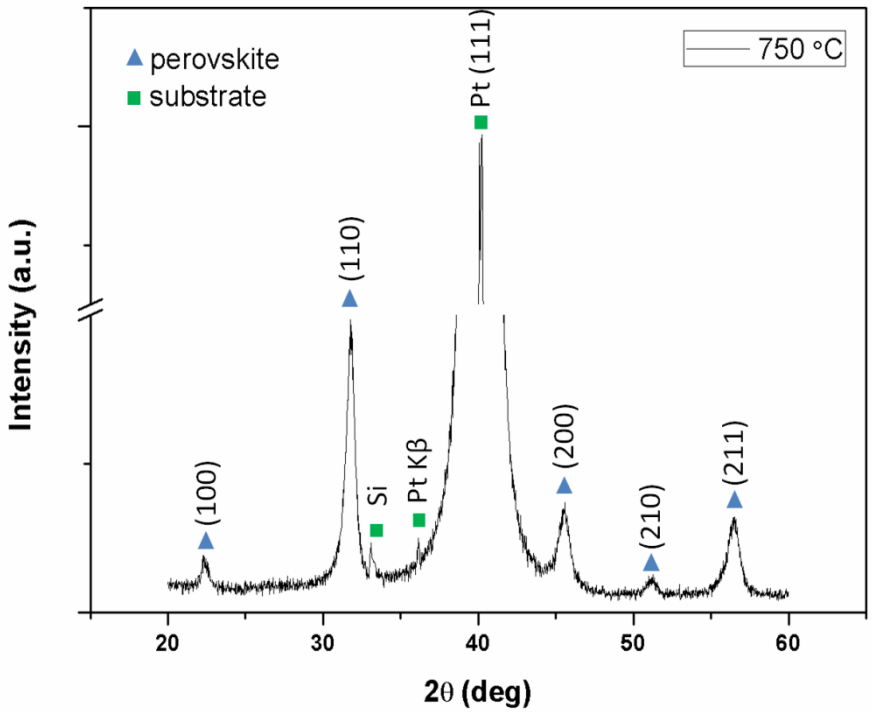

Figure 4.9 X-ray diffractogram of $Ba(Ti_{0.8}Zr_{0.2})O_3$-$(Ba_{0.7}Ca_{0.3})TiO_3$ thin film of 500 nm thickness sintered at 750 °C for 1 h.

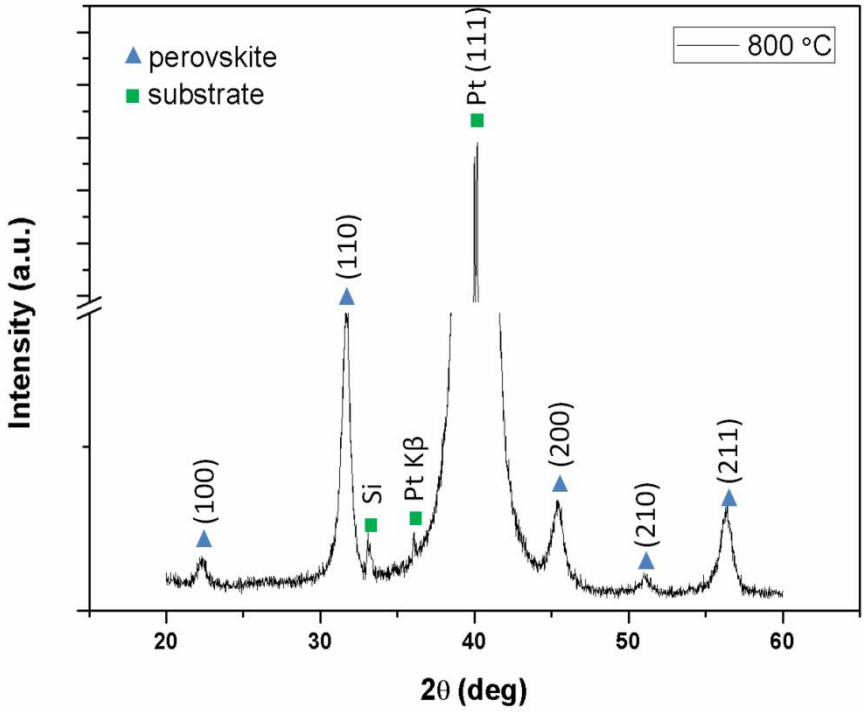

Figure 4.10 X-ray diffractogram of $Ba(Ti_{0.8}Zr_{0.2})O_3$-$(Ba_{0.7}Ca_{0.3})TiO_3$ thin film of 500 nm thickness sintered at 800 °C for 1 h.

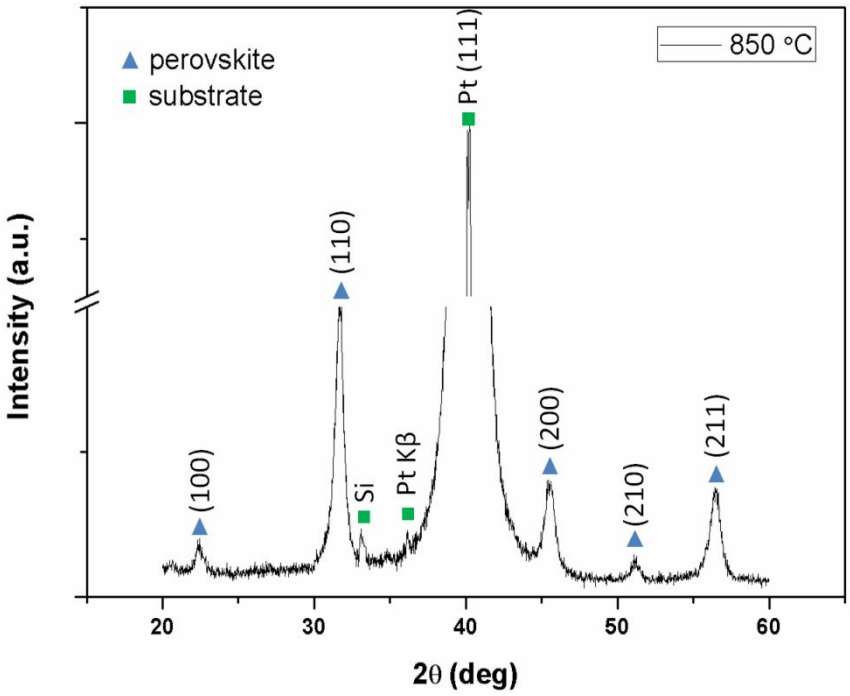

Figure 4.11 X-ray diffractogram of $Ba(Ti_{0.8}Zr_{0.2})O_3$-$(Ba_{0.7}Ca_{0.3})TiO_3$ thin film of 500 nm thickness sintered at 850 °C for 1 h.

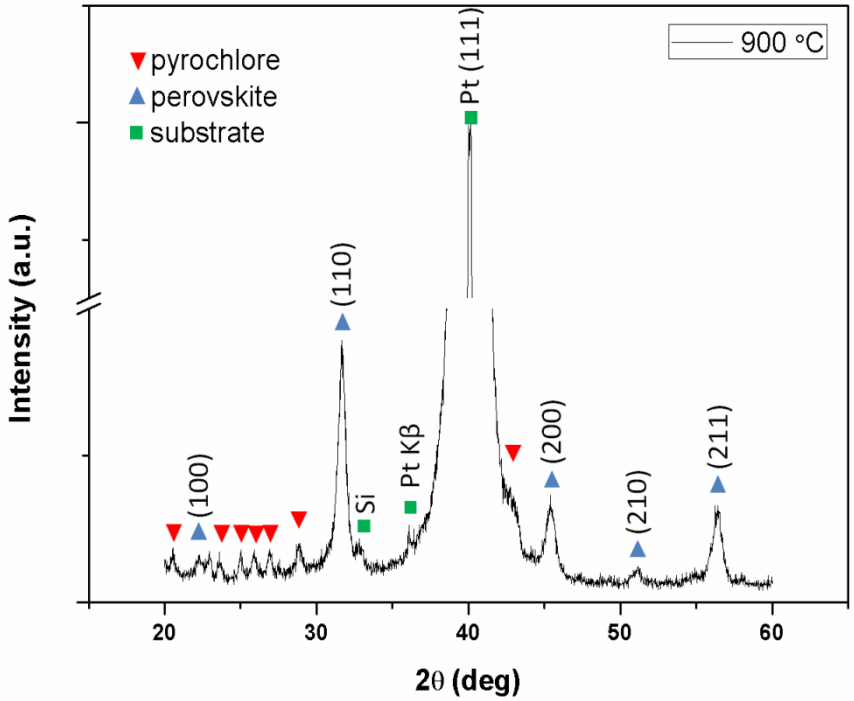

Figure 4.12 X-ray diffractogram of $Ba(Ti_{0.8}Zr_{0.2})O_3$-$(Ba_{0.7}Ca_{0.3})TiO_3$ thin film of 500 nm thickness sintered at 900 °C for 1 h.

Figure 4.12 illustrates the x-ray diffractogram of $Ba(Ti_{0.8}Zr_{0.2})O_3$-$(Ba_{0.7}Ca_{0.3})TiO_3$ thin film sintered at 900 °C. Both of perovskite and pyrochlore phases were coexisting in the system similar to sintered samples at 600 °C and 700 °C. However, in 900 °C, the other peaks of pyrochlore $Ba_2Ti_2O_5.CO_3$ and the peaks of TiO_2, TiO_2-x and $BaCO_3$ and possible other Ca and Zr derivative secondary metastable phases appeared. This situation draws a conclusion that heating the film to a temperature above the exact sintering temperature without waiting enough time at this exact temperature (the sintering temperature is lower than 900 °C in our study) causes coexistence of pyrochlore and perovskite phase in the structure. This is because of the incomplete transformation of the secondary intermediate phases to main perovskite phase at those higher temperatures. Figure 4.13 illustrates the comparison of all x-ray results for different sintering temperatures of $Ba(Ti_{0.8}Zr_{0.2})O_3$-$(Ba_{0.7}Ca_{0.3})TiO_3$ thin films. As a conclusion of this part of the study, 750 ˚C, 800 ˚C, and 850 ˚C sintering temperatures have to be compared with all ferroelectric and dielectric results to find out optimum process parameters for the first time for $Ba(Ti_{0.8}Zr_{0.2})O_3$-$(Ba_{0.7}Ca_{0.3})TiO_3$ phase using chemical solution deposition method in the literature.

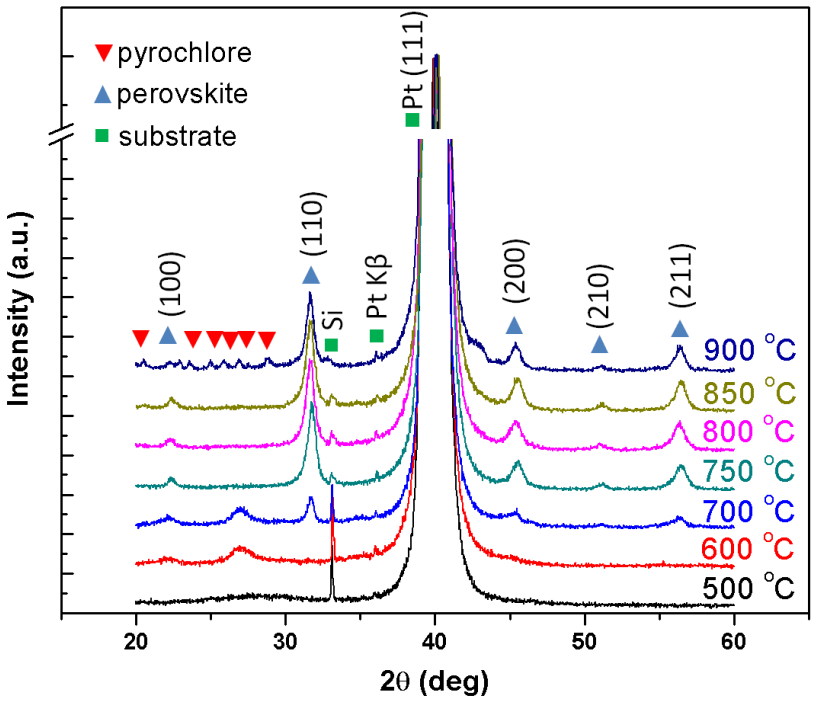

Figure 4.13 X-Ray diffraction patterns of $Ba(Ti_{0.8}Zr_{0.2})O_3$-$(Ba_{0.7}Ca_{0.3})TiO_3$ thin films sintered at different temperatures.

4.4 Morphology of BZT-BCT Thin Films

The thickness and morphology studies were investigated by using Field Emission Scanning Electron Microscope (FESEM). At first the crack involvement of the films were examined using lower magnifications in FESEM. The stresses depend on microstructure or thermal process can cause the crack initiation on the surface of the films. Figure 4.14 shows the surfaces of the films and it is clear that there are no cracks on surfaces at 5000X magnification. Also, Figure 4.15 shows that films are crack-free and have smooth surface at 1000X magnification.

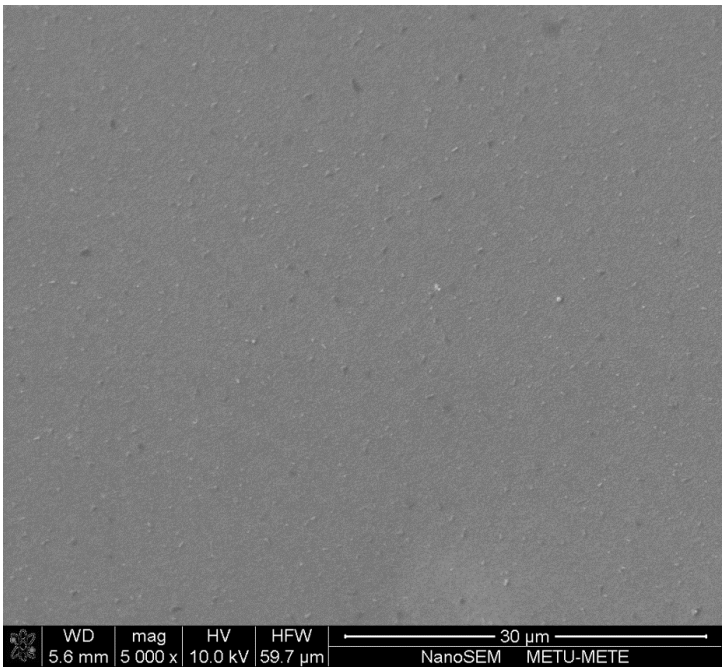

Figure 4.14 SEM image of BZT-BCT thin film surfaces sintered at 800 °C for 1 h at 5000X magnification.

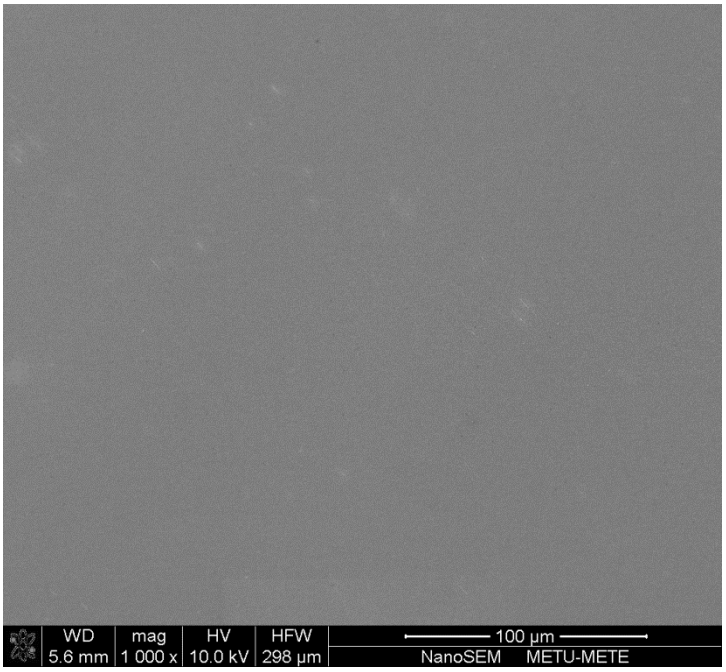

Figure 4.15 SEM image of BZT-BCT thin film surfaces sintered at 800 °C for 1 h at 1000X magnification.

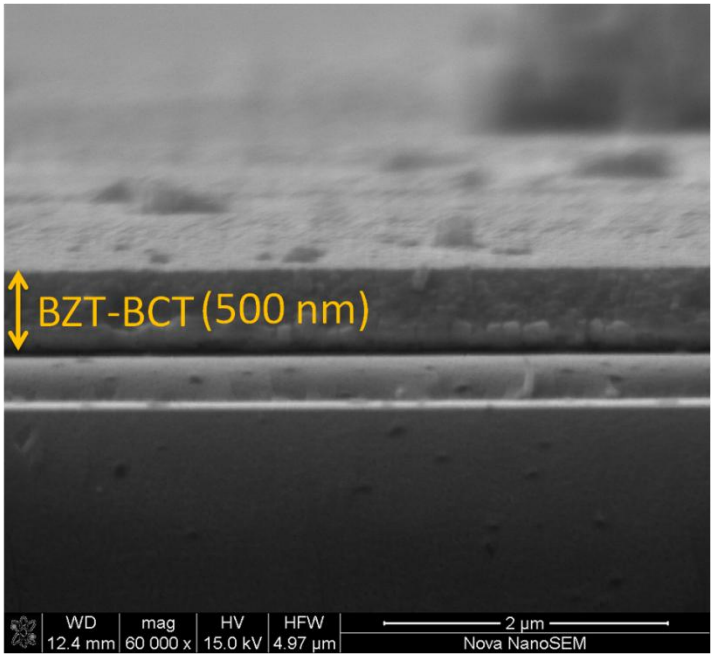

Figure 4.16 SEM cross-sectional image of 500 nm thick BZT-BCT three layered film sintered at 800 °C for 1 h.

The thickness measurements were done to examine electrical properties because of the thickness dependence of these properties by using scanning electron microscope. Figure 4.16 shows the cross-section analysis of the BZT-BCT thin film sintered at 800 °C for 1 h. In this image the thickness of the film was found as 500 nm for triple layering.

Also, another result from the cross-section analysis is that the films were sticking well to the substrate. Additionally, the effect of multiple coating layers to obtain the desired thickness was investigated using single to multilayered films can be observed in Figures 4.17 to 4.19. Thickness values were estimated approximately between 220 to 625 nm. The thickness was measured as 220 nm in single layered films produced by spin coating at a rate of 1500 rpm for 30 s. For the entire study the molarity and the spin coating conditions were held constant. 350 nm thickness films were obtained for two layered BZT-BCT thin films. Three and four layered films had a thickness of 500 and 625 nm, respectively.

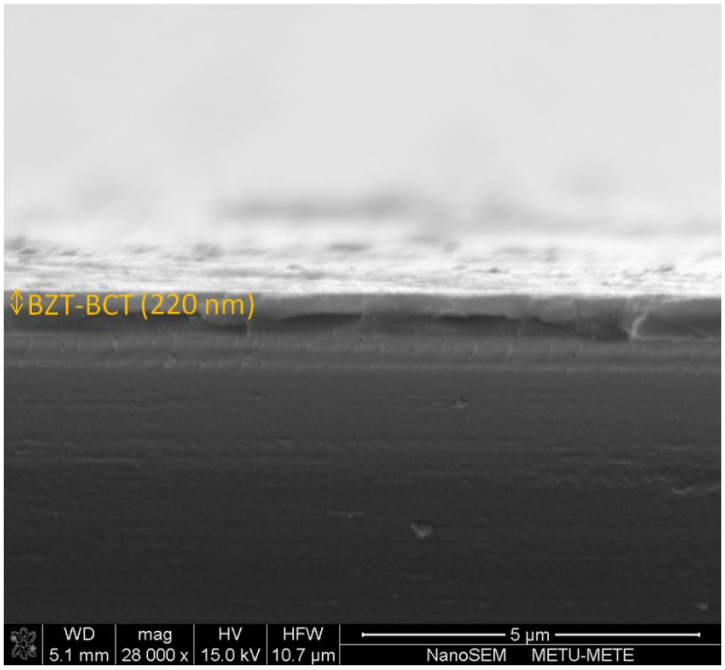

Figure 4.17 SEM cross-sectional image of single layered 220 nm thick BZT-BCT film sintered at 800 °C for 1 h.

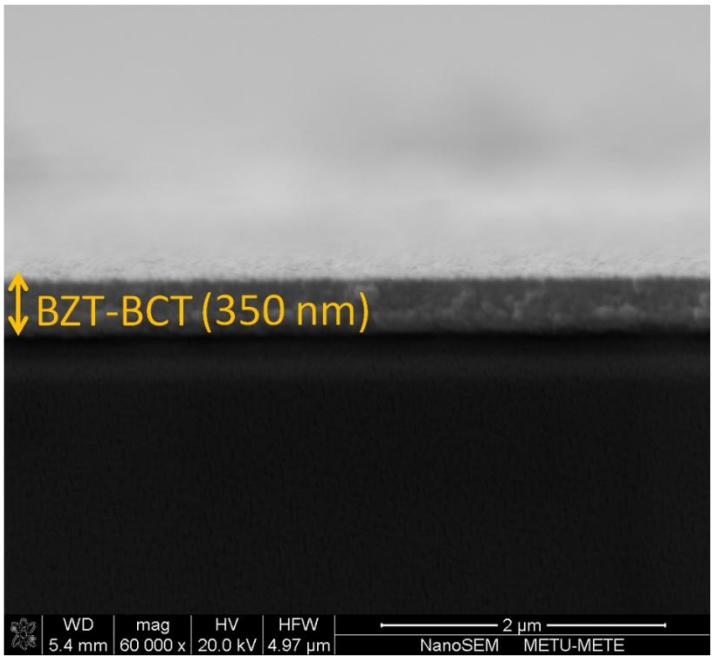

Figure 4.18 SEM cross-sectional image of double layered 350 nm thick BZT-BCT film sintered at 800 °C for 1 h.

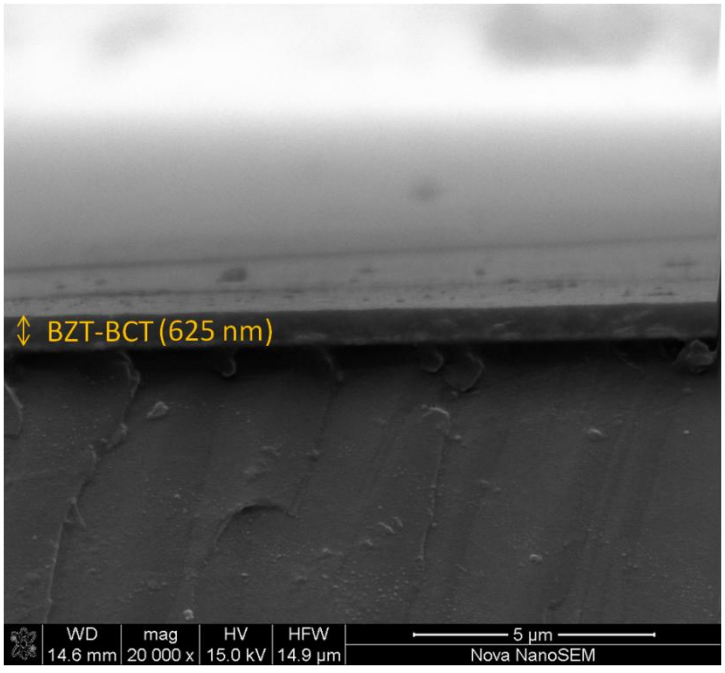

Figure 4.19 SEM cross-sectional image of four layered 625 nm thick BZT-BCT film sintered at 800 °C for 1 h.

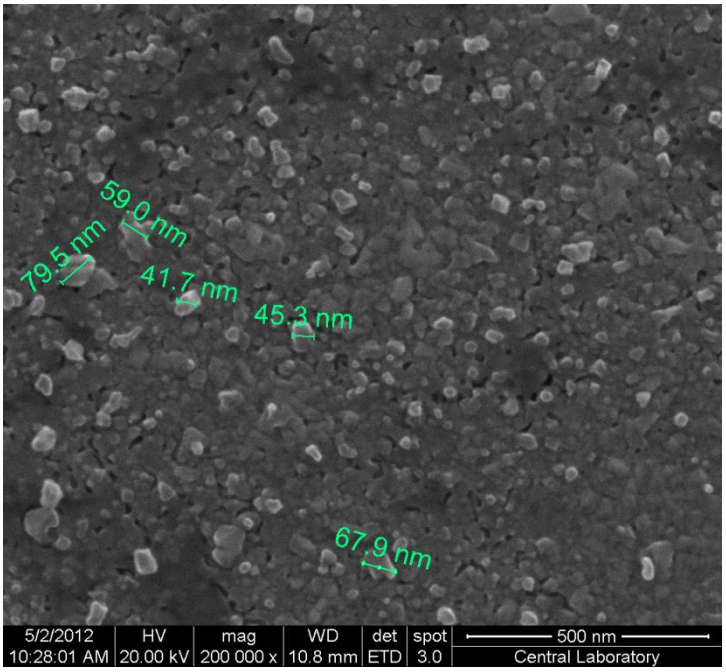

Figure 4.20 SEM image of BZT-BCT thin film surfaces sintered at 700 °C for 1 h.

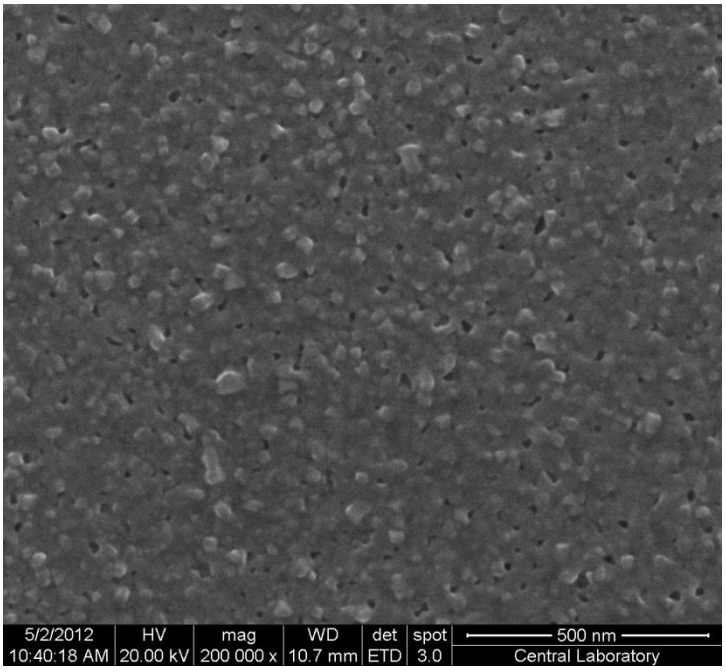

Figure 4.21 SEM image of BZT-BCT thin film surfaces sintered at 750 °C for 1 h.

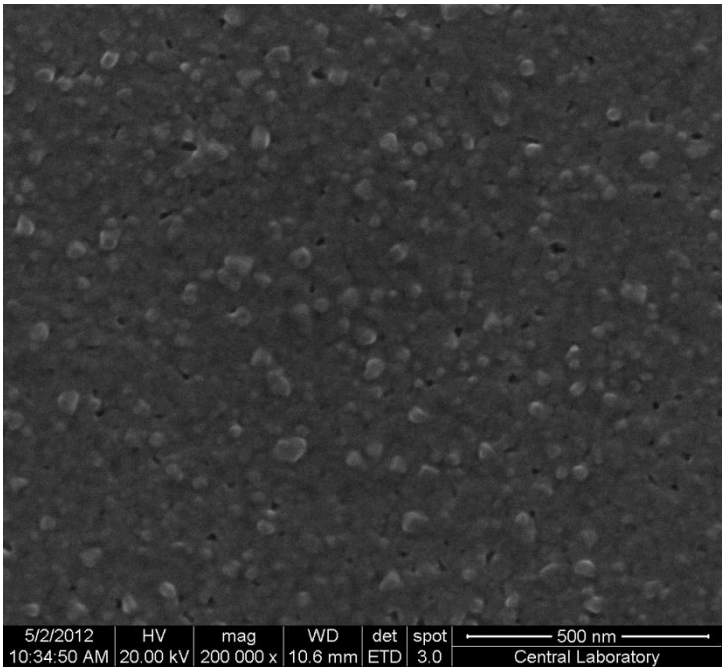

Figure 4.22 SEM image of BZT-BCT thin film surfaces sintered at 800 °C for 1 h.

Figures 4.20 to 4.25 show the surface morphologies of the BZT-BCT thin films sintered between 700 °C to 900 °C for 1 h. Sintered samples at 700 °C, 750 °C and 800 °C do not yield differences about the grain sizes. Measured grain sizes are approximately 60 nm for these samples. As a result of this situation, it can be said that sintering temperatures between 700 °C to 800 °C do not affect much the morphology and grain structure of these films.

The kinetics of phase transformation (solid to solid in our system) is quite important for chemical solution deposition based thin film growth. Most of the chemical solution deposition derived PZT thin films have columnar structure that is because the peroskite phase is nucleated at the substrate interface and growth occurs toward the surface of the film through the consumption of pyrochlore phase leading to single grain thick films [4]. Since intermediate pyrochlore phases in bulk of the PZT films can not overcome the critical sizes, which can be explained by lower driving force of crystallization (typical crystallization temperature of PZT is about 600 °C), they do not act as nucleation points within the bulk of the PZT film and crystallization results in a favoring of heterogeneous nucleation. The illustration of

this situation in a real morphological analysis is seen in Figure 4.23 from Küguler's work [106]. In contrast to the PZT thin films, in $BaTiO_3$ based compositions, perovskite phase nucleation has occurred within the bulk of the film. High crystallization temperatures of $BaTiO_3$ based compositions (typical crystallization temperature of BZT-BCT thin film is about 800 °C) lead to the overcoming of the intermediate pyrochlore phases above the critical sizes within the bulk of the film. Since crystallization starts at numerous nucleation sites throughout the film, homogeneous nucleation within the amorphous matrix and heterogeneous nucleation at the interface between substrate and film have occurred together [4]. The morphology of homogeneously nucleated $BaTiO_3$ film can be seen at Hoffmann's work [98] in Figure 4.24.

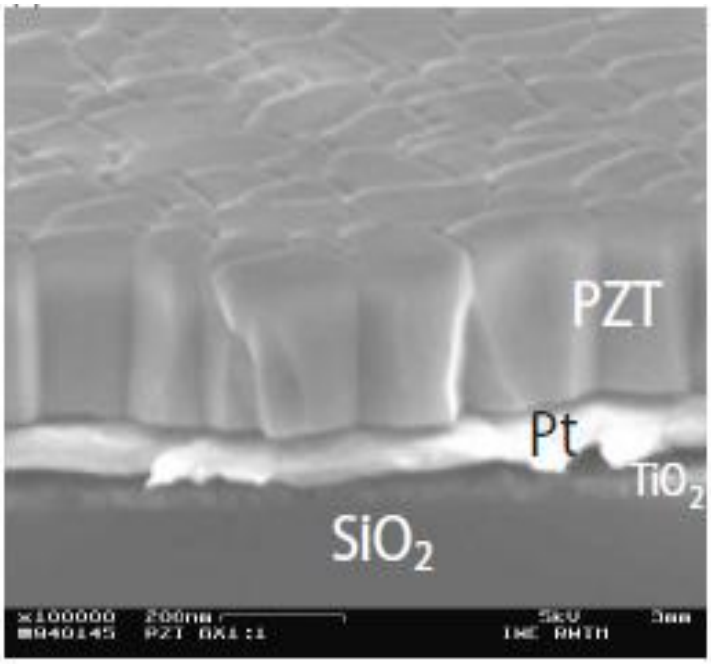

Figure 4.23 Oriented PZT phase which has dense and single grains along the thickness [99].

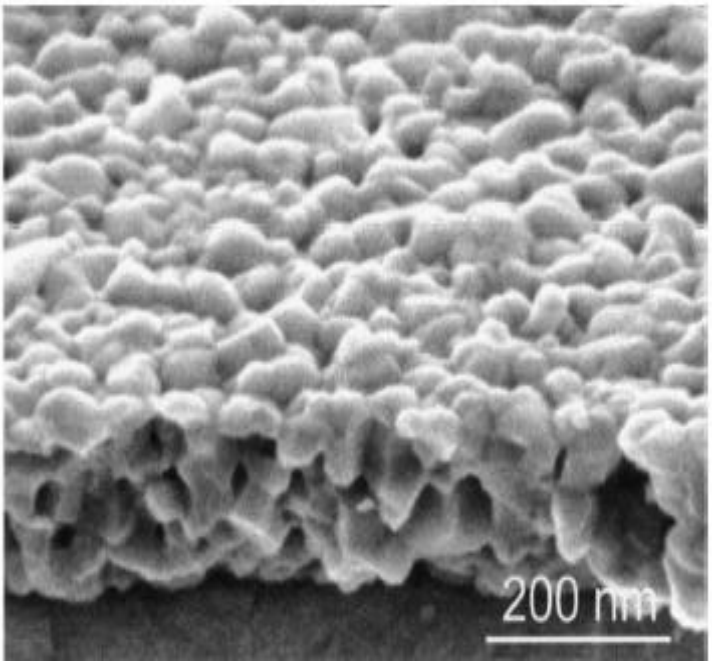

Figure 4.24 Homogeneous nucleation results with pores and small grains in whole film illustrated here in $BaTiO_3$-based films [98].

In our thin films, this theory is clearly seen because of the fact that small grains and pores exist on the surfaces. There will not be a dominant diffraction peak in XRD measurements as a result of homogeneous nucleation (causes randomly orientation) within the bulk of the film. X-ray diffraction results mentioned in the previous section reflect the polycrystalline nature of the films. There is not any dominant peak which is mostly coming from the oriented growth if it exists. In Figures 4.25, 4.26 and 4.27 for 850 °C and 900 °C sintered samples, the microstructure changed to a more porous and sharp cornered grain structure. Although there is not any intermediate phase peak in 850 °C sintered samples on XRD spectra, this temperature can be accepted as a transition temperature to the formation of some intermediate phases appearing at 900 °C. Therefore, the exact sintering temperature is below these temperatures ranges of 850-900 °C.

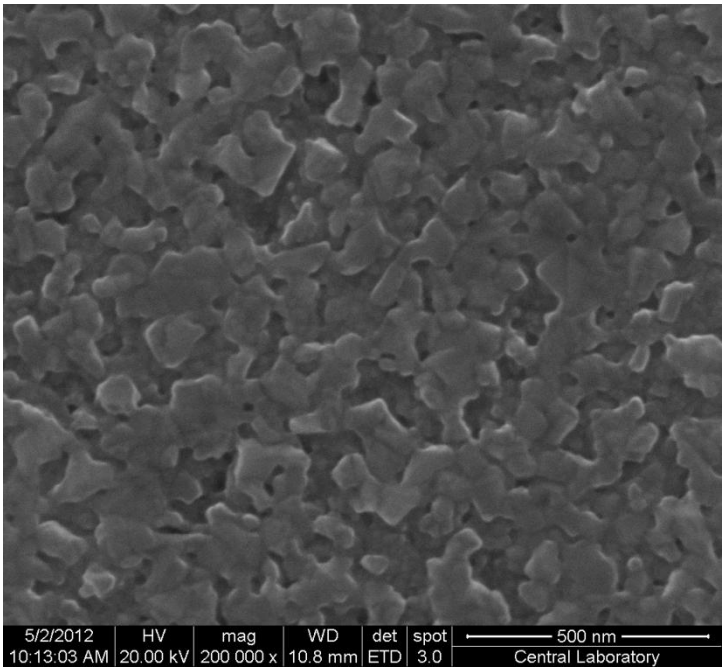

Figure 4.25 SEM image of BZT-BCT thin film surfaces sintered at 850 °C for 1 h.

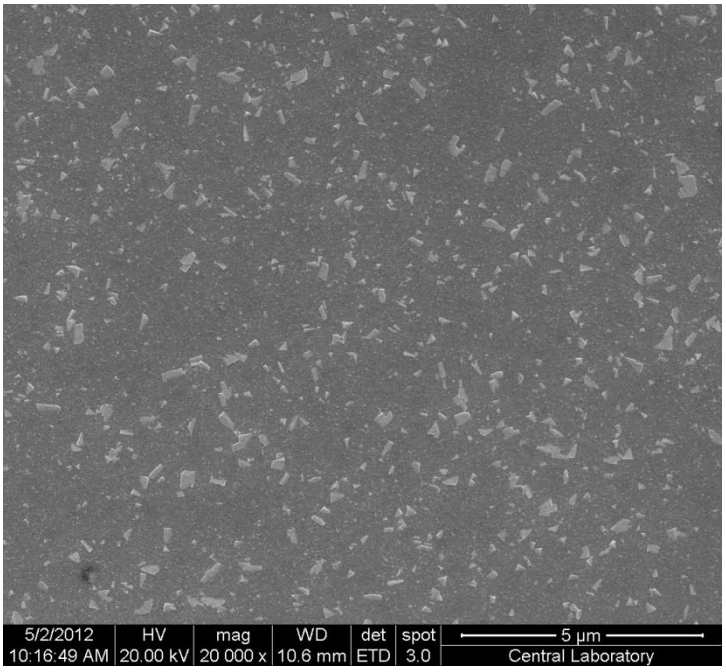

Figure 4.26 SEM image of BZT-BCT thin film surfaces sintered at 900 °C for 1 h.

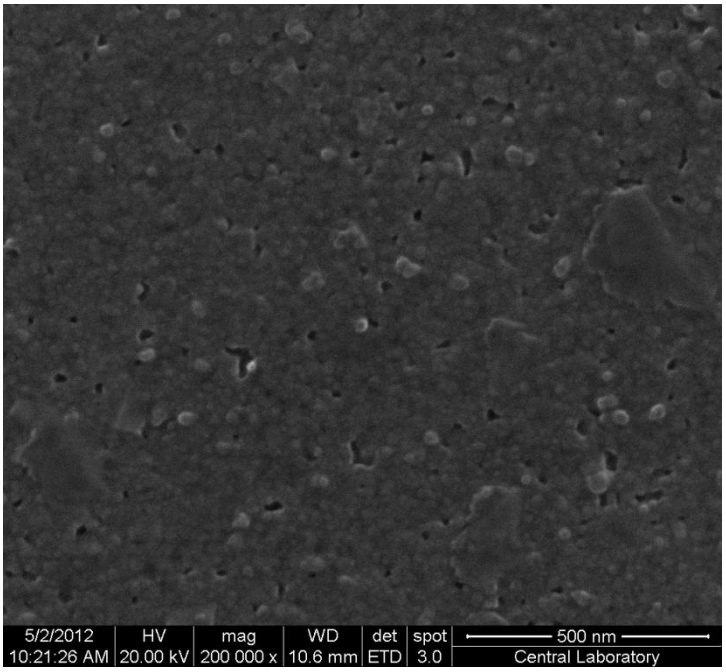

Figure 4.27 SEM image of BZT-BCT thin film surfaces sintered at 900 °C for 1 h.

4.5 Dielectric Properties of BZT-BCT Thin Films

Dielectric properties of BZT-BCT thin films were measured by Agilent 4294A impedance analyzer and a professional mercury probe contact through Capacitance-Frequency measurements. Dielectric constant (ϵ_r) and tangent loss (tanδ) values were obtained in the frequency range 1 kHz-1000 kHz with an oscillation voltage of 0.05 V in order to compare the dielectric properties of the films.

It is mentioned before that dielectric material becomes polarized in an applied electric field. The direction of the polarization will also switch in order to align with the new applied field (frequency). This cannot occur instantaneously: some time is needed for the movement of charges or rotation of dipoles. If the field is switched, there is a characteristic time that the orientational polarization (or average dipole orientation) takes to adjust, called the relaxation time. Therefore, if the electric field switches direction at a frequency higher than this characteristic frequency, the dipole orientation cannot respond to the alternating field, the polarization direction is unable

to remain aligned with the field, and this polarization mechanism ceases to contribute to the polarization of the dielectric material [100].

Therefore, a stable capacitance range has to be selected for an optimum dielectric material. For good dielectrics, the dielectric constant does not vary much from dc to microwave frequencies for most of the applications [25].

Effect of sintering temperature on dielectric constant and dielectric loss values was investigated in this part of the thesis and morphology and crystallization of thin films on dielectric properties was correlated mainly. Thickness (500 nm) was kept constant in all dielectric evaluations.

The dielectric constant can be written in terms of measured capacitance,

$$C = \frac{\epsilon_r \times \epsilon_o \times A}{d} \qquad \text{Eq. [2.5]}$$

where ϵ_r is dielectric constant of thin film, ϵ_o is the permittivity of vacuum, 8.85×10^{-12} F/m, A is the contact area (mercury probe area, 0.00454 cm^2), d is the thickness of the film.

Figure 4.28 illustrates the capacitance-frequency curves of BZT-BCT thin film sintered at 750 °C where sintering period is 1 h. Also, Figure 4.29 and 4.30 show the dielectric constant and dielectric loss curves, respectively, of BZT-BCT thin film sintered at 750 °C for 1 h. Table 4.2 is the measured capacitance, dielectric loss and calculated dielectric values for sintered samples at 750 °C for 1 h. Measured capacitance value for 600 kHz (a randomly selected frequency) is about 2.03 nF. The calculations using Equation 2.5 yields the dielectric constant as 252.5. Figure 4.31 shows all capacitance-frequency measurements for sintered samples at different temperatures. So, after this point, the capacitance measurements for all samples will not be given separately. Table 4.3 gives us all capacitance, dielectric constants and

dielectric loss values for sintered samples at different temperatures (700 °C, 750 °C, 800 °C, 850 °C, and 900 °C).

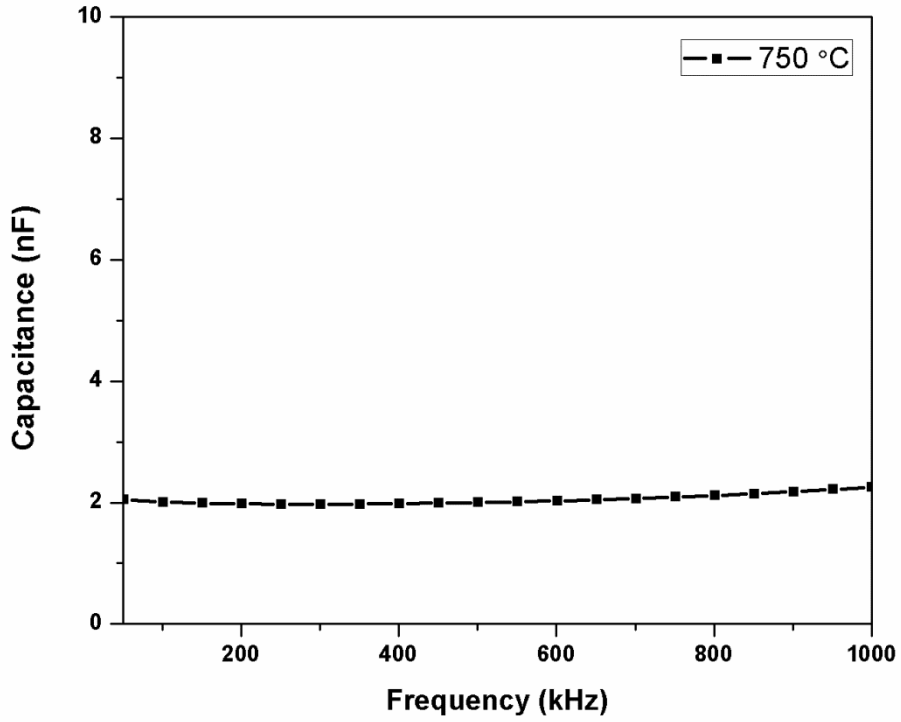

Figure 4.28 Capacitance-Frequency curves of BZT-BCT thin films sintered at 750 °C for 1 h.

Table 4.2 Measured dielectric loss, capacitance values and calculated dielectric constants as a function of frequency.

	Frequency (kHz)				
	200 kHz	400 kHz	600 kHz	800 kHz	1000 kHz
Capacitance (nF)	1.98	1.98	2.03	2.12	2.36
Dielectric Loss (%)	5.20	5.93	6.39	7.12	8.07
Dielectric Constant	246.6	246.9	252.5	263.7	281.2

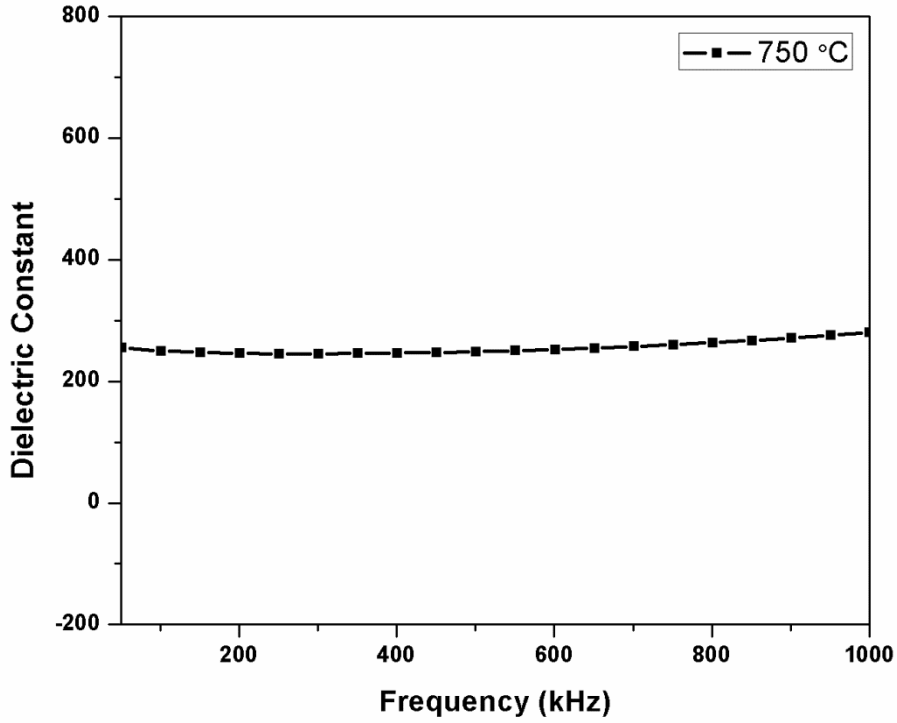

Figure 4.29 Dielectric Constant-Frequency curves of BZT-BCT thin films sintered at 750 °C for 1 h.

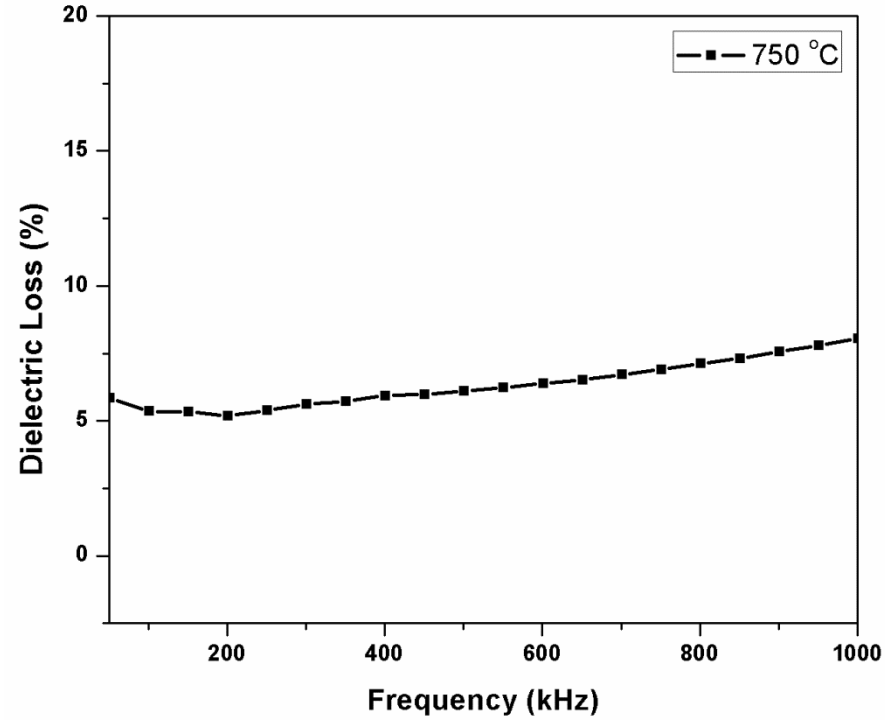

Figure 4.30 Dielectric Loss-Frequency curves of BZT-BCT thin films sintered at 750 °C for 1 h.

Table 4.3 Capacitance, dielectric loss and dielectric constants of sintered samples at different temperatures as a function of frequency.

		Frequency (kHz)				
Sintering Temperature		200 kHz	400 kHz	600 kHz	800 kHz	1000 kHz
700 °C	Capacitance (nF)	0.25	0.24	0.24	0.25	0.25
	Dielectric Loss (%)	0.14	0.79	0.87	0.95	0.97
	Dielectric Constant (K)	30.4	30.2	30.3	30.4	30.6
750 °C	Capacitance (nF)	1.98	1.98	2.03	2.12	2.36
	Dielectric Loss (%)	5.20	5.93	6.39	7.12	8.07
	Dielectric Constant (K)	246.6	246.9	252.5	263.7	281.2
800 °C	Capacitance (nF)	2.85	2.87	2.94	3.05	3.22
	Dielectric Loss (%)	3.41	3.22	3.52	4.05	4.70
	Dielectric Constant (K)	354.5	357.2	365.6	379.6	400.8
850 °C	Capacitance (nF)	1.68	1.69	1.73	1.80	1.91
	Dielectric Loss (%)	3.82	4.01	4.30	5.03	5.91
	Dielectric Constant (K)	208.8	210.0	215.4	224.5	237.9
900 °C	Capacitance (nF)	1.84	1.85	1.90	1.99	2.11
	Dielectric Loss (%)	4.53	4.44	4.71	5.19	5.98
	Dielectric Constant (K)	229.5	230.6	236.5	247.2	263.2

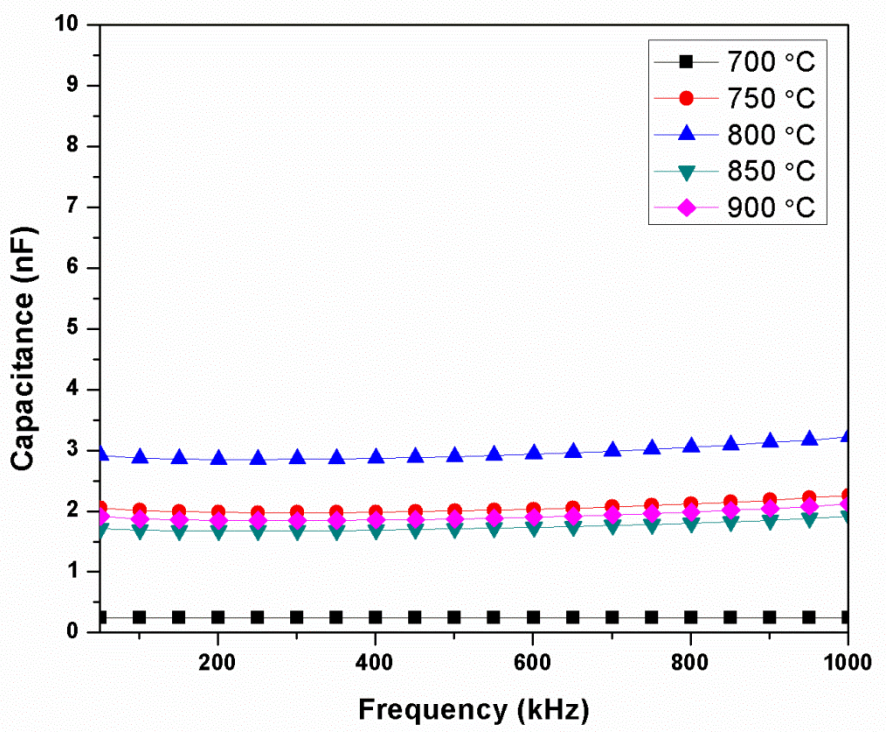

Figure 4.31 Capacitance-Frequency curves of BZT-BCT thin films sintered at different temperatures for 1 h.

Figure 4.32 to 4.36 illustrate the dielectric constant and dielectric loss values as a function of frequency for sintered samples at 700 °C, 750 °C, 800 °C, 850 °C and 900 °C, respectively.

Figure 4.32 shows much lower dielectric constant and dielectric loss values when they are compared with other samples. This is because of weak crystallization of BZT-BCT thin films and existence of pyrochlore phase which were given in XRD measurements (Fig.4.8). Especially, weak crystallization is an important factor that leads to the lower charge capacity of the material. Therefore, this low capacitance value results with low dielectric constant value. Additionally, the low dielectric loss value can be explained using this situation. If there is a weak capacitive effect (lower values of charges) on the surface, the possibility of leakage current (is the main reason of dielectric loss) will decrease. Thus, dielectric loss also will decrease as a result.

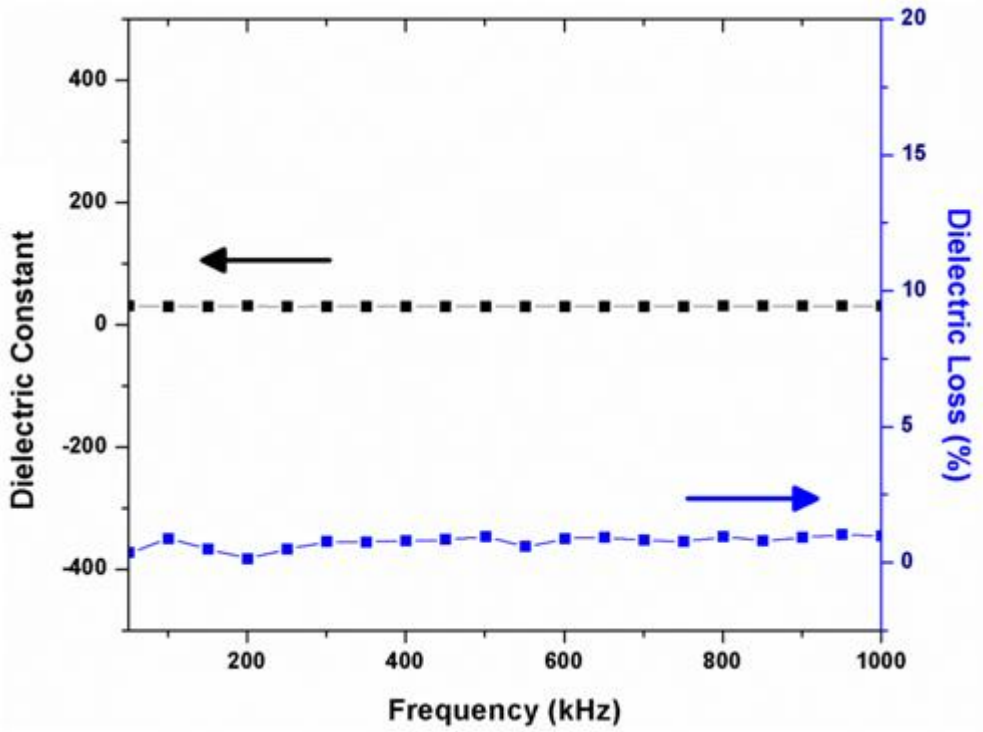

Figure 4.32 Dielectric Constant-Dielectric Loss-Frequency curves of BZT-BCT thin films sintered at 700 °C for 1 h.

It is explained in section 4.3 of this thesis that crystallization data of 750 ˚C, 800 ˚C, and 850 ˚C sintering temperatures have to be compared with all ferroelectric and dielectric results to find out optimum process parameters. The dielectric constants and dielectric loss curves of BZT-BCT thin films sintered at 750 °C and 800 °C are seen in Figure 4.33 and 4.34, respectively. As it is seen in the Table 4.3 and Figure 4.34, the highest dielectric constant (365.6 at 600 kHz) in this study was observed for BZT-BCT thin films sintered at 800 °C for 1 h. Also, the lowest dielectric loss values were obtained using this process temperature. When the morphologies were compared for samples sintered at 750 °C and 800 °C, the sintered samples at 750 °C have higher amount of surface porosity than sintered samples at 800 °C which can be a reason for lower dielectric constant for 750 °C process temperature. Secondly, as it is seen in thermal analysis results (in Figure 4.1), the maximum peak value of the crystallization temperature (784 °C) is higher than 750 °C which leads to better crystallization of the films at higher temperatures (such as 800 °C). This can explain higher dielectric constant obtained for sintered samples at 800 °C in comparison with 750 °C process temperature.

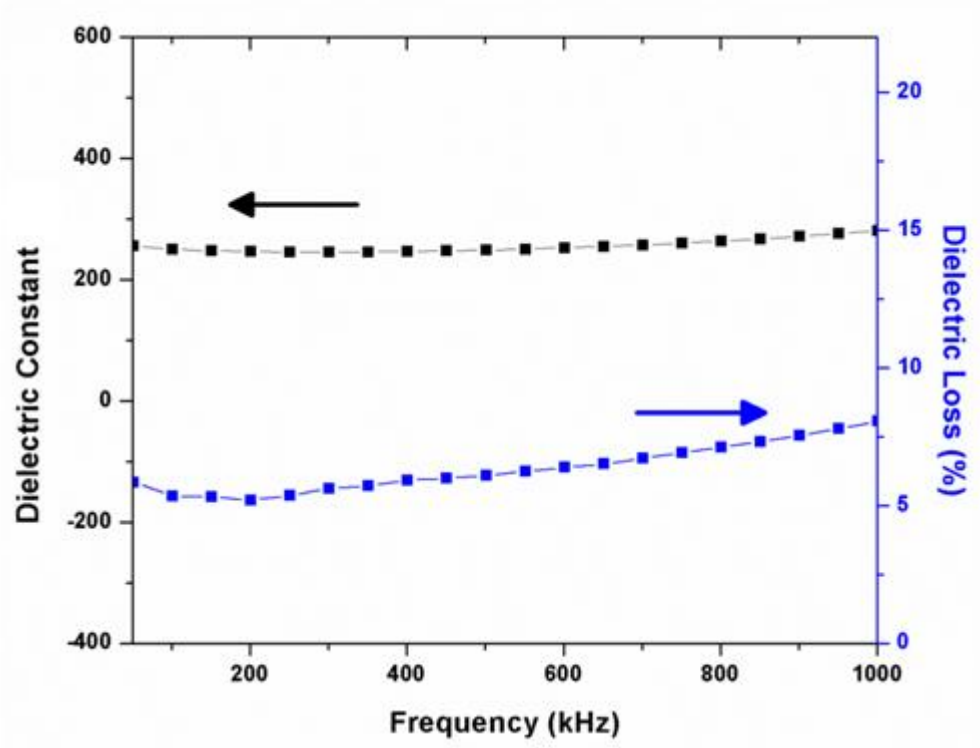

Figure 4.33 Dielectric Constant-Dielectric Loss-Frequency curves of BZT-BCT thin films sintered at 750 °C for 1 h.

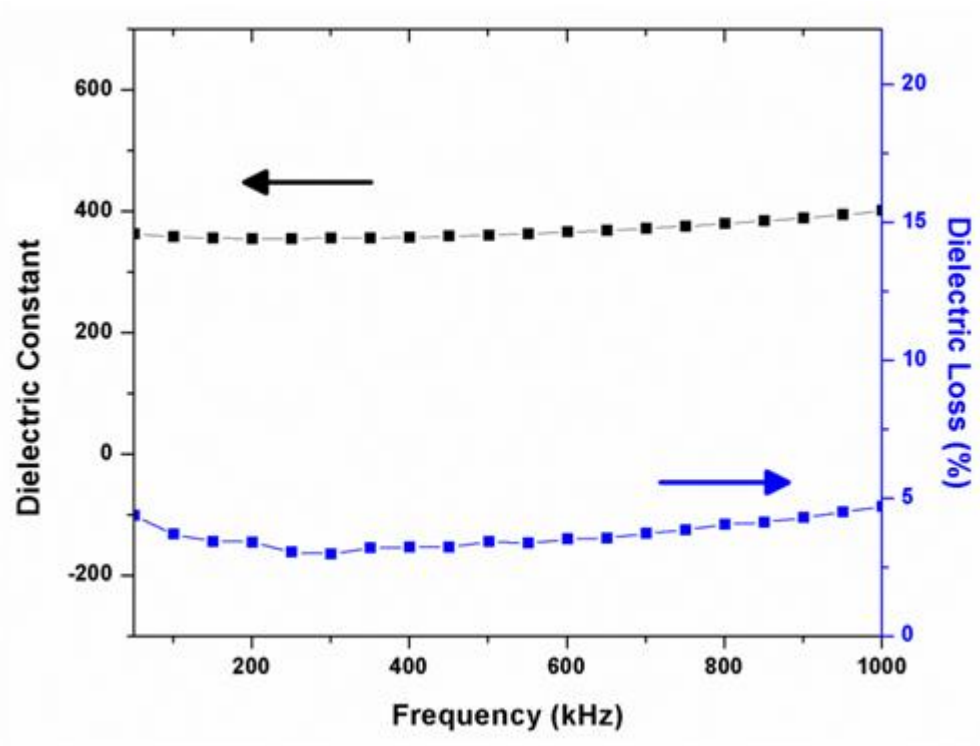

Figure 4.34 Dielectric Constant-Dielectric Loss-Frequency curves of BZT-BCT thin films sintered at 800 °C for 1 h.

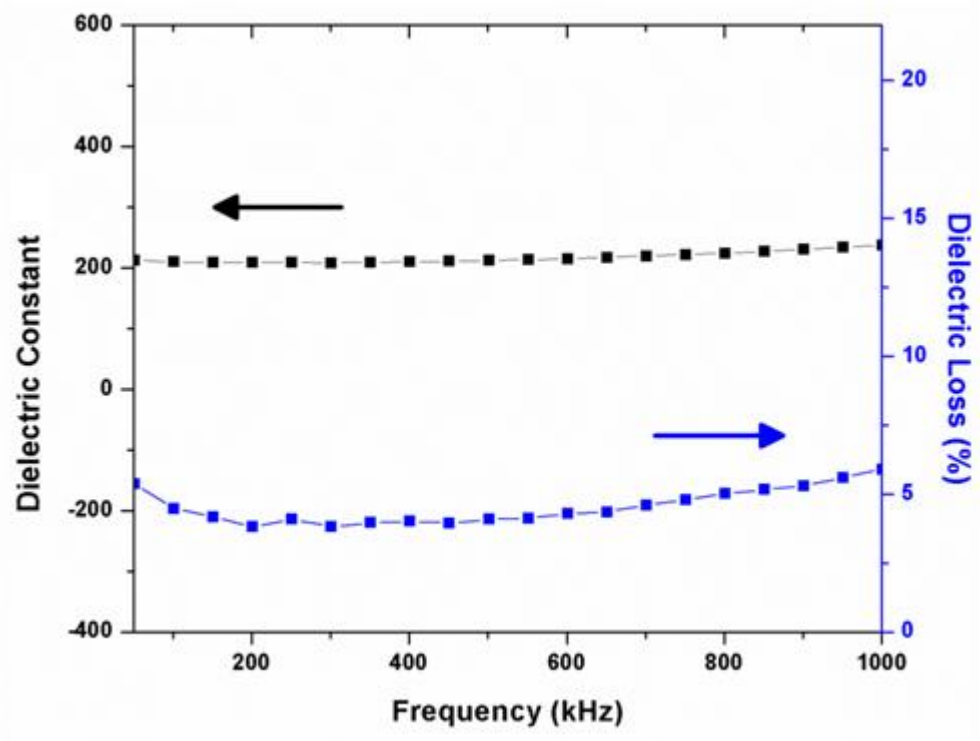

Figure 4.35 Dielectric Constant-Dielectric Loss-Frequency curves of BZT-BCT thin films sintered at 850 °C for 1 h.

Figure 4.35 shows the dielectric constant and dielectric loss curves of BZT-BCT thin films sintered at 850 °C for 1 h. In this process temperature, the dielectric constant values were decreased dramatically. Morphological results showed that (Figure 4.23) samples sintered at 850 °C have high surface porosity. Also, it is known that surface porosity is the source of moisture and this moisture causes the ionic conductivity on the surface. So, this dramatic decrease on the dielectric properties can be explained with the presence of surface porosity on thin films at this sintering temperature.

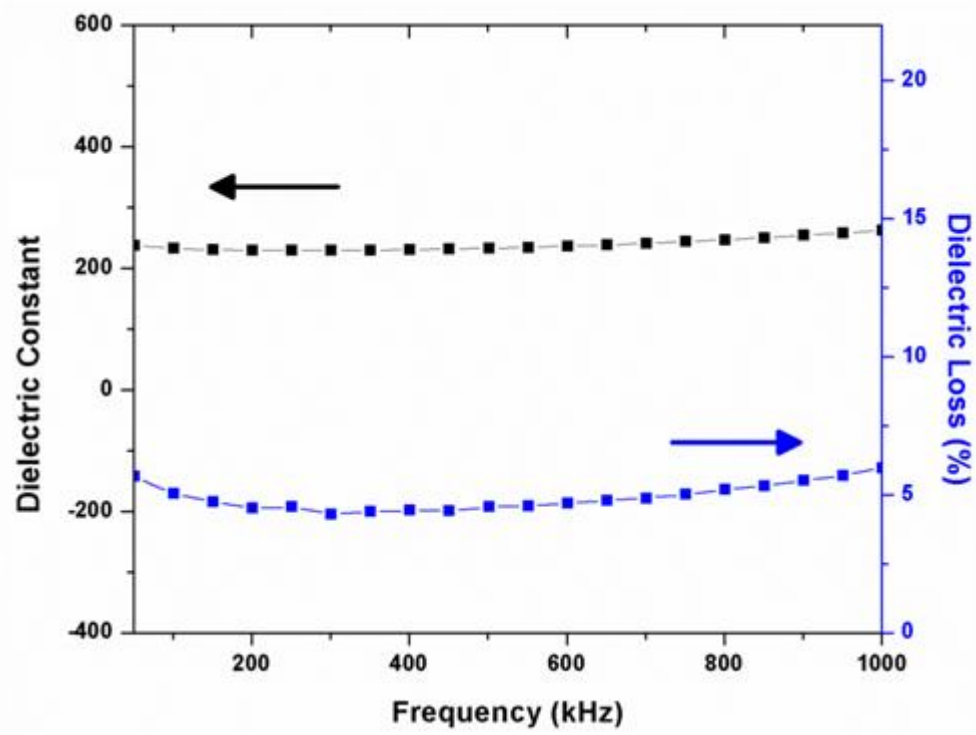

Figure 4.36 Dielectric Constant-Dielectric Loss-Frequency curves of BZT-BCT thin films sintered at 900 °C for 1 h.

Figure 4.36 illustrates the dielectric constant and dielectric loss as a function of frequency for BZT-BCT thin films sintered at 900 °C for 1 h. The presence of pyrochlore phase is a serious problem which was observed both in morphological and crystallographic analysis. As it is seen, the presence of pyrochlore phase is not as effective as the presence of moisture in comparison of dielectric properties, which was observed for films sintered at 850 °C. Therefore, the dielectric constant of the thin films sintered at 900 °C is slightly higher than the dielectric constant of films sintered at 850 °C. All comparisons of dielectric constants and dielectric losses for BZT-BCT thin films sintered at different temperatures can be examined in Figure 4.37 and 4.38, respectively.

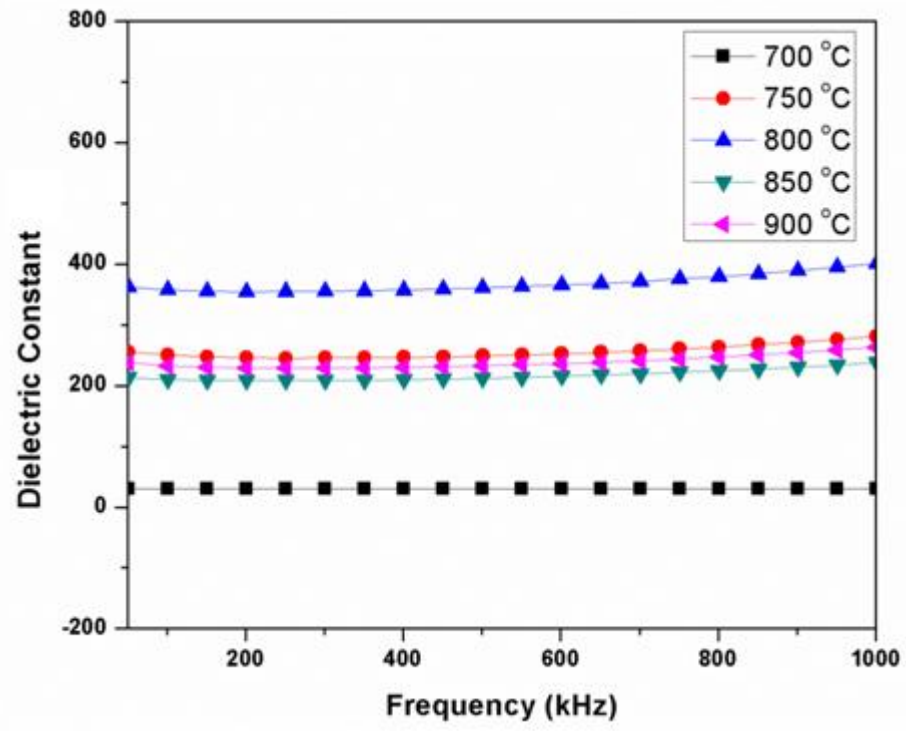

Figure 4.37 Dielectric Constant-Frequency curves of BZT-BCT thin films sintered at different temperatures for 1 h.

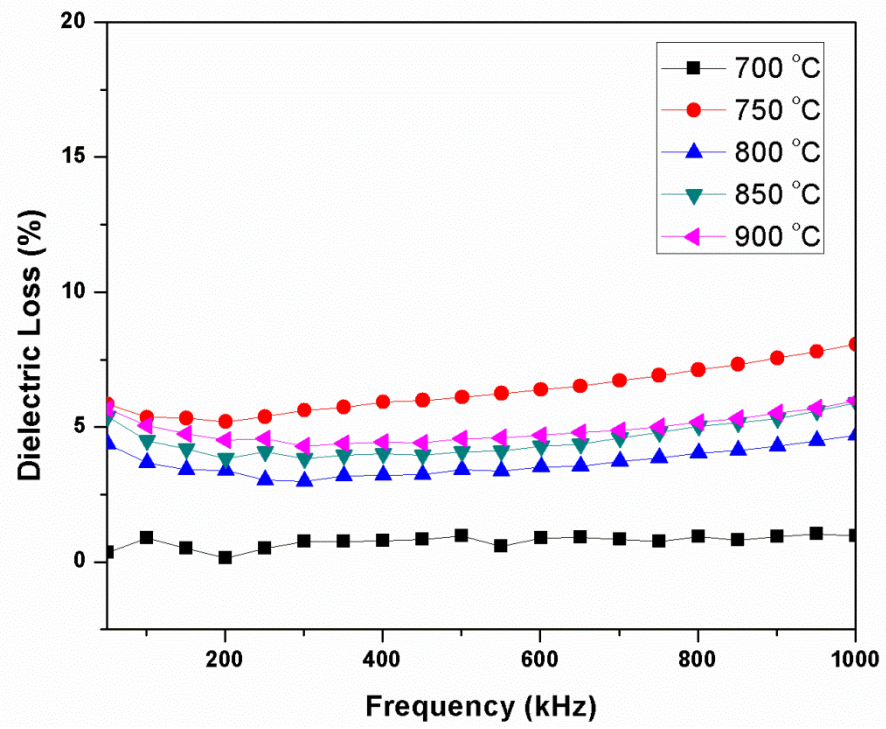

Figure 4.38 Dielectric Loss-Frequency curves of BZT-BCT thin films sintered at different temperatures for 1 h.

4.6 Ferroelectric Properties of Materials

The ferroelectric properties of BZT-BCT thin films were investigated using measurement of polarization produced by applied electric field to find out optimum sintering temperature for the films. Remnant polarization (Pr) and coercive field (Ec) values were measured. Five different sintering temperatures (700, 750, 800, 850 and 900 °C) were applied to the films. Sintering time and thickness kept constant as 1 h and 500 nm, respectively. Table 4.4 shows the results of different sintering temperatures on remnant polarization and coercive field at various applied voltages for BZT-BCT thin films.

Ferroelectric responses were examined in the voltage range of 5 V to 15 V. Actually higher voltages can be applied to the BZT-BCT thin films. However, 15 V is a limit for maximum polarization of the films which have slope as zero. This situation is called as saturation point of the hysteresis of the ferroelectric films.

Table 4.4 Remnant Polarization and Coercive Field values for different sintering temperatures.

Sintering Temperature (°C)	Remnant polarization (P_r) ($\mu C/cm^2$)			Coercive Field (E_c) (kV/cm)		
	5 V	10 V	15 V	5 V	10 V	15 V
700	0.63	1.00	1.18	16.8	28.0	28.6
750	0.55	1.05	1.16	11.0	25.0	11.6
800	1.04	1.82	2.91	19.0	33.0	47.5
850	0.64	1.29	2.07	16.8	31.0	40.0
900	0.45	0.94	0.95	17.0	25.0	23.0

Figure 4.39 to 4.43 show the hysteresis curves of BZT-BCT thin films for various voltage values and different sintering temperatures. Sintered samples at 700, 750 and 900 °C have an interesting situation about comparison of different voltages. Remnant polarization values for different applied voltages (especially 10 V and 15 V in comparison) do not have so much difference which can also be followed in Table 4.4. For example, while remnant polarization value for sintered samples at 700 °C is 1.00 μC/cm^2 for 10 V, it is 1.18 μC/cm^2 for 15 V. This is probably because of the existence of pyrochlore phase at 700 °C and 900 °C which causes a limitation of the polarization with applied higher voltages. Samples sintered at 750 °C exhibit no pyrochlore phase in the films, however it was mentioned before (in comparison of dielectric properties) that 750 °C is below the crystallization temperature which was given in thermal analysis. So, as a result, the phase is also not well crystallized at this process temperature which leads to lower electrical properties.

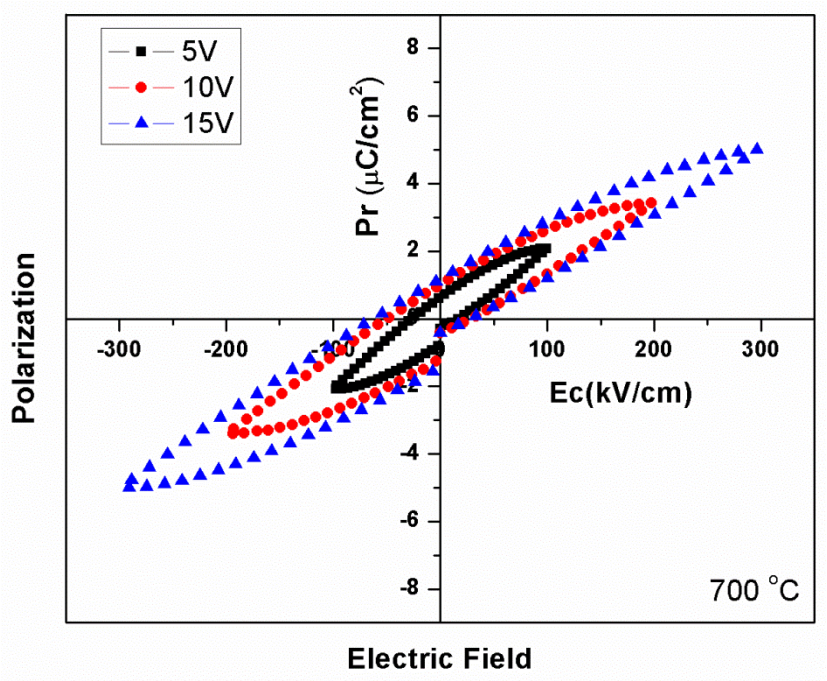

Figure 4.39 Hysteresis curves of BZT-BCT thin films for different applied voltages sintered at 700 °C for 1 h.

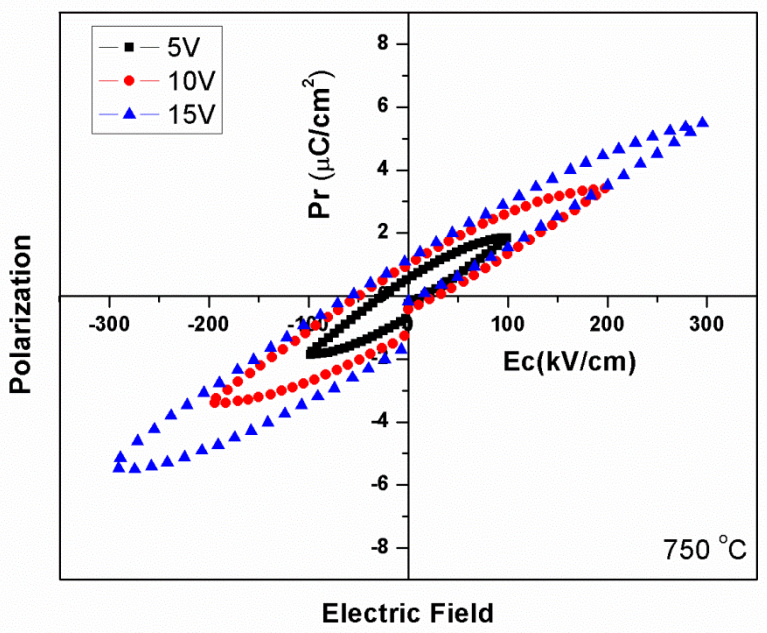

Figure 4.40 Hysteresis curves of BZT-BCT thin films for different applied voltages sintered at 750 °C for 1 h.

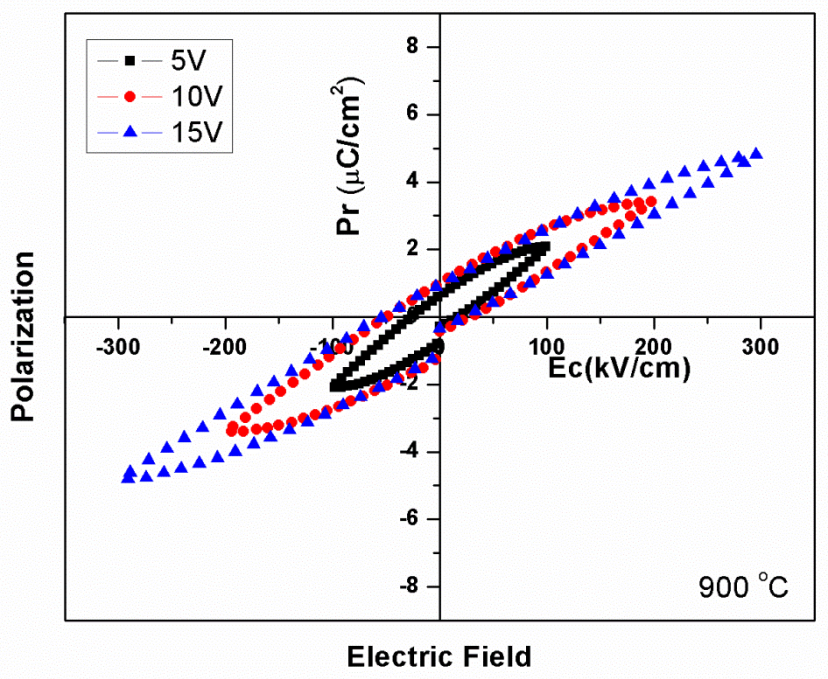

Figure 4.41 Hysteresis curves of BZT-BCT thin films for different applied voltages sintered at 900 °C for 1 h.

However, BZT-BCT thin films sintered at 800 and 850 °C have a significant difference in comparison with other process temperatures. At first, the situation of having almost similar remnant polarization values which is mentioned above is not seen for samples sintered at 800 and 850 °C. As it is seen in Figure 4.44 (Ferroelectric responses of $Ba(Ti_{0.8}Zr_{0.2})O_3$-$(Ba_{0.7}Ca_{0.3})TiO_3$ thin films as a function of sintering temperature at applied voltages of 15 V), the maximum polarization values were observed for BZT-BCT thin films sintered at 800 °C for 1 h as 2.9 $\mu C/cm^2$. As explained before for the explanation of dielectric properties, the sample sintered at 800 °C had the lowest amount of surface porosity which yielded the highest remnant polarization value in comparison with sintered samples at 850 °C.

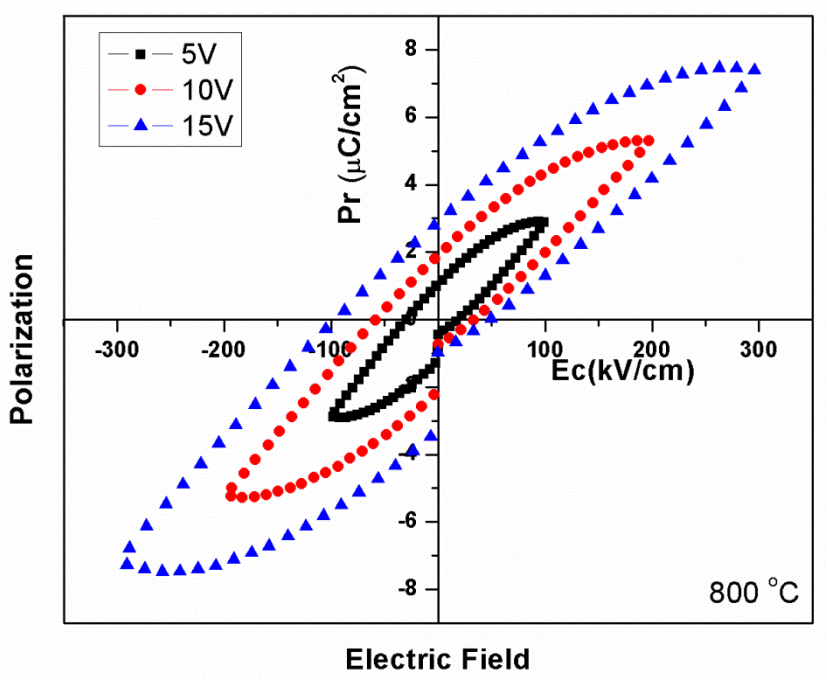

Figure 4.42 Hysteresis curves of BZT-BCT thin films for different applied voltages sintered at 800 °C for 1 h.

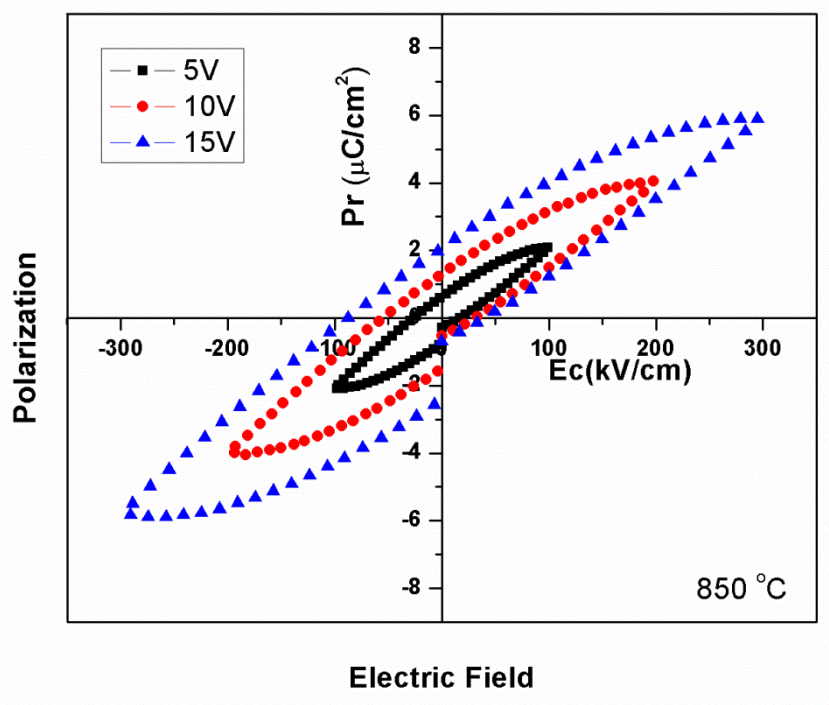

Figure 4.43 Hysteresis curves of BZT-BCT thin films for different applied voltages sintered at 850 °C for 1 h.

The coercive fields of the sintered samples at different temperatures do not tend to give the same behavior of the remnant polarization with respect to sintering temperatures until 800 °C. While the remnant polarizations of samples sintered for 700 to 750 °C do not vary much (as 1.16 and 1.18 μC/cm^2, respectively), coercive fields of the same samples were 28.6 and 11.6 kV/cm, respectively, at 15 V applied voltage. The largest coercive field was observed as 47.5 kV/cm at 15 V applied voltage for sintered samples at 800 °C for 1 h. For samples sintered at 850 °C, the coercive field was also high such as 40.0 kV/cm. This can be explained by well polarization which is seen in Figure 4.43. The coercive field for samples sintered at 900 °C is around 23.0 kV/cm since polarization observed is weak that can be followed in Figure 4.41.

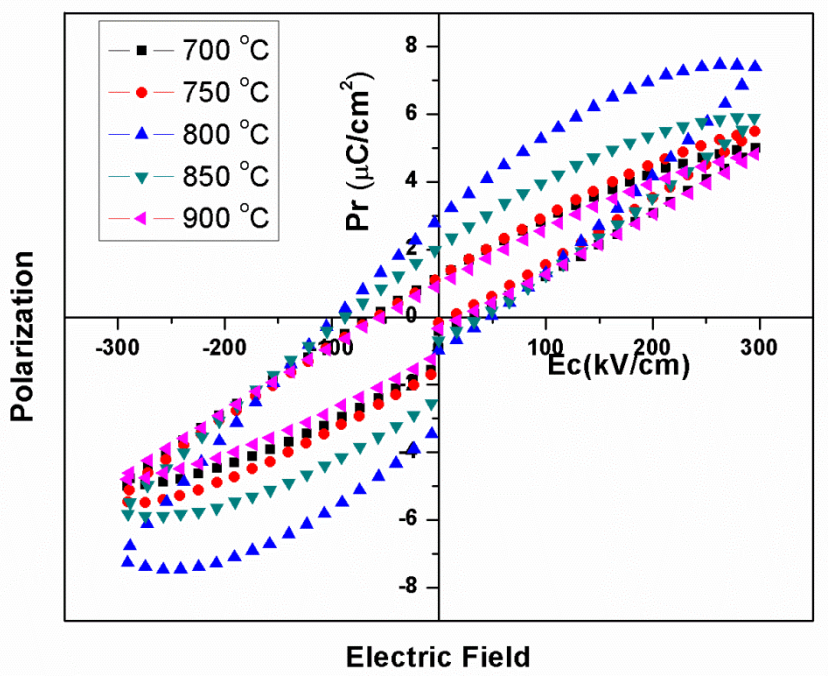

Figure 4.44 Hysteresis curves of BZT-BCT thin films sintered at different temperatures for 1 h using applied voltage of 15 V.

CHAPTER 5

SUMMARY, CONCLUSIONS AND FURTHER SUGGESTIONS

In this thesis, lead free $Ba(Ti_{0.8}Zr_{0.2})O_3$-$(Ba_{0.7}Ca_{0.3})TiO_3$ thin films were prepared using chemical solution deposition method and coated on (111)-Pt/Ti/SiO_2/Si-(100) substrates. Different process parameters were examined with respect to morphological, structural and thermal properties to find out optimum ferroelectric and dielectric properties of BZT-BCT thin films.

At first, it is clearly observed that stable stock solutions were obtained and ability for a successful coating of these solutions was studied. The molarity and volume of the solution was kept as 0.845 M and 40 ml, respectively, in all of the study. 2-methoxyethanol and acetic acid were used as solvents and a few milliliters ethylene glycol was used to obtain crack-free films. Viscosity measurements showed that viscosity did not change with the increase of the shear rate which means that the solution was uniform and homogeneous coatings can be done with these solutions.

Additionally, our films which are grown on Pt/Ti/SiO_2/Si-(100) substrates were crack-free and smooth. The spin coating process used in the study, 1500 rpm spin rate and 30 s spinning speed, results with 500 nm thick film through 3 coating-pyrolysis cycles and also different thicknesses were studied for single and multiple layering. While single layered and two layered films had 220 and 350 nm thickness, respectively, four layered films were 625 nm in thickness. It is observed about the thickness that one and two coating-pyrolsis cycles were not enough to obtain optimum ferroelectric and dielectric measurements because of the existence of dielectric breakdown. Four layered coatings (around 650 nm in thickness) resulted with cracked films because of the stresses produced on the films. Therefore, three

coating layers (around 500 nm in thickness) were the optimum choice at this solution molarity (0.845 M) to produce $Ba(Ti_{0.8}Zr_{0.2})O_3$-$(Ba_{0.7}Ca_{0.3})TiO_3$ composition as a measurable thin film.

Structural analyses were done for BZT-BCT 500 nm thin films to understand the effect of process parameters on the crystallization behavior of these films. Structural analysis showed that pure perovskite phase was observed without the presence of secondary phases sintered at 750 ˚C, 800 ˚C, and 850 ˚C. The peak intensities of perovskite phase for these temperatures were almost the same. Thus, the selection of optimum sintering temperature cannot be done by just using these XRD results. 600 ˚C, 700 ˚C and 900 ˚C sintering temperatures yielded strong pyrochlore phase peaks. This pyrochlore phase was identified as secondary metastable $Ba_2Ti_2O_5$**.**CO_3 phase.

Scanning electron microscopy was used for morphology and cross-section analysis of the BZT-BCT thin films to study surface morphology and film thicknesses. The first morphological studies were done in lower magnifications to determine the existence of cracks on the surfaces. It was clearly observed that surfaces are crack-free. Sintered samples at 700 °C, 750 °C and 800 °C did not yield differences in grain sizes. Measured grain sizes were approximately 60 nm for these samples. As a result of this situation, it can be said that sintering temperatures between 700 °C to 800 °C do not affect much the morphology and grain structure of these films. Films sintered at 850 ˚C showed a high amount of porosity on the surface.

Both morphological and structural analyses showed that $BaTiO_3$ based $Ba(Ti_{0.8}Zr_{0.2})O_3$-$(Ba_{0.7}Ca_{0.3})TiO_3$ composition had homogeneous nucleation throughout the film. This type of growth mechanism yields polycrystalline films as observed in structural analyses and dense-small grained morphology as observed in morphological analysis. The control of the growth mechanism is quite important for thin films to obtain desired electrical properties. As a further suggestion for this part of the study, the change of dissipation of homogeneously nucleated grains within the bulk of the film for the $BaTiO_3$ based thin films is essential. One of the solutions for this problem is decreasing the molarity of the precursor to obtain thinner layers for

each coating-pyrolsis step. For highly dilute solution, the single-coated layer is very thin. This thickness contributes to heterogeneous nucleation at the interface between the new coating layer and the former coated layer, resulting in layer-by-layer homoepitaxial growth within individual grain. This method was tried and structural and SEM analysis showed that highly oriented films were observed. However, this study was not mentioned in the current study.

Dielectric constant (ϵ_r) and dielectric loss (tanδ) values were obtained in the frequency range 1 kHz-1000 kHz with an oscillation voltage of 0.05 V in order to compare the dielectric properties of the films with respect to capacitance-frequency measurements. This frequency range is selected since dielectric properties were almost stable. Optimum dielectric constant (ϵ_r) and dielectric loss (%) values were obtained as 365.6 and 3.52 % at 600 kHz frequency for the BZT-BCT thin films sintered at 800 °C.

The ferroelectric properties of BZT-BCT thin films were investigated using measurement of polarization-applied electric field curves (hysteresis loops) to find out optimum sintering temperature for the films. Remnant polarization (Pr) and coercive field (Ec) values were determined as 2.91 $\mu C/cm^2$ and 47.5 kV/cm, respectively, for the films sintered at 800 °C using 15 V applied voltage.

Both ferroelectric and dielectric results were evaluated in the light of morphological and structural information. Thus, process parameter as 800 °C is selected as the optimum sintering temperature for the production of $BaTiO_3$ based BZT-BCT thin films.

To achieve better dielectric and ferroelectric properties, the presence of a dust free environment is essential. Any unknown particle in the coating step can cause an electric shortage between the electrodes during the measurements. Also, a professional wafer cleaning has to be provided to remove all particles resulting from substrate preparation for better films. Also, alcohol based Ba^{2+}, Ca^{2+} metal alkoxides can be used instead of metal acetates used in this study to decrease the sintering

temperatures which can result with better morphologies which is mentioned in the literature.

REFERENCES

1. A.S. Bhalla and K. M. Nair, The American Ceramic Society, Vol. 25, 1992.

2. K. Tu, J. W. Mayer and L. C. Feldman, Electronic Thin Film Science for Electrical Engineers and Materials Scienctists, Mazwell Macmillan International, 1992.

3. W. Liu and X. Ren, Physical Review Letters, Vol. 103, 257602, 2009.

4. R. W. Schwartz, T. Schneller, R. Waser, Comptes Rendus Chimie, 433-461, 2004.

5. Y. Saito, H. Takao, T. Tani, T. Nonoyama, K. Takatori, T. Homma, T. Nagaya and M. Nakamura, Nature, Vol. 432, 7013, 2004.

6. G. A. Smolenskii, V. A. Isupov, A. I. Agranovskaya, and N. N. Krainik, Sov. Phys. Solid State, Vol. 2, 11, 1961.

7. B. T. Matthias and J. P. Remeika, Phys. Rev., 82, 5, 727-729, 1951.

8. H. Bao, C. Zhou, D. Xue, J. Gao and X. Ren, Journal of Physics D: Applied Physics, Vol. 43, 465401, 2010.

9. D. Xue, Y. Zhou, H. Bao, C. Zhou, J. Gao, and X. Ren, Journal of Applied Physics, Vol. 109, 054110, 2011.

10. J. Gao, D, Xue, Y. Wang, D. Wang, L. Zhang, H. Wu, S. Guo, H. Bao, C. Zhou, W. Liu, S. Hou, G. Xiao, and X. Ren, Applied Physics Letters, Vol. 99, 092901, 2011.

11. W. Li, Z. Xu, R. Chu, P. Fu, and G. Zang, J. Am. Ceram. Soc., Vol. 93, 2942-2944, 2010.

12. D. E. Cox et al., Appl. Phys. Lett., Vol. 79, 400, 2001.

13. W. D. Callister, J., Materials Science and Engineering An Introduction. New York: Wiley, 2007, 7th edition.

14. Princeton University, Solid State Chemistry Group, November 2011, http://www.princeton.edu/~cavalab/tutorials/public/structures/perovskites.html

15. D. Damjanovic, Rep. Prog. Phys., Vol. 61, 1267- 1324, U.K. 2012.

16. B. Kaplan, Preparation of PNZT Thin Films by Chemical Solution Deposition and Their Characterization. M.S. Thesis (Supervisor: Prof. Dr. Macit Özenbaş), Middle East Technical University, Ankara-Turkey, 2005.

17. Dielectric Behaviour and Structure, Edited by C. P. Smyth, New York, McGraw-Hill, 1955.

18. Dielectric Materials and Applications, Edited by Arthur R. Von Hippel, pp. 19, 1954.

19. PC in control, http://www.pc-control.co.uk/piezoelectric_effect.htm, January 2008.

20. P. K. Larsen, R. Cuppens and G. A. C. M. Spierings, Vol. 128, 265-292, 1992.

21. Ferroelectric RAM, http://en.wikipedia.org/wiki/File:1T_FeRAM_cell_structure.svg, October 17, 2007.

22. J. F. Scott and C. Araujo, Vol. 246, 1400-1405, 1989.

23. Piezoelectric Materials, http://www.piezomaterials.com/, July 22, 2007.

24. Enver Koray Akdoğan, Dielectric and Piezoelectric Properties of Doped PZT Ceramics, M.S. Thesis (Supervisior:Prof. Dr. Muharrem Timuçin), Middle East Technical University, Ankara-Turkey, 1994.

25. Bernard Jaffe, Piezoelectric Ceramics, London, New York, Academic Press, 1971.

26. Cambridge University, Teaching and Learning Packages, U.K. 2012, http://www.doitpoms.ac.uk/tlplib/piezoelectrics/polarisation.php

27. American Piezo Ceramics International, LTD, Piezoelectric Ceramics: Principles and Applications, Mackeywille, Pennsylvania, 17750 USA.

28. A. Safari and M. Abazari, Ferroelectrics, and Frequency Control, Vol. 57, 10, 2010.

29. K. Wang, J. F. Li, and N. Liu, Applied Physics Letters, Vol. 93, 092904, 2008.

30. E. Hollenstain, M. Davis, D. Damjanovic, and N. Setter, Applied Physics Letters, Vol. 87, 182905, 2005.

31. D. Lin, K. W. Kwok, and H. L. W. Chan, Journal of Applied Physics, Vol. 102, 0.34102, 2007.

32. C. W. Ahn, H. J. Seog, A. Ullah, S. Y. Lee, J. W. Kim, S. S. Kim, M. Park, K. No, and W. Kim, Vol. 111, 024110, 2012.

33. T. Takenaka, K. Maruyama, K. Sakata, Jpn. J. Appl. Phys., 30 (9B), p. 2236, 1991.

34. B.J. Chu, D.R. Chen, G.R. Li, Q.R. Yin, J. Eur. Ceram. Soc., 22, p. 2115, 2002.

35. L.F. Gao, Y.Q. Huang, Y. Hu, H.Y. Du, Ceram. Int., 33, p. 1041, 2007.

36. Y.F. Qu, D. Shan, J.J. Song, Mater. Sci. Eng. B, 121, p. 148, 2005.

37. J. Suchanicz, J. Kusz, H. Bohm, H. Duda, J.P. Mercurio, K. Konieczny, J. Eur. Ceram. Soc., 23, p. 1559, 2003.

38. J.R. Gomah-Pettry, A.N. Salak, P. Marchet, V.M. Ferreira, J.P. Mercurio, Phys. Stat. Sol. B, 241, p. 1949, 2004,

39. K. Sakata, T. Takenaka, Y. Naitou, Ferroelectrics, 131 (1992), p. 219

40. V. Dorcet, P. Marchet, G. Trolliad, J. Eur. Ceram. Soc., 27 (2007), p. 437

41. P. Marchet, E. Boucher, V. Dorcet, J.P. Mercurio, J. Eur. Ceram. Soc., 26 (2006), p. 3037

42. H. Nagata, N. Koizumi, T. Takenaka, Key Eng. Mater., 169–170 (1999), p. 37

43. A. Sasaki, T. Chiba, Y. Mamiya, E. Otsuki, Jpn. J. Appl. Phys., 38 (9B) (1999), p. 5564

44. Y.M. Li, W. Chen, J. Zhou, Q. Xu, H.J. Sun, R.X. Xu, Mater. Sci. Eng. B, 112 (2004), p. 5

45. X.X. Wang, X.G. Tang, H.L.W. Chan, Appl. Phys. Lett., 85 (2004), p. 91

46. H. Nagata, T. Takenaka, Jpn. J. Appl. Phys., 37 (9B) (1998), p. 5311

47. X.X. Wang, H.L.W. Chan, C.L. Choy, J. Am. Ceram. Soc., 86 (10), p. 1809, 2003.

48. A. Herabut, A. Safari, J. Am. Ceram. Soc., 80 (11), p. 2954, 1997.

49. F. Gao, C.S. Zhang, X.C. Liu, L.H. Cheng, C.S. Tian, J. Eur. Ceram. Soc., 27 , p. 3453, 2007.

50. X.Y. Wang, C.L. Wang, M.L. Zhao, J.F. Wang, K. Yang, J.C. Li, Mater. Lett., 61, p. 3847, 2007.

51. D.M. Lin, D.Q. Xiao, J.G. Zhu, P. Yu, J. Eur. Ceram. Soc., 26, p. 3247, 2006.

52. M. Abazari, A. Safari, S. S. N. Bharadwaja, and S. Trolier-McKinstry, Applied Physics Letters, Vol. 96, 082903, 2010.

53. Thurnauer H. ,The Rochester Engineer, Vol. 21, 74-75, 1947.

54. X.S. Wang, L.L. Zhan, H. Liu, J. W. Zhai, X. Yao, Mater. Chem. Phys., Vol. 112, 675, 2008.

55. O. P. Thakur, C. Prakash, and A. R. James, Journal of Alloys and Compounds, Vol. 470, 548-551, 2009.

56. X. S. Wang, H. Yamada, and C. N. Xu, Applied Physics Letters, Vol. 86, 022905, 2005

57. Takenaka T. and Nagata H, J. Eur. Ceram. Soc., Vol 25, 2693, 2005.

58. H. X. Fu and R. E. Cohen, Nature (London), Vol. 403, 281, 2000.

59. M. Ahart et al., Nature (London), Vol. 451, 545 2008.

60. G. A. Rossetti, A. G. Khachaturyan, G. Akçay, and Y. Ni, Journal of Applied Physics, Vol. 103, 114113, 2008.

61. M. J. Haun, E. Furman, S. J. Jang, and L. E. Cross, Ferroelectrics, Vol. 99, 13, 1989.

62. E. K. H. Salje, Phase Transitions in Ferroelastic and Co-Elastic Crystals, Cambridge University Press, Cambridge, 1990.

63. J. Wu and J. Wang, Journal of Applied Physics, Vol. 106, 066101, 2009.

64. Y. Nakashima, W. Sakamoto and T. Yogo, Journal of European Ceramic Society, Vol. 31, 2497-2503, 2011.

65. P. C. Goh, K. Yao, and Z. Chen, Applied Physics Letters, Vol. 99, 092902, 2011.

66. C. W. Ahn, H. J. Seog, A. Ullah, S. Y. Lee and J. W. Kim, Journal of Applied Physics, Vol. 111, 024110, 2012.

67. P. C. Goh, K. Yao and Z. Chen, Applied Physics Letters, Vol. 97, 102901, 2010.

68. F. Lai, J. F. Li, Z. X. Zhu and Y. Xu, Journal of Applied Physics, Vol. 106, 064101, 2009.

69. L. Wang, R. Zuo, L. Liu, H. Su, M. Shi, X. Chu, X. Wang and L. Li, Materials Chemistry and Physics, Vol. 130, 165-169, 2011.

70. M. Abazari, T. Choi, S. W. Cheong and A. Safari, Journal of Physics D: Applied Physics, Vol. 43, 025405, 2010.

71. L. Lian and N. R. Sottos, Journal of Applied Physics, Vol. 87, 3941, 2000.

72. H. Zhou, X. Liu, N. Qin, and D. Bao, Journal of Applied Physics, Vol. 110, 034102, 2011.

73. D. Z. Zhang, X. J. Zheng, X. Feng, T. Zhang, J. Sun, S. H. Dai, L. J. Gong, Y. Q. G. He, Z. Zhu, J. Huang and Z. Xu, Journal of Alloys and Compounds, Vol. 504, 129-133, 2010.

74. T. Yu, K. W. Kwok and H. L. W. Chan, Thin Solid Films, Vol. 515, 3563-3566, 2007.

75. Y. Guo, D. Akai, K. Sawada and M. Ishida, Solid State Sciences, Vol. 10, 928-933, 2008.

76. T. Yu, K. W. Kwok and H. L. W. Chan, Materials Letters, Vol. 61, 2117-2120, 2007.

77. C. Dragoi, M. Cernea and L. Trupina, Applied Surface Science, Vol. 257, 9600-9605, 2011.

78. A. Piorra, A. Petraru, H. Kohlstedt, M. Wuttig, and E. Quandt, Journal of Applied Physics, Vol. 109, 104101, 2011.

79. K. Mimura, T. Naka, T. Shimura, W. Sakamoto and T. Yogo, Thin Solid Films, Vol. 516, 8408-8413, 2008.

80. L. N. Gao, J. W. Zhai, and X. Yao, J Sol-Gel Sci. Tech., Vol. 45, 51-55, 2008.

81. L. L. Jiand, X. G. Tang, Q. Li, H.L.W. Chan, Vacuum, Vol. 83, 1018-1021, 2009.

82. Sol-Gel Technology for Thin Films, Fibers, Preforms, Electronics and Specialty Shapes, Edited by Lisa C. Klein, pp. 297, 1988.

83. Nemo, http://optoweb.fis.uniroma2.it/opto/solgel/index.html, January 2008.

84. J. Fukushima, K. Kodaira,and T. Matsushita, Journal of Material Science, Vol. 19, 595, 1984.

85. Robert W. Schwartz, T. Schneller, and R. Waser, C. R. Chimic, Vol. 7, 433-461, 2004.

86. D. E. Bornside, C. W. Macosco and L. E. Scriven, Journal of Imaging Technology, Vol. 13, 122-129, 1987.

87. I.M. Reaney, K. Brooks, R. Klissurka, C. Pawlaczyk, N. Setter J. Am. Ceram. Soc., Vol. 77, 1209, 1994.

88. E.M. Griswold, L. Weaver, M. Sayer, J.D. Calder J. Mater. Res., Vol. 10, 3149, 1995.

89. A.P. Wilkinson, J.S. Speck, A.K. Cheetham, S. Nataraan, J.M. Thomas Chem. Mater., Vol. 6 , 750, 1994.

90. P. Duran, D. Gutierrez, J.Tartaj, M. A. Banares and C. Moure, Journal of European Ceramic Society, Vol. 22, 797-807, 2002.

91. Viscosity, http://en.wikipedia.org/wiki/Viscosity, August 11, 2012.

92. Karakuşçu, Characterization of Maghemite Thin Films Prepared by Sol-Gel Processing. M.S. Thesis (Supervisor: Prof. Dr. Macit Özenbaş), Middle East Technical University, Ankara-Turkey, 2006.

93. Yale University, Fractal Geometry Couse Page, August 2012
http://classes.yale.edu/fractals/panorama/physics/dla/DBM/DBM.html

94. Y. Jiang, X. Tang, Q. Liu, T. Cheng, Y. Zhou, Trans. Nonferrous Met. Soc. China 17, 862-865, 2007.

95. S. W. Ko, D. A. Mourcey, T. Clark, S. Trolier-McKinstry, J Sol-Gel Sci Technol, 54, 269-275, 2010

96. L. Fang, M. Shen, D. Yao, Appl. Phys. A, 80, 1763-1767, 2005.

97. Gopalakrishnamurthy, H. S., Rao, M. S. and Kutty, T. R. N., Thermal decomposition of titanyl oxalates—I. Barium titanyloxalate. J. Inorg. Nucl. Chem., 1975, 37, 891–898.

98. Hoffmann et al., Journal of European Ceramic Society, 19, 1339-1343, 1999

99. C. Kügeler et al., Inst. of Solid State Res. & Jara-Fundamentals for Future Inf. Technol., Jülich, Germany, 2006

100. Cambridge University, Teaching and Learning Packages, U.K., http://www.doitpoms.ac.uk/tlplib/dielectrics/variation.php, July 18, 2012.